UNIVERSITÉ DE NICE-SOPHIA ANTIPOLIS
U.F.R FACULTE DES SCIENCES

THESE

Présentée pour obtenir le titre de
Docteur en SCIENCES (Sciences de l'Ingénieur)

par

Yannick PONTY

TEXTURES CONVECTIVES DANS UN FLUIDE EN ROTATION ET EFFET DYNAMO DANS UN ECOULEMENT FAIBLEMENT CHAOTIQUE

Soutenue à l'Observatoire de Nice
Le 16 janvier 1997 devant le jury composé de:

M. S. Fauve.	Ecole Normale Supérieure de Lyon	Rapporteur
M. T. Passot	Observatoire de la Côte d'Azur	Examinateur
M. A. Pocheau	Université d' Aix-Marseille	Rapporteur
Mme. A. Pouquet	Observatoire de la Côte d'Azur	Examinateur
M. A. Pumir	Institut Non Linéaire de Nice	Président
M. J. Sommeria	Ecole Normale Supérieure de Lyon	Examinateur
M. P.L. Sulem	Observatoire de la Côte d'Azur	Directeur de Thèse
M. L. Valdettaro	Ecole Politecnico di Milano	Examinateur

Résumé

Cette thèse comporte deux parties. La première porte sur les écoulements convectifs à nombre de Prandtl fini, en rotation autour d'un axe vertical, dans des domaines étendus. Un calcul perturbatif sur les équations d'Oberbeck-Boussinesq avec des conditions aux limites libres, a permis de mettre en évidence une nouvelle instabilité qui amplifie les perturbations dont le vecteur d'onde fait un petit angle avec celui des rouleaux de base. Afin d'étudier le développement non linéaire de cette instabilité, un modèle de type Swift-Hohenberg généralisé a été construit et étudié numériquement pour des conditions aux limites libres ou rigides. Dans le premier cas, "l'instabilité à petit angle" produit, en régime faiblement non linéaire, une distortion des rouleaux sous l'effet d'un cisaillement moyen qui conduit, après reconnections, à une rotation continue de la texture. En régime fortement non linéaire, on observe pour des rotations modérées, la formation de structures cohérentes sous forme de cibles de grande taille, associées à la présence de forts tourbillons, une configuration compatible avec les propriétés d'invariance par rotation de l'instabilité à petit angle. Dans le cas de conditions aux limites rigides, la dynamique est gouvernée par le mouvement et l'annihilation de dislocations, pouvant conduire, dans le cas d'un écoulement périodique, à la restabilisation des rouleaux droits.

La deuxième partie de la thèse, porte sur l'étude d'une dynamo cinématique dans un écoulement hamiltonien faiblement perturbé. Le champ magnétique qui se développe dans les zones chaotiques localisées le long des orbites homoclines ou hétéroclines, survit à forts nombres de Reynolds magnétique, contrairement aux tourbillons magnétiques apparaissant dans des zones intégrables. Il est montré que le taux de croissance du champ magnétique est sensible à la largeur des zones chaotiques, qui est évaluée par la méthode de Melnikov.

Abstract

This thesis includes two parts. In the first one, the problem of rotating convection at finite Prandtl number in a large aspect ratio container is considered. A singular perturbation analysis performed on the Oberbeck-Boussinesq equations with free-slip top and bottom boundary conditions, points out a new instability which amplifies perturbations whose wavevectors make a small angle with the wavevector of the basic rolls. In order to study the nonlinear development of this instability, a generalized Swift-Hohenberg model has been derived and studied numerically for both free-slip and rigid boundary conditions. In the former case, the "small-angle instability" produces, in the weakly nonlinear regime, a distortion of the rolls under the effect of a strong mean shear, which, after reconnections, leads to a continuous rotation of the pattern. In the fully nonlinear regime, the formation of coherent targets associated to large vortices, is observed, a pattern consistent with the rotational invariance of the small-angle instability. In the no-slip case, the dynamics is governed by the gliding and the annihilation of dislocations, leading to the stabilization of the straight parallel rolls.

In the second part, the kinematic dynamo action of a weakly perturbed hamiltonian flow is considered. The magnetic structures generated in the chaotic zones along the heteroclinic or homoclinic orbits, survive in the limit of infinite Reynold number, in contrast with the magnetic eddies which appear in integrable zones. It is shown that the magnetic growth rate, is strongly sensitive to the width of the chaotic zones, which is estimated using the Melnikov method.

Remerciements

Je tiens à remercier vivement:

- Pierre Louis Sulem et Thierry Passot pour avoir dirigé cette thèse. Je les remercie de leur constante disponibilité et de leurs nombreux conseils qui m'ont permis de mener à bien mon travail dans de très bonnes conditions,
- Annick Pouquet pour m'avoir fait profiter de son expérience sur le problème dynamo, ainsi que pour son soutien moral,
- Stéphan Fauve et Alain Pocheau qui ont accepté de rapporter sur ce travail, ainsi que Alain Pumir, Jöel Sommeria et Lorenzo Valdettaro qui l'ont également examiné,
- Richard Kofman et Jean-Pierre Provost de leurs aides et encouragements en ce qui concerne l'enseignement dont j'ai été chargé à l'Université de Nice-Sophia Antipolis au cours de ces quatre dernières années,

- Annick Tschaeglé-Ponty mon épouse, pour son aide morale tout le long de ces nombreuses années d'études et de vie commune,
- ma famille de m'avoir aidé et soutenu,
- Hélène Politano et Tony Tschaeglé pour leur lecture attentive du mémoire,
- Jean-Marc Petit et Alain Noullez pour leurs aides précieuses,
- mes amis thésards et stagiaires: Elke Lohinger, Frédric Rué, Fabrice Thomas, Yves Bobichon, Elena Lega et Patrick Bury, pour les bons moments passés ensemble et les nombreuses aides qu'ils m'ont apportés,
- ainsi que tous les personnels de l'Observatoire, en particulier ceux du Centre de Calcul pour leurs nombreux conseils.

  Et enfin, je ne saurais oublier tous mes amis.

Je dédie ma Thèse à mon épouse Annick, à mon fils Florian
à mes parents, mes grands parents et ma tante.

TABLE DES MATIERES

I Convection dans un fluide en rotation 1

A Introduction 3

1 L'équation de Boussinesq avec rotation 3

1.1 Formulation usuelle 4

1.2 Conditions aux limites 5

1.3 Analyses en modes normaux 5

2 L'instabilité de Küppers-Lortz 6

3 Modèles isotropes 9

Bibliographie 11

B Stabilité des rouleaux de convection en présence de rotation, à nombre de Prandtl fini 13

A new instability for finite Prandtl number rotating convection with free-slip boundary conditions Y. Ponty, T. Passot and P.L. Sulem *Phys. Fluids.* **9**, 67 (1997) 19

1 Introduction 20

2 Steady convective rolls in a rotating frame 21

3 The Küppers-Lortz instability 23

4 The small-angle instability 27

5 Nature of the instability and nonlinear developments 35

Bibliography 38

C Convection avec rotation dans un système étendu. 41

1 Modèle de convection à nombre de Prandtl fini 42

2 Relation entre l'instabilité d'amplitude à petit angle et l'instabilité de phase varicose oblique. 44

3 Dynamique non linéaire du modèle simplifié avec des conditions aux limites libres. 47

4 Dynamique non linéaire du modèle avec des conditions aux limites rigides. 49

5 Appendice 51

Pattern dynamics in rotating convection at finite Prandtl number

Y. Ponty, T. Passot and P.L. Sulem *Phys. Rev. E (sous presse)* 55

1 Introduction 56

2 A model for rotating convection 57

2.1 An asymptotic model near threshold for free-slip boundaries 57

2.2 Linear stability analysis 60

2.3 A simplified model 63

2.4 Modeling rigid boundaries 68

3 Weakly nonlinear dynamics 71

3.1 Nonlinear development of the small-angle instability 71

3.2 Derivation of the phase-mean drift equations 73

3.3 Relation between the small-angle and the skewed-varicose instabilities 75

3.4 Busse balloons for rigid boundary conditions 81

4 Nonlinear dynamics for free-slip boundary conditions 84

5 Nonlinear dynamics for rigid boundary conditions 89

6 Summary 95

Bibliography 96

Chaos and structures in rotating convection at finite Prandtl number

Y. Ponty, T.Passot and P.L. Sulem *Phys. Rev. lett.* **79**, *juillet 1997* 101

II Effet dynamo dans un écoulement chaotique 115

A Introduction 117

1 Dynamo cinématique 117

2 Dynamo dans un écoulement $2D\frac{1}{2}$ 119

Bibliographie 120

B Dynamo cinématique dans un flot hamiltonien faiblement perturbé 123

Dynamos in weakly chaotic two-dimensional flows
Y. Ponty, A. Pouquet and P.L. Sulem
J. Geophys. Astrophys. Fluid Dyn. **79**, 239 (1995). 127

1 Introduction 128

2 The CP flow 129

3 Dynamo growth rates 136

4 Geometry of the magnetic field 139

Bibliography 149

Appendix 151

C Effet dynamo pour un écoulement proche de l'intégrabilité. 155

Dynamo Action in a Nearly Integrable Chaotic Flow
Y. Ponty, A. Pouquet, V. Rom-Kedar and P.L Sulem
Theory of Solar and Planetary Dynamos , 241-248 M.R.E Proctor, P.C Matthews & A.M Rucklidge (eds.), Cambridge University Press (1993). . 159

1 Introduction 160

2 The dynamical system 160

3 Dynamo action 163

4 Dynamo and chaos: how are they Connected? 165

Bibliography 168

RESULTATS ET PERSPECTIVES 171

Partie I

Convection dans un fluide en rotation

Chapitre A

Introduction

Une couche de fluide incompressible subissant un gradient de température juste au dessus du seuil de convection s'organise en structures spatiales cohérentes sous forme de rouleaux ou d'autres textures. Dans un domaine à grand rapport d'aspect et à nombre de Prandtl fini, la dynamique horizontale conduit à l'existence d'écoulements à grande échelle issus de la courbure des textures. La rotation, introduisant des forces supplémentaires, va dynamiser ces textures horizontales, et introduire de nouvelles instabilités.

1 L'équation de Boussinesq avec rotation

Une couche de fluide incompressible subissant un gradient de température et une rotation d'axe vertical où l'approximation de Boussinesq est valide, est gouvernée par le système d'équations adimensionnées suivant

$$\begin{aligned} P^{-1}(\frac{\partial}{\partial t}\mathbf{u} + \mathbf{u}.\nabla\mathbf{u}) &= \Delta\mathbf{u} + \hat{\mathbf{z}}\vartheta - \nabla(p+\Gamma) - \tau\hat{\mathbf{z}}\times\mathbf{u} && (1)\\ \nabla.\mathbf{u} &= 0 && (2)\\ \frac{\partial}{\partial t}\vartheta + \mathbf{u}.\nabla\vartheta &= \Delta\vartheta + R_a\hat{\mathbf{z}}.\mathbf{u}\ . && (3) \end{aligned}$$

Le fluide subit la force de Coriolis en $-\hat{\mathbf{z}}\times\mathbf{u}$ et son étude se place dans le référentiel tournant associé, la force centrifuge est réécrite comme un gradient $\nabla\Gamma$, et s'ajoute à la pression du fluide p. La vitesse du fluide est notée $\mathbf{u}$, et ϑ est l'écart à la température moyenne. Ce système est paramétré par deux nombres sans dimension. Le nombre de Rayleigh $R_a = \frac{\alpha g \Delta T h^3}{\kappa\nu}$ détermine le seuil de l'instabilité convective qui est déterminé par un rapport entre le coefficient de dilation thermique α, l'accélération g, la différence de température entre la plaque supérieure et inférieure du fluide ΔT, l'épaisseur de la couche de fluide h et la diffusivité cinématique ν et thermique κ. Il y a aussi le nombre de Prandtl $P = \frac{\nu}{\kappa}$ qui est le rapport entre la diffusion visqueuse et thermique. Pour un fluide en rotation, un nombre sans dimension supplémentaire est présent, le nombre de Rossby $R_o = \Omega \frac{h^2}{\nu}$ où Ω est la vitesse angulaire et $t_\nu = \frac{h^2}{\nu}$ représente le temps caractéristique visqueux. Ce nombre de Rossby est représenté par le coefficient τ qui est égal à deux fois le nombre de Rossby R_o, et τ^2 est appelé le nombre de Taylor.

1.1 Formulation usuelle

Le fluide considéré étant incompressible, il est habituel d'éliminer la pression en projetant l'équation (1) sur un espace de divergence nulle. Dans cette formulation, on montre que la force centrifuge n'apporte rien à la dynamique, seule la force de Coriolis va jouer un rôle. On note la vitesse des particules fluides $\mathbf{u} = (u, v, w)$. Une notation souvent utilisée ([3],[20],[4]), consiste à séparer la composante horizontale de la vitesse en une partie irrotationnelle dérivant d'un potentiel ϕ et la partie rotationnelle dérivant d'une fonction courant ψ, en écrivant

$$\mathbf{u} = \Lambda(\phi\hat{\mathbf{z}}) + \Upsilon(\psi\hat{\mathbf{z}}) = \begin{pmatrix} \partial_z\partial_x\phi + \partial_y\psi \\ \partial_z\partial_y\phi - \partial_x\psi \\ -\Delta_h\phi \end{pmatrix}$$

avec $\Upsilon = \nabla \times .$, $\Lambda = \nabla \times (\nabla \times .)$ et $\Delta_h = \partial_x^2 + \partial_y^2$.

Une autre notation similaire est aussi utilisée ([21]):

$$\begin{aligned} u &= \partial_x\bar{\phi} + \partial_y\psi \\ v &= \partial_y\bar{\phi} - \partial_x\psi \\ \partial_z w &= \Delta_h\bar{\phi} \end{aligned}$$

où $\bar{\phi}$ est relié à ϕ par la relation $\bar{\phi} = \partial_z\phi$.

Avec ces deux notations, on peut réécrire le système des eqs. (1)-(3) sous la forme ([2],[21]),

$$\begin{aligned} P^{-1}(\partial_t\Delta w + \mathcal{Q}_1) &= \Delta^2 w + \Delta_h\vartheta + \tau\partial_z\Delta_h\psi && (4) \\ (\partial_t - P\Delta)\Delta_h\psi &= -\tau P\partial_z w + \partial_x(\mathbf{u}\cdot\nabla v) - \partial_y(\mathbf{u}\cdot\nabla u) && (5) \\ \partial_t\vartheta + \mathbf{u}\cdot\nabla\vartheta &= \Delta\vartheta + R_a w && (6) \end{aligned}$$

avec

$$\mathcal{Q}_1 = \Delta_h(\mathbf{u}\cdot\nabla w) - \partial_z\left(\partial_x\left(\mathbf{u}\cdot\nabla u\right) + \partial_y\left(\mathbf{u}\cdot\nabla v\right)\right) \ . \qquad (7)$$

On peut noter que dans ces deux formulations la vorticité verticale ξ du champ de vitesse $\mathbf{u}$ est reliée à ψ par la relation $\xi = -\Delta_h \psi$. L'équation de la vorticité verticale (5) va se révéler très importante pour la dynamique convective à faible nombre de Prandtl.

1.2 Conditions aux limites

Le fluide est confiné entre deux plans ($z = 0$ et $z = 1$). La température sur ces deux surfaces est supposée uniforme et constante. L'écart à la température moyenne est donc nul ($\theta = 0$ pour $z = 0$ et 1). Ces surfaces sont indéformables, la vitesse verticale doit donc disparaître ($w = 0$ pour $z = 0$ et 1).

Il y a deux sortes de conditions aux limites généralement utilisées:

La surface est considérée comme rigide lorsque le fluide adhère à la surface. On a donc $u = v = w = 0$ en $z = 0$ et 1. En utilisant l'équation de continuité $\frac{\partial u}{\partial x} + \frac{\partial v}{\partial y} + \frac{\partial w}{\partial z} = 0$, on obtient $\frac{\partial w}{\partial z} = 0$, ce qui est équivalent à $\frac{\partial \phi}{\partial z} = 0$. De plus, les conditions aux limites pour la composante verticale de la vorticité $\xi = \frac{\partial v}{\partial x} - \frac{\partial u}{\partial y} = -\Delta_h \psi$ s'écrivent $\xi = 0$ pour $z = 0$ et 1.

Les conditions aux limites rigides s'écrivent

$$\vartheta = \phi = \frac{\partial \phi}{\partial z} = \psi = 0 \quad \text{pour} \quad z = 0 \text{ et } 1 \ . \tag{8}$$

La surface est considérée comme libre, lorsque le tenseur visqueux n'a pas de composante transverse, d'où $\frac{\partial u}{\partial z} + \frac{\partial w}{\partial x} = \frac{\partial v}{\partial z} + \frac{\partial w}{\partial y} = 0$ et comme w disparaît sur la surface, on obtient $\frac{\partial u}{\partial z} = \frac{\partial v}{\partial z} = 0$ et pour la composante verticale de la vorticité, on obtient $\frac{\partial \xi_z}{\partial z} = 0$. Avec l'équation de continuité, on en déduit que $\frac{\partial^2 w}{\partial z^2} = 0$ ou $\frac{\partial^2 \phi}{\partial z^2} = 0$.

Les conditions aux limites libres s'écrivent

$$\theta = \phi = \frac{\partial^2 \phi}{\partial z^2} = \frac{\partial \psi}{\partial z} = 0 \quad \text{pour} \quad z = 0 \text{ et } 1 \ . \tag{9}$$

1.3 Analyses en modes normaux

En négligeant les termes non linéaires du système eqs. (4)-(6) et en supposant que la couche de fluide est horizontalement illimitée, on peut analyser le comportement linéaire par une décomposition en modes de Fourier. On met ainsi en évidence l'existence d'un nombre d'onde critique et d'un nombre de Rayleigh critique pour lesquels l'instabilité convective apparaît. Le cas avec rotation a été étudié par Chandrasekhar dans [2]. Le nombre de Rayleigh critique pour des conditions aux limites libres est donné par

$$R_{ac} = \frac{((\pi^2 + k^2)^3 + \pi^2 \tau^2)}{k^2} = 3(\pi^2 + k^2)^4 \tag{10}$$

et le nombre d'onde critique k_c est donné par l'équation

$$2(\frac{k}{\pi})^6 + 3(\frac{k}{\pi})^4 = 1 + \frac{\tau^2}{\pi^4} \ . \tag{11}$$

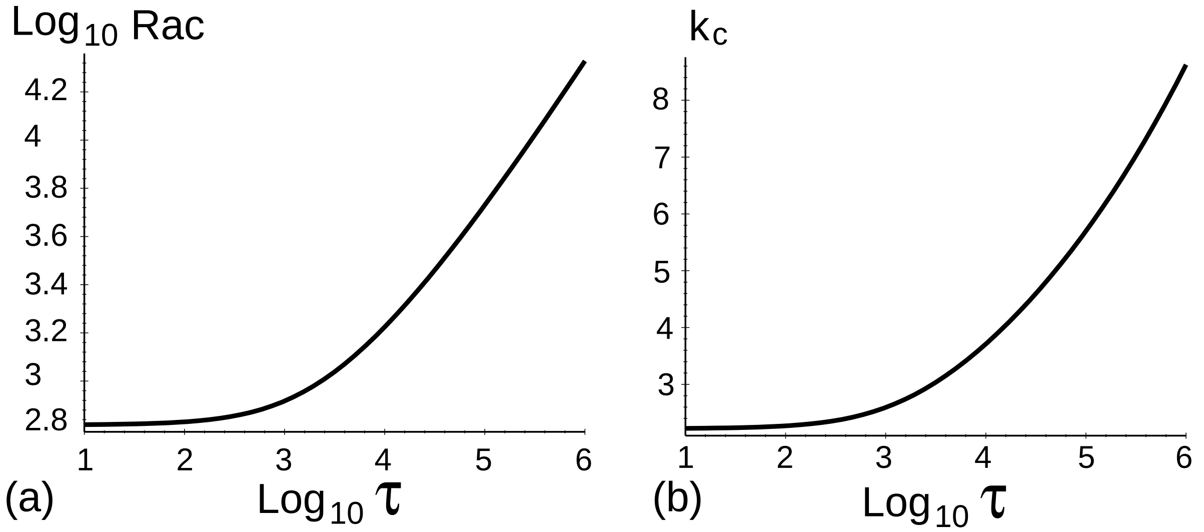

Figure A.i: Pour des conditions aux limites libres, (a) le Rayleigh critique et (b) le nombre d'onde critique en fonction de $log_{10}\tau$, où $\tau/2$ est le nombre de Rossby.

Le comportement du Rayleigh critique et du nombre critique en fonction de la rotation τ pour des conditions aux limites libres est présenté dans la Figure (A.i); dans la limite des fortes rotations, le nombre de Rayleigh et le nombre d'onde critique se comportent comme $R_{ac} \to 3\pi^4(\frac{\tau^2}{2\pi^4})^{\frac{2}{3}}$ et $k_c \to (\frac{\pi^2}{2}\tau^2)^{\frac{1}{3}}$ [2].

Le cas des conditions aux limites rigides est plus complexe car il induit un type de profil de vitesse sur l'axe vertical qui nécessite la résolution numérique d'une équation transcendante [2].

2 L'instabilité de Küppers-Lortz

Les solutions linéarisées des équations de Boussineq avec rotation (4)-(6) ont été étudiées par Chandrasekhar (1953) ([1] et [2]). Küppers et Lortz [3] en 1969 se sont intéressés à la stabilité de telles solutions près du seuil de convection pour des conditions aux limites libres à nombre de Prandtl infini. Ils ont calculé la solution stationnaire, la perturbation et le taux de croissance de la perturbation dans une asymptotique où l'écart au nombre de Rayleigh critique est utilisé comme paramètre de développement. Pour résoudre l'équation linéarisée à chaque ordre, il faut satisfaire une condition de solvabilité. Cette condition donnera à chaque ordre la contribution du taux de croissance de la perturbation.

Pour une solution stationnaire sous forme de rouleaux de convection, le taux de croissance de la perturbation devient positif au-delà d'une rotation critique $\tau_c = 48.7$, pour des vecteurs d'onde de la perturbation faisant un angle proche de 58 degrés avec le vecteur d'onde de base (voir Figure A.ii). Cette instabilité d'amplitude est appelée l'instabilité de Küppers-Lorzt et ce calcul a été étendu par Küppers [4] en 1970 pour des conditions aux limites rigides à nombre de Prandtl fini.

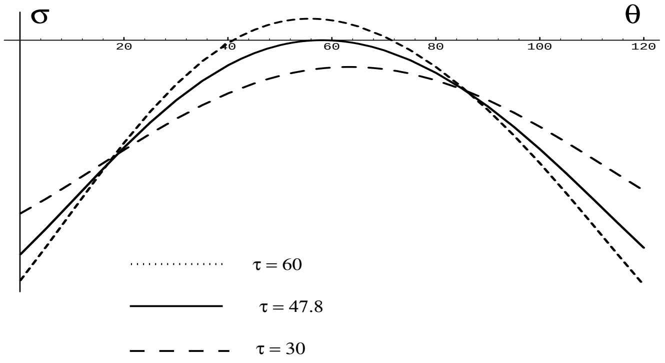

Figure A.ii: Taux de croissance de la perturbation σ en fonction de l'angle θ (en degré) formé par le vecteur d'onde de la perturbation et le vecteur d'onde des rouleaux de base pour différents taux de rotation.

L'analyse linéaire montre que des rouleaux de convection sont déstabilisés pour laisser la place à des rouleaux qui ont une nouvelle orientation tournant d'un angle d'environ 60 degrés. Si l'on reproduit deux fois ce scénario pour cette nouvelle solution de rouleaux, on retrouve sensiblement l'orientation des rouleaux de départ. Une étude à trois modes dont l'orientation reproduit cette dynamique cyclique, a été présentée par Busse et Heikes [5] [6] en 1980.

En supposant une solution sous la forme de trois rouleaux de convection avec trois amplitudes et de directions différentes telle que,

$$w = \sum_{i=1..3} A_i e^{i\vec{k}_i \cdot \vec{x}} + c.c. \text{ avec } \vec{k}_1 + \vec{k}_2 + \vec{k}_3 = 0 \ ,$$

on obtient un système dynamique pour les amplitudes A_i

$$\partial_t A_i = A_i(\epsilon - \sum_{j=1}^{3} g_{ij} |A_j|^2)$$

avec $g_{11} = g_{22} = g_{33} = 1$, $g_{12} = g_{23} = g_{31} = \beta$, $g_{21} = g_{32} = g_{13} = \gamma$.
et où ϵ est l'écart au nombre de Rayleigh critique.

Ce système a été étudié par May et Leonard [7] dans un contexte d'évolution d'une population animale. Ce système comporte huit points fixes qui deviennent tous instables lorsque $\beta + \gamma > 2$ et $\beta < 1$ ou $\gamma < 1$. La solution s'approche de trois orbites hétéroclines qui relient trois points fixes $(\sqrt{\epsilon}, 0, 0), (0, \sqrt{\epsilon}, 0), (0, 0, \sqrt{\epsilon})$ dans l'espace (A_1, A_2, A_3) (figure.A.iii). Dans ce système dynamique, les orbites convergent sur ces points fixes en un temps infini. Il faut donc rajouter une perturbation sous forme de bruit et permettre aux orbites de s'évader des points fixes en un temps fini (Busse (1984) [8]). Les orbites vont tourner de manière cyclique autour des trois points fixes. Ceci modélise l'évolution des rouleaux subissant l'instabilité de Küppers-Lorzt et changeant d'orientation cycliquement. Ce phénomène a été observé expérimentalement [5]. On peut aussi noter la présence de l'instabilité de Küppers-Lortz dans des expériences à très fortes rotations [15], malgré l'existence d'une dynamique très différente associée à la formation de tourbillons.

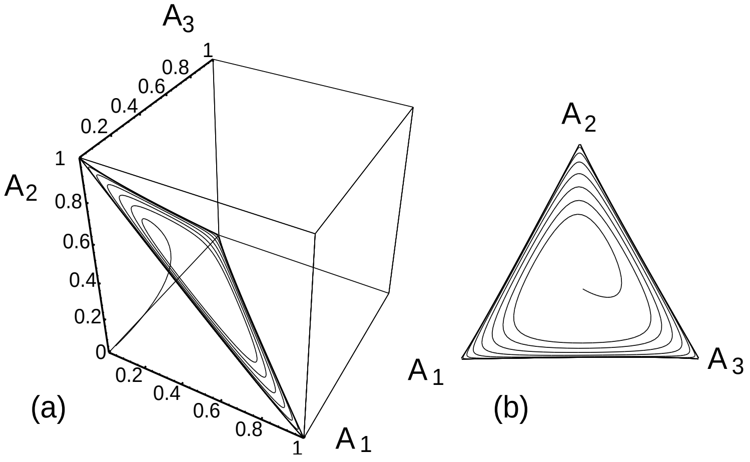

Figure A.iii: (a) Visualisation d'une orbite dans l'espace (A_1, A_2, A_3), tournant autour de trois points fixes hétéroclines et (b) visualisation de la même orbite projetée sur plan de l'orbite pour $\epsilon = 1$, $\beta = 0.1$ et $\gamma = 2$.

Une extension du système dynamique de Heikes-Busse incorporant les effets non-Boussinesq a été étudiée par Millan-Rodrigez et al (1992) [13]. Une approche tenant compte de la dynamique des textures en ajoutant un terme avec une dépendance spatiale du type de Newell-Whitehead-Segel [10],

$$\tau_0 \partial_t A_i = A_i(\epsilon - \sum_{j=1}^{3} g_{ij} |A_j|^2) + \xi_0^2 \left(\partial_{x_i} + \frac{1}{2iq_0} \partial_{y_i}^2 \right)^2 A_i$$

(où ξ_0 est la longueur de corrélation et q_0 la norme du nombre d'onde critique) a permis à Tu et Cross [9] (1992) d'évaluer la vitesse de déplacement du front de changement d'orientation des rouleaux et de prédire que la longueur de corrélation des zones de rouleaux ayant une même orientation varie en $\epsilon^{-\frac{1}{2}}$ avec l'écart au seuil.

Cette instabilité de Küppers-Lorzt est présente au-delà d'une certaine rotation critique qui dépend du nombre de Prandtl et des conditions aux limites , mais aussi pour des rotations plus faibles. Le calcul de stabilité de Clever et Busse (1979) [20] montre l'existence de l'instabilité de Küppers-Lorzt pour des rotations en dessous de la rotation critique à des nombres d'onde inférieurs ou supérieurs au nombre d'onde critique. Elle s'insère dans un ballon de stabilité contenant des instabilités à grande et petite longueurs d'onde.

3 Modèles isotropes

Le champ d'investigation a été élargi, en permettant une orientation isotrope des textures. Alors que les équations d'amplitude sont restreintes à une orientation choisie, des modèles du type Swift-Hohenberg [16] introduisant un caractère isotrope, permettent de traiter toutes les orientations possibles des textures.

Essentiellement, le modèle de Swift-Hohenberg a été modifié, en ajoutant un terme brisant la symétrie de chiralité tel que dans le modèle de Cross, Meiron et Tu ci-dessous [11],

$$\partial_t w = (\epsilon - (\Delta + 1)^2)w - g_1 w^3 + g_2 \nabla \times [(\nabla w)^2 \nabla w] + g_3 \nabla.[(\nabla w)^2 \nabla w] \tag{12}$$

Ce modèle a confirmé les résultats des études théoriques sur le modèle basé sur les équations de Newell-Whitehead à trois modes [9], montrant que la taille des domaines de même orientation se comporte bien en $\epsilon^{-\frac{1}{2}}$. Les frontières délimitant les zones d'orientations différentes sont formées de zones d'étirement et de défauts . Les défauts engendrés par des effets de bord [14] jouent un rôle prépondérant dans la dynamique en dessous de la rotation critique de l'instabilité de Küppers-Lortz. Le déplacement des défauts en convection avec rotation a été étudié numériquement par Rodriguez et al. (1994) [17] et (1995) [18].

Neufeld, Friedrich et Haken (1993) [12] ont dérivé un modèle de convection à nombre de Prandtl infini, autour du seuil de convection. Evaluant l'interaction des termes non linéaires dans l'espace spectral et simplifiant les opérateurs agissant sur le second harmonique, ils déterminent les coefficients devant les termes non linéaires. Cette approximation a été utilisée par Manneville (1983) [21] dans l'espace physique et elle est discutée par Roberts (1992) [19]. Le modèle de Neufeld, Friedrich et Haken dans le cadre de conditions aux limites libres s'écrit

$$\partial_t w = (\epsilon - (\Delta + 1)^2) w + w_s \Delta w + \nabla . (w_s \nabla w) - \tau \beta_{N.F.H} \nabla . (\hat{\mathbf{z}} \times w_s \nabla w) \tag{13}$$

avec $w_s = -w\Delta w + (\nabla w)^2$ et $\beta_{N.F.H} = \frac{1}{(\pi^2 + k_c^2)} \left[1 + \frac{6k_c^2(\pi^2+k_c^2)^2}{4\pi^2\tau^2+(4\pi^2)^3} \right]$. Avec ce modèle, l'instabilité de Küppers-Lortz apparaît pour une rotation critique proche du nombre de Taylor déterminé avec les équations primitives de Boussinesq.

Ces modèles de convection à caractère isotrope sont restreints à des nombres de Prandtl infinis.

Dans le chapitre B, la stabilité linéaire de rouleaux de convection à partir des équations primitives de Boussinesq est étudiée, pour des nombres de Prandtl finis et des conditions aux limites libres. Les modèles à nombres de Prandtl finis et le rôle du champ moyen dans des régimes avec rotation font l'objet du Chapitre C.

[1] S. Chandrasekhar *Proc. Roy. Soc.*, A **217**, 306, (1953).

[2] S. Chandrasekhar. "Hydrodynamic and Hydromagnetic Stability " *Oxford University Press* (1961)

[3] G. Küppers and D. Lortz "Transition from laminar convection to thermal turbulence in a rotating fluid layer", J. Fluid Mech. **35**, 609-620 (1969).

[4] G. Küppers, "The stability of steady finite amplitude convection in a rotating fluid layer", Phys. Lett. **32 A**, 7-8.(1970).

[5] F.H. Busse and K.E. Heikes, "Convection in a rotating layer: a simple case of turbulence", Science **208**, 173-174. (1980).

[6] K.E. Heikes and F.H. Busse "Weakly nonlinear turbulence in a rotating convection layer", *Annals N.Y Acadamy of sciences*, **357**, (1980)

[7] R. M. May, W. J. Leonard "Nonlinear aspect of competition between species", SIAM *J. Appl. Math*, **29**, 243-253, (1975).

[8] F.H. Busse "Transition to turbulence via the statistical limit route" , *Turbulence and Chaotic Phenomene in Fluids*,Tasumi ed. Elsevier Science Publishers B.V (North-Holland), 197-202 (1984).

[9] Yuhai. Tu and M. C. Cross "Chaotic Domain structure in Rotating convection", Phys. Rev. Let., **69**, 2515-2518, (1992).

[10] A. C. Newell and J.A Whitehead J. Fluid. Mech., **38**, 279, (1969).

[11] M.C. Cross, D. Meiron and Y. Tu, "Chaotic domain: A numérical investigation" *Chaos* **4**, 607 (1994).

[12] M. Neufeld, R. Friedrich and H Haken, "Order parameter equation and equation for high Prandtl number. Rayleigh-bénard convection in a rotating aspect ratio system", *Z. Phys.* **B 92**, 243 (1993); M. Fantz, R. Friedrich, M. Bestehorn and H. Haken, "Pattern formation in Bénard convection" Physica D **61** , 147-154, (1992).

[13] J. Millán- Rodríguez, C. Pérez-García, M. Bestehorn, M. Fantz, and R. Friedrich "Pattern formation in convection of rotating fluids with broken vertical symmetry", *Phys. Rev.*, **46**, 4729-4735, (1992).

[14] Fang Zhong and R. Ecke "Pattern dynamics and heat transport in rotating Rayleig-Bénard convection" *Chaos*, **2**, 163-171, (1992).

[15] Yuchou Hu, R. Ecke and Guenter Ahlers “Time and length scale in rotating Rayleigh-Bénard convection”, *Phys. Rev. Let.*, **74**, 5040-5043, (1995).

[16] J. Swift, P. C. Hohenberg,”Hydrodynamic fluctuations at the convective instability” *Phys. Rev.*, A **15**, 319, (1977).

[17] J. Millán- Rodríguez and C. Pérez-García “ Motion of defects in rotating fluid”, *Chaos*, **4**, (1994).

[18] J. Millán- Rodríguez, M. Bestehorn, C. Pérez-García, and R. Friedrich “Deffect motion in rotating fluids”, *Phys. Rev. Let*, **74**, (1995).

[19] A.J. Roberts, “The Swift-Hohenberg equation requires non-local modifications to model spatial pattern evolution of physical problems” *J. Austral. Math. Soc. Ser. B* **34**, 174 (1992).

[20] R.M. Clever and F.H. Busse, “Nonlinear properties of convection rolls in a horizontal layer rotating about a vertical axis”, J. Fluid Mech. **94**, 609-627 (1979).

[21] P. Manneville, ”A two-dimensional model for three-dimensional convective patterns in wide containers”, J.Physique **44**, 759-765 (1983).

Chapitre B

Stabilité des rouleaux de convection en présence de rotation, à nombre de Prandtl fini

L'étude de l'instabilité de Küppers-Lortz a débuté à nombre de Prandtl infini et dans le cas de conditions aux limites libres [1]. Cette instabilité est aussi présente à nombre de Prandtl fini, mais Swift (cité dans [9]) a noté l'existence d'une divergence du taux de croissance pour une perturbation sous forme de rouleaux presque parallèles aux rouleaux de base. L'origine de cette divergence était un problème ouvert. Nous nous sommes intéressés à ce problème en reconduisant l'asymptotique à nombre de Prandtl fini et dans le cas de conditions aux limites libres.

Nous avons construit une solution stationnaire sous forme de rouleaux par un calcul perturbatif près du seuil de convection. L'étude de la stabilité de cette solution stationnaire est faite pour une perturbation prise à l'ordre dominant sous la forme de rouleaux inclinés d'un angle θ par rapport à la direction des rouleaux stationnaires. Le taux de croissance de cette perturbation est déduit des conditions de solvabilité à chaque ordre.

Cette asymptotique reproduit la divergence remarquée par Swift. Mais elle permet aussi de localiser l'origine de cette divergence. A nombre de Prandtl fini, il existe un champ moyen à grande échelle qui déforme et déplace les textures. Dans ce calcul asymptotique, nous montrons que l'origine de la divergence provient de la fonction de courant de l'écoulement moyen qui est engendré par la force de Coriolis et diverge dans la limite des angles petits.

Pour des vecteurs d'onde d'orientation proches de la solution stationnaire, il faut donc chercher un taux de croissance et une fonction de courant du champ moyen à un ordre plus élevé que dans l'asymptotique précédente. Cela conduit à un calcul de couche limite angulaire. La nouvelle échelle de temps et la largeur de la couche limite sont prises de manière à raccorder le taux de croissance entre les différents domaines angulaires. Dans cette asymptotique, il faut considérer une fonction courant du champ moyen comme résultant d'un battement entre les rouleaux de bases et les rouleaux de la perturbation. L'amplitude de cette fonction de courant n'est pas définie. Ceci induit un degré de liberté supplémentaire, qui sera levé en considérant une condition de quasi-solvabilité supplémentaire, pour des termes proportionnels aux battements entre les rouleaux de bases et la perturbation, ne dépendant pas de la coordonnée verticale.

En effet, ce sont ces termes qui sont à l'origine de la divergence. Ils constituent un espace indépendant qui est résonnant pour des angles nuls et nécessitent une élimination par une condition de solvabilité supplémentaire. Cette approche non triviale permet le passage à la limite des angles nuls. Elle est analogue à l'analyse d'Ablowitz et Benney [11], dans le contexte de la théorie de Whitham, sur l'analyse de modulation d'ondes dispersives [12].

En additionnant à tous les ordres les conditions de solvabilité et, séparément les conditions de quasi-solvabilité, on obtient deux équations couplées liant le taux de croissance de la perturbation avec l'amplitude de la fonction de courant du champ moyen. On montre ainsi que l'une des deux valeurs propres de ce système, est toujours instable dans un domaine angulaire positif et qu'elle se raccorde avec la solution extérieure de la couche limite.

Ce calcul montre l'existence d'une instabilité pour des petits angles de perturbation en présence de faibles rotations et à nombre de Prandtl fini. Pour une rotation suffisante, l'instabilité de Küppers-Lortz est présente et peut coexister avec l'instabilité à petit angle. Mais à faible nombre de Prandtl, l'instabilité à petit angle et celle de Küppers-Lortz se confondent, rendant instable un large domaine angulaire.

Des simulations sur un modèle de convection dérivé dans le Chapitre 3 ont montré, une déstabilisation des rouleaux produite par des zones d'étirement de l'écoulement moyen conduisant à une précession des rouleaux, s'effectuant par petits sauts angulaires (Figure B.i). Les zones d'étirement se produisent à grande échelle, et cette dynamique ressemble à une instabilité de phase, du type instabilité variqueuse oblique ("skewed varicose"). Mais si l'on s'intéresse, au taux de croissance de l'instabilité à petit angle, on remarque qu'elle est plus rapide qu'une instabilité d'amplitude et de phase classique.

Par contre sans rotation, pour des conditions aux limites libres, Zippelius et Siggia (1983) [13], Busse et Bolton (1984) [14] ont montré l'existence d'une instabilité de phase du type “skewed varicose” qui est toujours présente pour des nombres d’onde supérieurs au nombre d’onde critique. Si l’on relie le taux de croissance de l’instabilité à petit angle avec le rapport d’aspect des rouleaux, on trouve un taux de croissance comparable à l’instabilité de phase trouvée sans rotation.

Pour pouvoir relier correctement l’instabilité d’amplitude à petit angle à cette instabilité de phase trouvée sans rotation, il a fallu construire et étudier un modèle de convection avec rotation à nombre de Prandtl fini.

Ce travail est exposé dans le chapitre C.

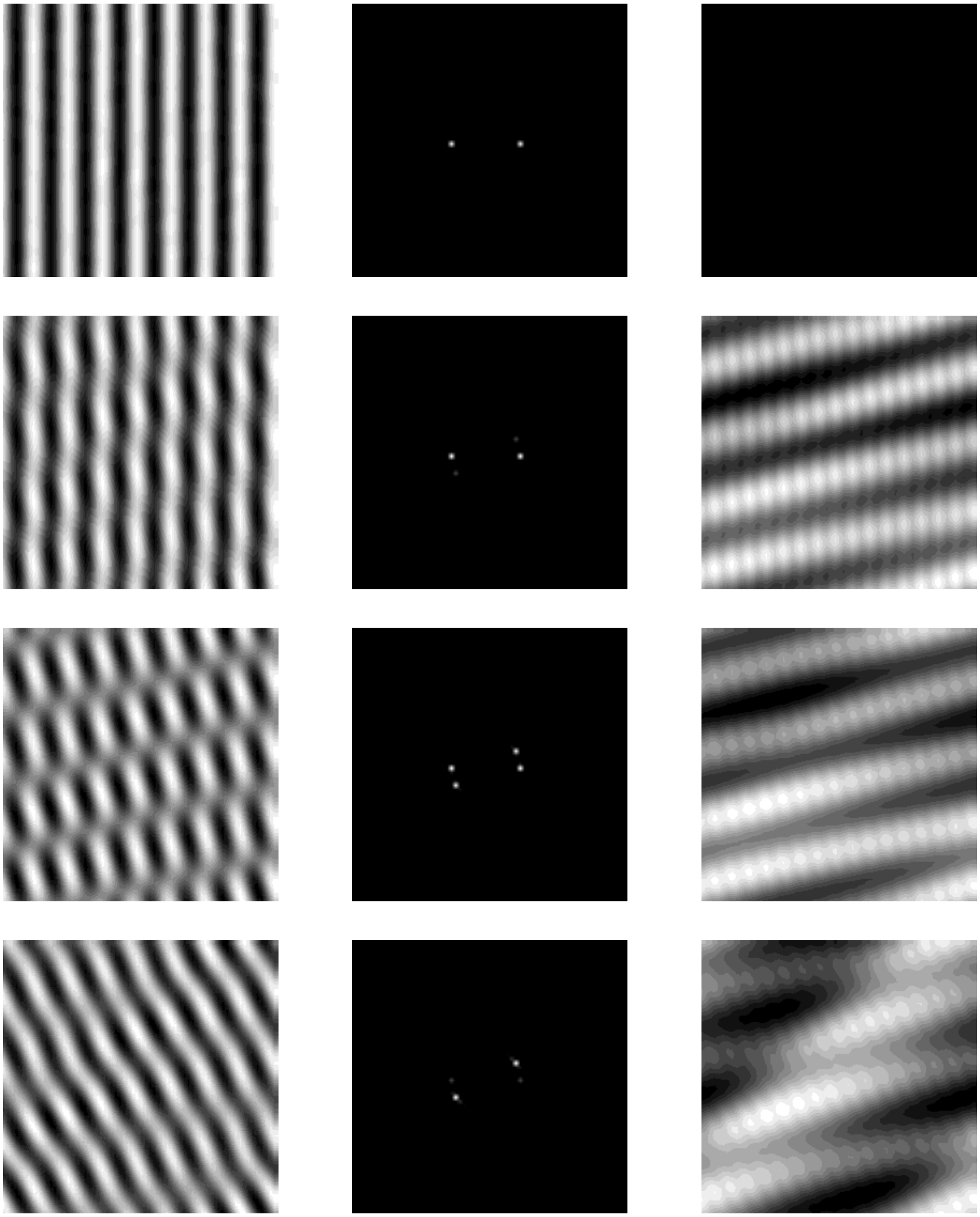

Figure B.i: Simulation numérique de rouleaux de convection subissant l'instabilité à petit angle, réalisée sur un modèle de convection dérivé dans le Chapitre 3, à nombre de Prandtl $P = 2$, pour une rotation faible $\tau = 10$, avec un écart au nombre de Rayleigh critique $\tilde{\epsilon} = 0.1$ et un nombre d'onde égal au nombre d'onde critique. La colonne de droite représente une évolution temporelle du mode convectif, celle du milieu représente son spectre bidimensionnel et la troisième la fonction de courant de l'écoulement moyen. La simulation a débuté sous forme de rouleaux droits perturbés de manière isotrope, par des rouleaux prenant toutes les orientations possibles et ayant de très faibles amplitudes.

A new instability for finite Prandtl number rotating convection with free-slip boundary conditions

Y. Ponty, T. Passot and P.L Sulem
CNRS URA 1362, Observatoire de la Côte d'Azur
B.P. 229, 06304 Nice Cedex 04, France

Phys. Fluid. **9**, *67 (1997).*

Abstract

Rolls in finite Prandtl number rotating convection with free-slip top and bottom boundary conditions are shown to be unstable with respect to small angle perturbations for any value of the rotation rate. This instability is driven by the horizontal mean flow whose estimation requires a special singular perturbation analysis.

PACS numbers: 47.27.Te, 47.20.Bp, 47.32.-y, 47.20.-Lz

1 Introduction

Rayleigh-Bénard convection in a plane layer heated from below and rotating about a vertical axis, has been the object of special attention motivated by both astrophysical and geophysical applications, and by the existence of additional instabilities occuring in this system. In the case of free-slip top and bottom boundary conditions, Küppers and Lortz [1] showed, using by a perturbation analysis near threshold, that when in an infinite Prandtl number fluid, the Taylor number (which measures the rotation rate) exceeds the critical value 2285, two-dimensional rolls are unstable with respect to perturbations of the form of a similar pattern rotated by an angle close to 58^o. This instability which is also present with no-slip boundaries [2], leads in the case of extended systems to the formation of chaotically evolving patches of parallel rolls [7], [3], [4], [5],[6].

Convection at moderate Prandtl number with no-slip top and bottom boundary conditions, was addressed in [8], [2] and [9], and the Küppers-Lortz instability was shown to occur at a critical Taylor number lower than in the infinite Prandtl number limit. Free-slip boundaries were considered by Swift (cited in [9]) who noted that the usual perturbative calculation of the growth rate leads to a divergence in the limit of perturbations quasi-parallel to the basic rolls. The present paper is mostly concerned with a revisited analysis of this problem, leading to a uniformly valid expression of the instability growth rate. We show in particular that for any finite Prandtl number and rotation rate, straight parallel rolls are unstable when the angle associated to the perturbation is small enough.

In Section 2, steady convective rolls in a rotating frame are constructed perturbatively near threshold. Section 3 is devoted to the computation of the instability growth rate for finite angle perturbation, an analysis which, at finite Prandtl number, breaks down in the small angle limit. In Section 4, we present a special analysis in the resulting small angle "boundary layer", where the interaction of the basic rolls with quasi-parallel perturbations leads to almost space-independent contributions which become resonant in the zero angle limit. These terms are removed by prescribing a quasi-solvability condition the marginal mode of quasi-constant horizontal velocity. A uniform expression for the instability growth rate is then derived and a new "small-angle instability" is obtained. The sensitivity of the instability growth rate to the Prandtl and Taylor numbers is analyzed. Qualitative features of this instability and its nonlinear development are briefly described in Section 5.

2 Steady convective rolls in a rotating frame

The Boussinesq equations in a horizontal fluid layer heated from below and rotating around a vertical axis $\hat{\mathbf{z}}$, are written in the non-dimensional form

$$\Delta\mathbf{u} + \hat{\mathbf{z}}\vartheta - \nabla\Gamma - \tau\hat{\mathbf{z}} \times \mathbf{u} = {P_r}^{-1}(\mathbf{u}.\nabla\mathbf{u} + \frac{\partial}{\partial t}\mathbf{u}) \tag{1}$$

$$\nabla.\mathbf{u} = 0 \tag{2}$$

$$\Delta\vartheta + R_a\hat{\mathbf{z}}.\mathbf{u} = \mathbf{u}.\nabla\vartheta + \frac{\partial}{\partial t}\vartheta, \tag{3}$$

where the vertical diffusion time is taken as time unit. We assume a Prandtl number $P_r > 0.6766$, to prevent over-stability [10]. The other parameters are the Rayleigh number R_a and the square root τ of the Taylor number (equal to twice the Rossby number) which, to be specific, is taken positive (anti-clockwise rotation).

Proceeding as in [1], we introduce the operators $\Lambda = \nabla \times (\nabla \times .)$ and $\Upsilon = \nabla \times .$, and express the velocity $\mathbf{u} = (u, v, w)^t$ in terms of two scalar fields ϕ and ψ, in the form $\mathbf{u} = \Lambda(\phi\hat{\mathbf{z}}) + \Upsilon(\psi\hat{\mathbf{z}}) = (\partial_z\partial_x\phi + \partial_y\psi, \partial_z\partial_y\phi - \partial_x\psi, -\Delta_h\phi)^t$, where $\Delta_h = \partial_{xx} + \partial_{yy}$. Applying the operators $\hat{\mathbf{z}}.\Lambda$ and $\hat{\mathbf{z}}.\Upsilon$ on eqs. (1)-(3), we obtain

$$(U + R_aG)X = Q(X,X) + \frac{\partial}{\partial t}VX, \tag{4}$$

with

$$X = \begin{bmatrix} \phi \\ \psi \\ \vartheta \end{bmatrix}, \; Q(X,X') = \begin{bmatrix} {P_r}^{-1}\hat{\mathbf{z}}.\Lambda(\mathbf{u}\cdot\nabla\mathbf{u}') \\ -{P_r}^{-1}\hat{\mathbf{z}}.\Upsilon(\mathbf{u}\cdot\nabla\mathbf{u}') \\ \mathbf{u}\cdot\nabla\vartheta' \end{bmatrix}, \; G = \begin{bmatrix} 0 & 0 & 0 \\ 0 & 0 & 0 \\ -\Delta_h & 0 & 0 \end{bmatrix},$$

$$U = \begin{bmatrix} \Delta^2\Delta_h & -\tau\partial_z\Delta_h & -\Delta_h \\ \tau\partial_z\Delta_h & \Delta\Delta_h & 0 \\ 0 & 0 & \Delta \end{bmatrix}, \; V = \begin{bmatrix} {P_r}^{-1}\Delta\Delta_h & 0 & 0 \\ 0 & {P_r}^{-1}\Delta_h & 0 \\ 0 & 0 & 1 \end{bmatrix}.$$

For free-slip boundary conditions, $\vartheta = \phi = \partial_{zz}\phi = \partial_z\psi = 0$ in the planes $z = \pm\frac{1}{2}$.

A stationary solution of eq. (4) is computed perturbatively near the convection threshold by expanding $R_a = R_0 + \epsilon R_1 + \epsilon^2 R_2 + \cdots$ and $X = \epsilon X_1 + \epsilon^2 X_2 + \epsilon^3 X_3 + \cdots$. or, more explicitly, when taking into account the boundary conditions satisfied by the individual components,

$$\phi = \epsilon\phi_1 \cos\pi z + \epsilon^2\phi_2 \sin 2\pi z + \cdots \tag{5}$$

$$\psi = \epsilon\psi_1 \sin\pi z + \epsilon^2(\psi_0 + \psi_2 \cos 2\pi z) + \cdots \tag{6}$$

$$\vartheta = \epsilon\vartheta_1 \cos\pi z + \epsilon^2\vartheta_2 \sin 2\pi z + \cdots. \tag{7}$$

Introducing the linear operator $L = U + R_0G$, we get at the successive orders of the expansion,

$$LX_1 = 0 \tag{8}$$

$$LX_2 = -R_1GX_1 + Q(X_1, X_1) \tag{9}$$

$$LX_3 = -(R_1GX_2 + R_2GX_1) + Q(X_1, X_2) + Q(X_2, X_1). \tag{10}$$

For a solution in the form of two-dimensional rolls with a critical wavenumber $|\vec{k}_1| = k$, given by the real solution of

$$2(\frac{k^2}{\pi^2})^3 + 3(\frac{k^2}{\pi^2})^2 = 1 + \frac{\tau^2}{\pi^4}, \tag{11}$$

the critical Rayleigh number is $R_0 = \frac{(k^2+\pi^2)^3+\tau^2\pi^2}{k^2}$ [10]. To simplify the writing, we denote by

$$Z(\alpha, \beta, \gamma) = (\alpha \cos \pi z, \beta \sin \pi z, \gamma \cos \pi z)^t, \tag{12}$$

vectors corresponding to fundamental modes in the vertical direction and obeying the boundary conditions prescribed on X. An element of the null space of L is then given by

$$v(\vec{k}) = Z(c_1, c_2, c_3)e^{i\vec{k}.\vec{x}}, \tag{13}$$

with $c_1 = 1, \quad c_2 = -\frac{\tau\pi}{k_p^2}, \quad c_3 = \frac{R_0k^2}{k_p^2}$, and $k_p^2 = k^2 + \pi^2 = \sqrt{\frac{R_0}{3}}$, and the leading order solution reads

$$X_1 = Av(\vec{k}_1) + c.c., \tag{14}$$

where the amplitude A will be determined by a solvability condition arising at a higher order. For this purpose, it is convenient to introduce the inner product

$$\langle X, X' \rangle = R_0 \int \phi^*\phi' d\vec{x} + R_0 \int \psi^*\psi' d\vec{x} + \int \vartheta^*\vartheta' d\vec{x}, \tag{15}$$

for which the operator L is self-adjoint.

Using the notation

$$Q(X_i, X_j) + Q(X_j, X_i) = (1 + \delta_{ij})(Q^{(1)}_{i,j}, Q^{(2)}_{i,j}, Q^{(3)}_{i,j})^t, \tag{16}$$

we have in eq. (9),

$$Q(X_1, X_1) = \begin{bmatrix} Q^{(1)}_{1,1} \\ Q^{(2)}_{1,1} \\ Q^{(3)}_{1,1} \end{bmatrix} = \begin{bmatrix} 0 \\ 2\frac{\tau}{P_r}\pi^2\frac{k^4}{k_p^2}(A^2e^{2i\vec{k}_1.\vec{x}} + c.c.) \\ -2R_0\pi\frac{k^4}{k_p^2}\sin 2\pi z|A|^2 \end{bmatrix}. \tag{17}$$

The solvability condition for eq. (9) (obtained by taking the inner product of this equation with $v(\vec{k}_1)$), requires $R_1 = 0$. Defining the operator $P = \Delta^3 + \tau^2\partial_{zz} - R_0\Delta_h$, eq. (9) reduces to

$$\Delta_h P\phi_2 = \Delta Q^{(1)}_{1,1} + \tau\partial_z Q^{(2)}_{1,1} + \Delta_h Q^{(3)}_{1,1}. \tag{18}$$

where the right hand side vanishes identically. We thus get $\Delta_h\phi_2 = 0$, since elements of the null space of P, already included in ϕ_1, are not needed in ϕ_2.

For the two other components of X_2, one easily checks that $\psi_2 = 0$, $\psi_0 = \Psi_0 e^{2i\vec{k}_1.\vec{x}} + c.c.$ and $\vartheta_2 = \Theta_2$ with $\Psi_0 = \frac{\tau\pi^2}{8P_r k_p^2}A^2$ and $\Theta_2 = \frac{R_0 k^4}{2\pi k_p^2}|A|^2$. This enable us to compute

$$Q(X_1, X_2) + Q(X_2, X_1) = \left(\begin{array}{l} 0 \\ \frac{4k^4\pi}{P_r}\Psi_0(A^* e^{i\vec{k}_1.\vec{x}} - 3Ae^{3i\vec{k}_1.\vec{x}})\sin\pi z + c.c. \\ 2\pi k^2\Theta_2 A e^{i\vec{k}_1.\vec{x}}\cos\pi z\cos 2\pi z + c.c. \end{array}\right).$$

The solvability condition of eq. (10) then reduces to $R_2 = r_2|A|^2$ or equivalently, $\epsilon^2|A|^2 = \frac{R_a - R_0}{r_2}$, with $r_2 = \frac{1}{2k_p^2}(R_0 k^4 - \frac{\tau^2\pi^4}{P_r{}^2})$, which completes the computation of the roll amplitude in terms of the distance to threshold.

3 The Küppers-Lortz instability

We assume that the steady rolls of wavevector $\vec{k}_1$ computed in Section 2 are subject to a perturbation $\tilde{X}$ in the form of rolls with an infinitesimal amplitude and a wavevector $\vec{k}_2$ making with $\vec{k}_1$ an angle θ that it is enough to consider in the range $]-\frac{\pi}{2}, \frac{\pi}{2}]$. We assume for the sake of simplicity that the wavenumbers $|\vec{k}_1|$ and $|\vec{k}_2|$ are critical. When real, the growth rate σ of this perturbation is given by

$$(U + R_a G)\tilde{X} = Q(X, \tilde{X}) + Q(\tilde{X}, X) + \sigma V\tilde{X}. \tag{19}$$

In order to compute $\sigma = \epsilon\sigma_1 + \epsilon^2\sigma_2 + \cdots$ perturbatively near threshold, we also expand $\tilde{X} = \tilde{X}_1 + \epsilon\tilde{X}_2 + \epsilon^2\tilde{X}_3 + \cdots$ or, for the individual components,

$$\tilde{\phi} = \tilde{\phi}_1\cos\pi z + \epsilon\tilde{\phi}_2\sin 2\pi z + \cdots \tag{20}$$

$$\tilde{\psi} = \tilde{\psi}_1\sin\pi z + \epsilon(\tilde{\psi}_0 + \tilde{\psi}_2\cos 2\pi z) + \cdots \tag{21}$$

$$\tilde{\vartheta} = \tilde{\vartheta}_1\cos\pi z + \epsilon\tilde{\vartheta}_2\sin 2\pi z + \cdots. \tag{22}$$

Equation (19) leads to

$$L\tilde{X}_1 = 0 \tag{23}$$

$$L\tilde{X}_2 = Q(X_1, \tilde{X}_1) + Q(\tilde{X}_1, X_1) + \sigma_1 V\tilde{X}_1 \tag{24}$$

$$\begin{aligned} L\tilde{X}_3 = {} & Q(X_2, \tilde{X}_1) + Q(\tilde{X}_1, X_2) + Q(X_1, \tilde{X}_2) + Q(\tilde{X}_2, X_1) \\ & +\sigma_1 V\tilde{X}_2 + \sigma_2 V\tilde{X}_1 - R_2 G\tilde{X}_1. \end{aligned} \tag{25}$$

Using a notation similar to (16), we define

$$Q(X_i,\tilde{X}_j)+Q(\tilde{X}_j,X_i)=Q_{i,\tilde{j}}=(Q^{(1)}_{i,\tilde{j}},Q^{(2)}_{i,\tilde{j}},Q^{(3)}_{i,\tilde{j}})^t. \tag{26}$$

Writing the solution of eq. (23) in the form $\tilde{X}_1 = Bv(\vec{k}_2)+c.c.$, where B is an arbitrary constant, we have in the right hand side of eq. (24),

$$Q_{1,\tilde{1}} = \begin{pmatrix} \frac{j_1}{P_r}\delta_h^+\delta_h^-(AB^*e^{i\vec{k}^-.\vec{x}}+ABe^{i\vec{k}^+.\vec{x}})\sin 2\pi z + c.c. \\ \frac{j_2}{P_r}(\delta_h^- AB^*e^{i\vec{k}^-.\vec{x}}+\delta_h^+ ABe^{i\vec{k}^+.\vec{x}}) + c.c. \\ j_3(\delta_h^+ AB^*e^{i\vec{k}^-.\vec{x}}+\delta_h^- ABe^{i\vec{k}^+.\vec{x}})\sin 2\pi z + c.c. \end{pmatrix}, \tag{27}$$

where we have introduced the wavevectors

$$\vec{k}^\pm = \vec{k}_1 \pm \vec{k}_2, \tag{28}$$

and defined the numerical constants

$$j_1 = -\frac{3}{2}\pi k^2, \quad j_2 = -\frac{\tau\pi^2 k^2}{k_p^2}, \quad j_3 = \frac{R_0 k^2 \pi}{2k_p^2}. \tag{29}$$

Furthermore, the coefficient $\delta_h^\pm$, given by $\Delta_h e^{i\vec{k}^\pm.\vec{x}} = \delta_h^\pm e^{i\vec{k}^\pm.\vec{x}}$, read

$$\delta_h^+ = -4k^2\cos^2\frac{\theta}{2}, \quad \delta_h^- = -4k^2\sin^2\frac{\theta}{2}. \tag{30}$$

Since $\langle v(\vec{k}_2), Q(X_1,\tilde{X}_1)+Q(\tilde{X}_1,X_1)\rangle = 0$, while $\langle v(\vec{k}_2), V\tilde{X}_1\rangle \neq 0$, the solvability condition for eq. (24) implies $\sigma_1 = 0$. Straightforward algebra then leads to

$$P\Delta_h\tilde{\phi}_2 = \Delta Q^{(1)}_{1,\tilde{1}} + \tau\partial_z Q^{(2)}_{1,\tilde{1}} + \Delta_h Q^{(3)}_{1,\tilde{1}} \tag{31}$$

$$\Delta\Delta_h\tilde{\psi}_2 = -\tau\partial_z\Delta_h\tilde{\phi}_2 \tag{32}$$

$$\Delta\Delta_h\tilde{\psi}_0 = Q^{(2)}_{1,\tilde{1}} \tag{33}$$

$$\Delta\tilde{\vartheta}_2 = Q^{(3)}_{1,\tilde{1}} + R_0\Delta_h\tilde{\phi}_2. \tag{34}$$

Solving in the form

$$\tilde{\phi}_2 = \tilde{\Phi}_2^+ ABe^{i\vec{k}^+.\vec{x}} + \tilde{\Phi}_2^- AB^*e^{i\vec{k}^-.\vec{x}} + c.c. \tag{35}$$

$$\tilde{\psi}_2 = \tilde{\Psi}_2^+ ABe^{i\vec{k}^+.\vec{x}} + \tilde{\Psi}_2^- AB^*e^{i\vec{k}^-.\vec{x}} + c.c. \tag{36}$$

$$\tilde{\psi}_0 = \tilde{\Psi}_0^+ ABe^{i\vec{k}^+.\vec{x}} + \tilde{\Psi}_0^- AB^*e^{i\vec{k}^-.\vec{x}} + c.c. \tag{37}$$

$$\tilde{\vartheta}_2 = \tilde{\Theta}_2^+ ABe^{i\vec{k}^+.\vec{x}} + \tilde{\Theta}_2^- AB^*e^{i\vec{k}^-.\vec{x}} + c.c., \tag{38}$$

we get

$$\begin{array}{llll}
\tilde{\Phi}_2^+ & = \frac{\delta_h^-}{p^+}(\frac{j_1}{P_r}\delta^+ + j_3) & \tilde{\Phi}_2^- & = \frac{\delta_h^+}{p^-}(\frac{j_1}{P_r}\delta^- + j_3) \\
\tilde{\Psi}_2^+ & = -2\pi\tau\frac{\delta_h^-}{p^+\delta^+}(\frac{j_1}{P_r}\delta^+ + j_3) & \tilde{\Psi}_2^- & = -2\pi\tau\frac{\delta_h^+}{p^-\delta^-}(\frac{j_1}{P_r}\delta^- + j_3) \\
\tilde{\Psi}_0^+ & = \frac{j_2}{P_r\delta_h^+} & \tilde{\Psi}_0^- & = \frac{j_2}{P_r\delta_h^-} \\
\tilde{\Theta}_2^+ & = R_0\frac{\delta_h^+\delta_h^-}{p^+\delta^+}(\frac{j_1}{P-r}\delta^+ + j_3) + j_3\frac{\delta_h^-}{\delta^+} & \tilde{\Theta}_2^- & = R_0\frac{\delta_h^+\delta_h^-}{p^-\delta^-}(\frac{j_1}{P_r}\delta^- + j_3) + j_3\frac{\delta_h^+}{\delta^-}\ .
\end{array}$$

The coefficient $\delta^\pm$ and $p^\pm$ defined by the condition $\Delta e^{i\vec{k}^\pm.\vec{x}}T(2\pi z) = \delta^\pm e^{i\vec{k}^\pm.\vec{x}}T(2\pi z)$ and $Pe^{i\vec{k}^\pm.\vec{x}}T(2\pi z) = p^\pm e^{i\vec{k}^\pm.\vec{x}}T(2\pi z)$, (where the function T stands for sine or cosine), are given by

$$\delta^+ = -[4\pi^2 + 4k^2\cos^2\frac{\theta}{2}], \tag{39}$$

$$\delta^- = -[4\pi^2 + 4k^2\sin^2\frac{\theta}{2}], \tag{40}$$

$$p^+ = -[4\pi^2 + 4k^2\cos^2\frac{\theta}{2}]^3 - 4\pi^2\tau^2 + 4k^2R_0\cos^2\frac{\theta}{2}, \tag{41}$$

$$p^- = -[4\pi^2 + 4k^2\sin^2\frac{\theta}{2}]^3 - 4\pi^2\tau^2 + 4k^2R_0\sin^2\frac{\theta}{2}, \tag{42}$$

where the $\cos^2\frac{\theta}{2}$ and $\sin^2\frac{\theta}{2}$ contributions result from the action of the horizontal Laplacian on $e^{i\vec{k}^+.\vec{x}}$ and $e^{i\vec{k}^-.\vec{x}}$ respectively.

An important observation is that the contribution $\tilde{\Psi}_0^- AB^* e^{i\vec{k}^-.\vec{x}}$ to $\tilde{\psi}_2$ (which disappears at infinite Prandtl number) diverges in the limit $\theta \to 0$, where it can be viewed as associated to a "mean flow" generated by the rotation. This term is specific to free-slip boundary conditions and has no equivalent when rigid boundaries are considered. The divergence originates from the fact that in eqs. (31)-(34), the dynamics of the mean flow is slaved to that of the leading convective mode. This "adiabatic approximation" is valid at finite θ but breaks down in an "angular boundary layer" near $\theta = 0$, where time derivatives become relevant. Postponing to Section 4 the analysis of this layer, we derive here the solvability condition of eq. (25) for finite θ, by writing

$$\langle v(\vec{k}_2), G\tilde{X}_1\rangle = \frac{1}{2}c_1c_3k^2B^* \tag{43}$$

$$\langle v(\vec{k}_2), V\tilde{X}_1\rangle = \frac{1}{2}(R_0{P_r}^{-1}c_1^2k^2{k_p}^2 - R_0{P_r}^{-1}c_2^2k^2 + c_3^2)B^* \tag{44}$$

$$\langle v(\vec{k}_2), (Q(X_2, \tilde{X}_1) + Q(\tilde{X}_1, X_2)\rangle = \frac{1}{4}c_1^2c_3^2k^4|A|^2B^*. \tag{45}$$

Furthermore

$$Q(X_1, \tilde{X}_2) + Q(\tilde{X}_2, X_1) = Z(q_{1,\tilde{2}}^{(1)}, q_{1,\tilde{2}}^{(2)}, q_{1,\tilde{2}}^{(3)})|A|^2B^*e^{-i\vec{k}_2.\vec{x}} + c.c. + F_3, \tag{46}$$

where F_3 refers to non resonant terms proportional to $\sin 3\pi z$ or $\cos 3\pi z$. We also have

$$\begin{aligned}
q^{(1)}_{1,\tilde 2} &= \frac{k^4}{2P_r}\sin\theta[(-\tilde\Psi_2^+ + 2\tilde\Psi_0^-)(c_1\pi^2 - c_1k^2 - 2c_1\pi^2\cos\theta - 2c_2\pi\sin\theta)\\
&\quad +(\tilde\Psi_2^- - 2\tilde\Psi_0^+)(c_1\pi^2 - c_1k^2 + 2c_1\pi^2\cos\theta + 2c_2\pi\sin\theta)\\
&\quad +2\tilde\Phi_2^- k_p^2(c_2(1-\cos\theta) + \pi c_1\sin\theta) - 2\tilde\Phi_2^+ k_p^2(c_2(1+\cos\theta) - \pi c_1\sin\theta)]
\end{aligned} \tag{47}$$

$$\begin{aligned}
q^{(2)}_{1,\tilde 2} &= -\frac{k^4}{2P_r}[2\tilde\Psi_0^-(c_1\pi(-1+2\cos\theta-\cos 2\theta) + c_2(\sin\theta - \sin 2\theta))\\
&\quad +2\tilde\Psi_0^+(c_1\pi(-1-2\cos\theta-\cos 2\theta) - c_2(\sin\theta+\sin 2\theta))\\
&\quad +\tilde\Psi_2^+\sin\theta(-2c_1\pi\sin\theta + c_2(1+2\cos\theta))\\
&\quad +\tilde\Psi_2^-\sin\theta(-2c_1\pi\sin\theta - c_2(1-2\cos\theta))\\
&\quad +\tilde\Phi_2^+(c_2\pi(1-\cos 2\theta) - \pi^2c_1(2\sin\theta - \sin 2\theta))\\
&\quad +\tilde\Phi_2^-(c_2\pi(1-\cos 2\theta) + \pi^2c_1(2\sin\theta + \sin 2\theta))]
\end{aligned} \tag{48}$$

$$\begin{aligned}
q^{(3)}_{1,\tilde 2} &= \frac{k^2}{2}[\tilde{\Theta}_2{}^-(c_1\pi(1+\cos\theta) + c_2\sin\theta) + \tilde{\Theta}_2{}^+(c_1\pi(1-\cos\theta) - c_2\sin\theta)]\\
&\quad +\frac{k^2}{2}c_3[\tilde\Psi_2^+ + 2\tilde\Psi_0^+ - \tilde\Psi_2^- - 2\tilde\Psi_0^-]\sin\theta.
\end{aligned} \tag{49}$$

It follows that

$$\langle v(\vec{k}_2), Q(X_1,\tilde{X}_2) + Q(\tilde{X}_2, X_1)\rangle = \frac{1}{2}(R_0c_1q^{(1)}_{1,\tilde 2} + R_0c_2q^{(2)}_{1,\tilde 2} + c_3q^{(3)}_{1,\tilde 2})|A|^2B^*, \tag{50}$$

and finally

$$\sigma = \epsilon^2\sigma_2 = \epsilon^2\frac{r_2c_1c_3k^2 - (\frac{1}{2}c_1^2c_3^2k^4 + R_0c_1q^{(1)}_{1,\tilde 2} + R_0c_2q^{(2)}_{1,\tilde 2} + c_3q^{(3)}_{1,\tilde 2})}{R_0{P_r}^{-1}c_1^2k^2{k_p}^2 - R_0{P_r}^{-1}c_2^2k^2 + c_3^2}|A|^2, \tag{51}$$

where $\epsilon^2|A|^2$ can be expressed as $\frac{2k_p^2}{R_0k^4 - \frac{\tau^2\pi^4}{P_r^2}}(R_a - R_0)$.

Since in the limit $\theta \to 0$, $\tilde\Psi_0^-$ diverges like $\sin^{-2}\frac{\theta}{2}$, the quantity $q^{(l)}_{1,\tilde 2}$ with $l = 1,2,3$, scales like $\sin\frac{\theta}{2}\tilde\Psi_0^- \sim \sin^{-1}\frac{\theta}{2}$, and the growth rate behaves like

$$\sigma \sim \frac{\tau\pi^2k^2|A|^2}{2k_p^2P_r}\frac{\epsilon^2}{\sin\frac{\theta}{2}}, \tag{52}$$

indicating a breakdown of the above asymptotics at finite Prandtl numbers, in the case of small angle perturbations.

Pushing the θ-expansion at the next order, (as needed in Section 4), we write

$$\sigma \sim [-\eta + \frac{\tau\pi^2k^2}{2k_p^2P_r}(2\xi + \frac{1}{\sin\frac{\theta}{2}})]\epsilon^2|A|^2, \tag{53}$$

with

$$\eta = \frac{r_2}{R_0} \frac{k_p^2}{(1 + \frac{1}{P_r}(1 - \frac{2\tau^2\pi^2}{R_0 k^2}))} \tag{54}$$

and

$$\xi = -\frac{\tau\pi^2}{P_r k_p^2 k^2 (1 + \frac{1}{P_r}(1 - \frac{2\tau^2\pi^2}{R_0 k^2}))}, \tag{55}$$

the latter coefficient collecting contributions originating from $\tilde{\Psi}_0^-$.

The divergence shown in eq. (52) was noted in [9]. It indicates that the above analysis should be viewed as an outer expansion, and that a different scaling is required for small θ. In the following, the growth rate given by eq. (51) will thus be denoted σ_{outer}.

4 The small-angle instability

The small angle divergence of the stream function $\psi_0 \sim \epsilon \sin^{-2}\frac{\theta}{2}$ and of the growth rate $\sigma_{outer} \sim \epsilon^2 \sin^{-1}\frac{\theta}{2}$, indicates that new scalings in ϵ are expected in an angular boundary layer near $\theta = 0$. Denoting by ϵ^α the thickness of this layer, by ϵ^β the amplitude of Ψ_0 and by ϵ^γ the magnitude of the growth rate in this layer, the matching of the "outer" and "inner" regions requires $\beta = 1 - 2\alpha$ and $\gamma = 2 - \alpha$. Since, in the inner region, the time derivative in the mean flow equation (whose presence will remove the divergence) becomes comparable to the viscous term when $\gamma = 2\alpha$, we get $\alpha = \frac{2}{3}$, $\beta = -\frac{1}{3}$ and $\gamma = \frac{4}{3}$.

Furthermore, when expanding eq. (4) inside the boundary layer, the parameter ϵ appears not only through the horizontal Fourier modes of X_1 whose amplitudes scale like entire powers of ϵ, but also through the angular dependence of the operators involved in this equation. We are thus led to expand

$$\sigma = \epsilon\sigma_1 + \epsilon^{\frac{4}{3}}\sigma_{\frac{4}{3}} + \epsilon^{\frac{5}{3}}\sigma_{\frac{5}{3}} + \epsilon^2\sigma_2 + \epsilon^{\frac{7}{3}}\sigma_{\frac{7}{3}} + \epsilon^{\frac{8}{3}}\sigma_{\frac{8}{3}} + \cdots \tag{56}$$

and

$$\begin{aligned}\tilde{X} = {} & \epsilon^{-\frac{1}{3}}\tilde{Y}_{-\frac{1}{3}} + \tilde{Y}_0 + \tilde{X}_1 + \epsilon^{\frac{1}{3}}\tilde{Y}_{\frac{1}{3}} + \epsilon^{\frac{2}{3}}\tilde{Y}_{\frac{2}{3}} + \epsilon\tilde{X}_2 + \epsilon^{\frac{4}{3}}\tilde{X}_{\frac{4}{3}} + \epsilon^{\frac{5}{3}}\tilde{X}_{\frac{5}{3}} \\ & + \epsilon^2\tilde{X}_3 + \epsilon^{\frac{7}{3}}\tilde{X}_{\frac{7}{3}} + \epsilon^{\frac{8}{3}}\tilde{X}_{\frac{8}{3}} + \epsilon^3\tilde{X}_4 + \cdots \end{aligned} \tag{57}$$

where terms of the form $\tilde{Y}_\mu = \tilde{\Psi}_\mu B^* A e^{i\vec{k}^-.\vec{x}}(0,1,0)^t + c.c.$, are introduced to cancel almost resonant contributions resulting from the interaction of the basic rolls with quasi-parallel perturbations. As seen later, in the boundary layer, σ can be complex.

Substituting (57) and (56) in eq. (19) and concentrating on perturbations such that the angle θ between the wavevectors $\vec{k}_1$ and $\vec{k}_2$ is of order $\epsilon^{\frac{2}{3}}$, we obtain the following hierarchy.

- At order ϵ^0,

$$L\tilde{X}_1 = 0, \tag{58}$$

leading to

$$\tilde{X}_1 = v(\vec{k}_2)B + c.c.. \tag{59}$$

- At order ϵ,

$$L\tilde{X}_2 = \begin{pmatrix} 0 \\ -\frac{4j_2k^2}{P_r}ABe^{i\vec{k}^+.\vec{x}} \\ -4j_3k^2AB^*e^{i\vec{k}^-.\vec{x}}\sin 2\pi z \end{pmatrix} + \sigma_1 BVv(\vec{k}_2) + c.c.\ . \tag{60}$$

The solvability condition reads

$$\epsilon\sigma_1 = 0, \tag{61}$$

and the solution is given by

$$\tilde{X}_2 = \begin{pmatrix} 0 \\ \tilde{\Psi}_0^+ABe^{i\vec{k}^+.\vec{x}} \\ \tilde{\Theta}_2{}^-AB^*e^{i\vec{k}^-.\vec{x}}\sin 2\pi z \end{pmatrix} + c.c. \tag{62}$$

with $\tilde{\Psi}_0^+ = -\frac{j_2}{4k^2P_r}$ and $\tilde{\Theta}_2^- = j_3\frac{k^2}{\pi^2}$.

- At order $\epsilon^{\frac{4}{3}}$,

$$\begin{aligned} \epsilon^{\frac{4}{3}}L\tilde{X}_{\frac{4}{3}} &= \epsilon^{\frac{2}{3}}\sin\theta\tilde{\Psi}^*_{-\frac{1}{3}}|A|^2Be^{i\vec{k_2}.\vec{x}}Z(-\frac{k^4k_p^2}{P_r}, \frac{k^4c_2}{P_r}, -k^2c_3) \\ &+\epsilon^{\frac{4}{3}}\sigma_{\frac{4}{3}}VBv(\vec{k}_2) + c.c. + \mathcal{NR}, \end{aligned} \tag{63}$$

where $\mathcal{NR}$ collects non-resonant terms. The solvability condition is

$$\epsilon^{\frac{4}{3}}\sigma_{\frac{4}{3}} = \epsilon k^2\sin\theta|A|^2\epsilon^{-\frac{1}{3}}\tilde{\Psi}^*_{-\frac{1}{3}}. \tag{64}$$

- At order $\epsilon^{\frac{5}{3}}$,

$$\begin{aligned} \epsilon^{\frac{5}{3}}L\tilde{X}_{\frac{5}{3}} &= \epsilon\sin\theta\tilde{\Psi}^*_0|A|^2Be^{i\vec{k_2}.\vec{x}}Z(-\frac{k^4k_p^2}{P_r}, \frac{k^4c_2}{P_r}, -k^2c_3) \\ &+\epsilon^{\frac{5}{3}}\sigma_{\frac{5}{3}}VBv(\vec{k}_2) + c.c. + \mathcal{NR}. \end{aligned} \tag{65}$$

The solvability of this equation requires

$$\epsilon^{\frac{5}{3}}\sigma_{\frac{5}{3}} = \epsilon k^2 \sin\theta |A|^2 \tilde{\Psi}_0^*. \tag{66}$$

- At order ϵ^2,

$$\begin{aligned}\epsilon^2 L\tilde{X}_3 = {} & \epsilon^2 Q_{\tilde{1},2} + \epsilon^2 Z(\bar{q}^{(1)}_{1,\tilde{2}}, \bar{q}^{(2)}_{1,\tilde{2}}, \bar{q}^{(3)}_{1,\tilde{2}})|A|^2 B e^{i\vec{k_2}.\vec{x}} \\ & +\epsilon^{\frac{2}{3}} \sin\theta \tilde{\Psi}^*_{-\frac{1}{3}} e^{i\vec{k_2}.\vec{x}} |A|^2 BZ(-2\frac{k^4}{P_r} c_2 \pi \sin\theta \ , \frac{k^4}{P_r} c_1 \pi (\sin\frac{\theta}{2} - \sin\frac{3\theta}{2}) \ , 0) \\ & +\epsilon^{\frac{4}{3}} \sin\theta \tilde{\Psi}^*_{\frac{1}{3}} |A|^2 B e^{i\vec{k_2}.\vec{x}} Z(-\frac{k^4 k_p^2}{P_r}, \frac{k^4 c_2}{P_r}, -k^2 c_3) \\ & -\epsilon^2 R_2 G\tilde{X}_1 + \epsilon^2 \sigma_2 V B v(\vec{k_2}) + c.c. + \mathcal{NR},\end{aligned} \tag{67}$$

where

$$(\bar{q}^{(1)}_{1,\tilde{2}}, \bar{q}^{(2)}_{1,\tilde{2}}, \bar{q}^{(3)}_{1,\tilde{2}}) = (0, 4\frac{k^4}{P_r} c_1 \pi \tilde{\Psi}_0^+, k^2 c_1 \pi \tilde{\Theta}_2^-) \tag{68}$$

denotes the limit as $\theta \to 0$ of the vector $(q^{(1)}_{1,\tilde{2}}, q^{(2)}_{1,\tilde{2}}, q^{(3)}_{1,\tilde{2}})$ from which the contributions coming from Ψ_0^- have been removed. The solvability condition reads

$$\epsilon^2 \sigma_2 = -\eta |A|^2 \epsilon^2 + 2\epsilon^{\frac{2}{3}} \xi k^2 \sin\theta \sin\frac{\theta}{2} |A|^2 \tilde{\Psi}^{-*}_{-\frac{1}{3}} + \epsilon^{\frac{4}{3}} k^2 \sin\theta |A|^2 \tilde{\Psi}^{-*}_{\frac{1}{3}}, \tag{69}$$

where

$$\eta = -\frac{r_2 c_1 c_3 k^2 - (\frac{1}{2} c_1^2 c_3^2 k^4 + R_0 c_1 \bar{q}^{(1)}_{1,\tilde{2}} + R_0 c_2 \bar{q}^{(2)}_{1,\tilde{2}} + c_3 \bar{q}^{(3)}_{1,\tilde{2}})}{R_0 {P_r}^{-1} c_1^2 k^2 {k_p}^2 - R_0 {P_r}^{-1} c_2^2 k^2 + c_3^2} \tag{70}$$

identifies with the expression given in eq. (54). The coefficient ξ is given by eq. (55).

Combining the solvability conditions (61), (64), (66) and (69), we are led to express the growth rate

$$\sigma_{inner} \ = \ \epsilon^{\frac{4}{3}} \sigma_{\frac{4}{3}} + \epsilon^{\frac{5}{3}} \sigma_{\frac{5}{3}} + \epsilon^2 \sigma_2, \tag{71}$$

in terms of the “mean flow”

$$\Psi \ = \ \epsilon^{-\frac{1}{3}} \tilde{\Psi}^*_{-\frac{1}{3}} + \tilde{\Psi}^*_0 + \epsilon^{\frac{1}{3}} \tilde{\Psi}^*_{\frac{1}{3}}, \tag{72}$$

in the form

$$\sigma_{inner} = \epsilon k^2 \sin\theta |A|^2 (1 + 2\xi \sin\frac{\theta}{2}) \Psi - \epsilon^2 \eta |A|^2, \tag{73}$$

where subdominant corrections have been neglected.

In order to estimate the mean flow Ψ, we push the ϵ-expansion of eq. (4) at higher orders, where the beating of the perturbation with the basic solution produces contributions of the form $e^{i(\vec{k}_1-\vec{k}_2).\vec{x}}$ which become space-independent and thus resonant in the small θ limit. Consequently, uniform boundedness of the solutions requires, in addition to the usual solvability conditions, the prescription of "quasi-solvability conditions" aimed to eliminate terms which are strictly resonant only for $\theta = 0$. This approach is similar to that used by Ablowitz and Benney [11] when dealing with the small-amplitude divergence of the Whitham modulation analysis for nonlinear dispersive waves (see also [12]). These authors modify the (algebraic) dispersion relation by means of additional corrective terms determined by a constraint which becomes an actual solvability condition in the small amplitude limit, thus transforming the algebraic dispersion relation arising in Whitham's theory, into a partial differential equation for the wave amplitude. In the context of rotating convection, we include contributions $\tilde{Y}_n$ proportional to $e^{i(\vec{k}_1-\vec{k}_2).\vec{x}}$ in the perturbation expansion, which are determined by cancelling them with the terms displaying the same functional dependence and originating from the beating of the basic rolls with quasi-parallel perturbations. Like in the small-amplitude limit of nonlinear waves, this condition becomes an actual solvability in the limit $\theta \to 0$. In both instances, the singularity is prevented by removing slaving conditions: that of the amplitude with respect to the phase in the case of waves, or that of the mean flow with respect to the convective modes in the present problem (compare eqs. (32) and (80) below).

- At order $\epsilon^{\frac{7}{3}}$,

$$\begin{aligned}
&\epsilon^{\frac{7}{3}} L\tilde{X}_{\frac{7}{3}} + \begin{pmatrix} \epsilon\delta_h^- \tilde{\Theta}_2^- AB^* e^{i\vec{k}^-.\vec{x}} \sin 2\pi z \\ \epsilon^{-\frac{1}{3}}\delta_h^{-2}\tilde{\Psi}_{-\frac{1}{3}} AB^* e^{i\vec{k}^-.\vec{x}} + c.c. \\ 0 \end{pmatrix} = \\
&\epsilon^{\frac{7}{3}}[Q_{1,\tilde{\frac{4}{3}}}] + \epsilon \begin{pmatrix} \frac{j_1}{P_r}\delta_h^+\delta_h^-(AB^* e^{i\vec{k}^-.\vec{x}} + ABe^{i\vec{k}^+.\vec{x}}) \sin 2\pi z + c.c. \\ \frac{j_2}{P_r}\delta_h^- AB^* e^{i\vec{k}^-.\vec{x}} + c.c. \\ j_3\delta_h^- ABe^{i\vec{k}^+.\vec{x}} \sin 2\pi z + c.c. \end{pmatrix} + \\
&\begin{pmatrix} 0 \\ \epsilon^{\frac{4}{3}}\sigma^*_{\frac{4}{3}} P_r^{-1}\delta_h^- \epsilon^{-\frac{1}{3}}\tilde{\Psi}_{-\frac{1}{3}} AB^* e^{i\vec{k}^-.\vec{x}} + c.c. \\ 0 \end{pmatrix} + \\
&\epsilon \sin\theta \tilde{\Psi}_0^* e^{i\vec{k_2}.\vec{x}} |A|^2 BZ(-2\frac{k^4}{P_r} c_2\pi \sin\theta \ , \frac{k^4}{P_r} c_1\pi(\sin\frac{\theta}{2} - \sin\frac{3\theta}{2}) \ , 0) + \\
&+\epsilon^{\frac{5}{3}} \sin\theta \tilde{\Psi}^*_{\frac{2}{3}} Ae^{i\vec{k_2}.\vec{x}} Z(-\frac{k^4 k_p^2}{P_r}, \frac{k^4 c_2}{P_r}, -k^2 c_3) + \epsilon^{\frac{7}{3}}\sigma_{\frac{4}{3}} V\tilde{X}_2 + \epsilon^{\frac{7}{3}}\sigma_{\frac{7}{3}} V\tilde{X}_1,
\end{aligned} \tag{74}$$

where $[Q_{1,\tilde{\frac{4}{3}}}]$ denotes the leading order of $Q(X_1, \tilde{X}_{\frac{4}{3}}) + Q(\tilde{X}_{\frac{4}{3}}, X_1)$. Although $\tilde{X}_{\frac{4}{3}}$ contains terms proportional to $e^{\pm i\vec{k}_2.\vec{x}}$, the resulting contributions of the form $e^{i\vec{k}^-.\vec{x}}$ in $Q_{1,\tilde{\frac{4}{3}}}$ are preceded by a factor proportional to $\sin^2\frac{\theta}{2}$ and thus not included in $[Q_{1,\tilde{\frac{4}{3}}}]$. The quasi-solvability condition then reads

$$-\epsilon\sigma_{\frac{4}{3}}P_r^{-1}\delta_h^-\tilde{\Psi}^*_{-\frac{1}{3}}+\epsilon^{-\frac{1}{3}}\delta_h^{-2}\tilde{\Psi}^*_{-\frac{1}{3}}-\epsilon\delta_h^-j_2P_r^{-1}=0. \tag{75}$$

- At order $\epsilon^{\frac{8}{3}}$,

$$\begin{gathered}\epsilon^{\frac{8}{3}}L\tilde{X}_{\frac{8}{3}}+\begin{pmatrix}0\\ -P_r^{-1}\delta_h^-\epsilon^{\frac{4}{3}}\sigma_{\frac{4}{3}}\tilde{\Psi}^*_0+\delta_h^{-2}\tilde{\Psi}^*_0-P_r^{-1}\epsilon^{\frac{4}{3}}\sigma_{\frac{5}{3}}\tilde{\Psi}^*_{-\frac{1}{3}}\\ 0\end{pmatrix}=[Q_{\tilde{\frac{5}{3}},1}]+\\ \begin{pmatrix}0\\ \epsilon^2\frac{8}{P_r}k^4\Psi_0(B\epsilon^{-\frac{1}{3}}\tilde{\Psi}^*_{-\frac{1}{3}}e^{i\vec{k}^+.\vec{x}}+c.c.)\sin\theta\cos^2\frac{\theta}{2}\\ 0\end{pmatrix}+\\ \epsilon^{\frac{4}{3}}\sin\theta\tilde{\Psi}^*_{\frac{1}{3}}e^{i\vec{k_2}.\vec{x}}|A|^2BZ(-2\frac{k^4}{P_r}c_2\pi\sin\theta\ ,\frac{k^4}{P_r}c_1\pi(\sin\frac{\theta}{2}-\sin\frac{3\theta}{2})\ ,0).\end{gathered} \tag{76}$$

The quasi-solvability condition is

$$-P_r^{-1}\epsilon^{-\frac{4}{3}}\sigma_{\frac{4}{3}}\delta_h^-\tilde{\Psi}^*_0+\delta_h^{-2}\tilde{\Psi}^*_0-P_r^{-1}\epsilon^{\frac{5}{3}}\sigma_{\frac{5}{3}}\delta_h^-(\epsilon^{-\frac{1}{3}}\tilde{\Psi}^*_{-\frac{1}{3}})=0 \tag{77}$$

where, as previously, $[Q_{\tilde{\frac{5}{3}},1}]$ does not contribute.

- At order ϵ^3,

$$\begin{aligned}&\epsilon^3L\tilde{X}_4=\epsilon^3[Q_{1,\tilde{3}}+Q_{3,\tilde{1}}+Q_{2,\tilde{2}}]-\epsilon^3R_3G\tilde{X}_1-\epsilon^3R_2G\tilde{X}_2+\epsilon^3(\sigma_2V\tilde{X}_2+\sigma_3V\tilde{X}_1)\\ &-(0\ ,\epsilon^{\frac{1}{3}}\delta_h^{-2}\tilde{\Psi}^*_{\frac{1}{3}}AB^*e^{-i\vec{k}^-.\vec{x}}+c.c.\ ,0)^t\\ &+(0\ ,P_r^{-1}\delta_h^-\epsilon^{\frac{5}{3}}(\sigma_2\tilde{\Psi}^*_{-\frac{1}{3}}+\sigma_{\frac{4}{3}}\tilde{\Psi}^*_{\frac{1}{3}}+\sigma_{\frac{5}{3}}\tilde{\Psi}^*_0)AB^*e^{-i\vec{k}^-.\vec{x}}+c.c.\ ,0)^t,\end{aligned} \tag{78}$$

with the quasi-solvability condition

$$\delta_h^{-2}(\epsilon^{\frac{1}{3}}\tilde{\Psi}_{\frac{1}{3}}^{-*})-P_r^{-1}\epsilon^2\sigma_2\delta_h^-(\epsilon^{-\frac{1}{3}}\tilde{\Psi}^*_{-\frac{1}{3}})-P_r^{-1}\epsilon^{\frac{4}{3}}\sigma_{\frac{4}{3}}\delta_h^-(\epsilon^{\frac{1}{3}}\tilde{\Psi}^*_{\frac{1}{3}})-P_r^{-1}\epsilon^{\frac{5}{3}}\sigma_{\frac{5}{3}}\delta_h^-\tilde{\Psi}^*_0=0. \tag{79}$$

Combining eqs. (75), (77) and (79), we get, up to subdominant contributions,

$$-P_r^{-1}\sigma_{inner}\Psi+\delta_h^-\Psi=\epsilon P_r^{-1}j_2 \tag{80}$$

which together with eq. (73), constitute a closed system. Solving the resulting quadratic equation for the growth rate, we obtain two solutions

$$\begin{gathered}\sigma^{\pm}_{inner}=\frac{1}{2}(-\epsilon^2\eta|A|^2-4k^2P_r\sin^2\frac{\theta}{2})\pm\\ \frac{1}{2}\left[(\epsilon^2\eta|A|^2-4k^2P_r\sin^2\frac{\theta}{2})^2-4\epsilon^2k^2\sin\theta|A|^2j_2(1+2\sin\frac{\theta}{2}\xi)\right]^{\frac{1}{2}}.\end{gathered} \tag{81}$$

where η, ξ and j_2 are defined by eqs. (54), (55) and (29). This expression covers several regimes

(i) For $\theta \sim \epsilon^{\frac{2}{3}}$,

$$\sigma^{\pm}_{inner} \sim \frac{1}{2}(-4k^2 P_r \sin^2\frac{\theta}{2}) \pm \frac{1}{2}\left[(4k^2 P_r \sin^2\frac{\theta}{2})^2 - 4\epsilon^2 k^2 \sin\theta |A|^2 j_2\right]^{\frac{1}{2}} . \tag{82}$$

In this range, $\sigma^{+}_{inner} > 0$ for $\theta > 0$ ($\theta < 0$) if $\tau > 0$ (resp. $\tau < 0$) for any finite value of the Prandtl number (still assuming $P_r > 0.6766$) and of the Taylor number.

(ii) When $\theta \gg \epsilon^{\frac{2}{3}}$,

$$\sigma^{+}_{inner} \sim \sigma_{match} = [-\eta + \frac{\tau\pi^2 k^2}{2k_p^2 P_r}(2\xi + \frac{1}{\sin\frac{\theta}{2}})]\epsilon^2 |A|^2, \tag{83}$$

and matches the limit of σ_{outer} as $\theta \to 0$. Similarly,

$$\sigma^{-}_{inner} \sim -4k^2 P_r \sin^2\frac{\theta}{2} \tag{84}$$

is negative and becomes of order unity outside the boundary layer.

(iii) For $\theta \sim \epsilon^2$,

$$\sigma^{\pm}_{inner} \sim \frac{1}{2}(-\epsilon^2\eta|A|^2) \pm \frac{1}{2}\left[(\epsilon^2\eta|A|^2)^2 - 4\epsilon^2 k^2 \sin\theta |A|^2 j_2\right]^{\frac{1}{2}} , \tag{85}$$

and for $\theta = 0$, σ^{+}_{inner} vanishes, while $\sigma^{-}_{inner}(0) = -\epsilon^2\eta|A|^2$.

We thus obtain a uniform representation for $\theta \in]-\frac{\pi}{2}, \frac{\pi}{2}]$, of the instability growth rate near the convection threshold, of the form

$$\sigma^{+} \quad = \quad \sigma^{+}_{inner} + \sigma_{outer} - \sigma_{match} , \tag{86}$$

where the various terms arising in the right-hand-side of eq. (86) are given by eq. (51), (81) and (83). The influence of various parameters like the Prandtl number and the rotation rate on the strength of the instability, is illustrated in the following figures.

Figure 1 shows the variation of the eigenvalues $\sigma^{\pm}$ with the angle θ of the perturbation for $P_r = 2$, $\epsilon = 0.1$ and $\tau = 10$. For anti-clockwise rotation and finite Prandtl number, the growth rate σ^{+} is positive for small enough positive angles θ. There is also a range of negative angles, where there are two complex conjugate eigenvalues, with negative real parts. The dashed line represents the outer solution σ_{outer} which diverges in the limit $\theta \to 0$. The other eigenvalue σ^{-} which, as $\epsilon \to 0$, becomes marginal in a neighborhood of $\theta = 0$, is of order unity outside the angular boundary layer. It thus cannot be computed perturbatively for θ of order unity but, being always negative or complex with a negative real part, it cannot lead to an instability.

Figure 2 displays the growth rate σ^+ for $\tau = 38$, $\epsilon = 0.1$ and various values of the Prandtl number for positive angles. We observe that both the range of unstable angles and the maximal growth rate decrease when the Prandtl number is increased. At $P_r = 10$, the small angle instability and the Küppers-Lortz instability (around $\theta = 50^o$) can be separated, in contrast with the case of smaller Prandtl numbers (e.g. $P_r = 5$) where all the angles $0 < \theta \leq 64^o$ are unstable. For this rotation rate, only the small angle instability survives at Prandtl number $P_r = 15$. It becomes hardly visible at $P_r = 50$. Indeed, as the Prandtl number goes to infinity, the negative eigenvalue σ^- has a limit, while the outer expansion σ^+_{outer} extends towards $\theta = 0$ where it asymptotically reaches the value $\sigma^-(0)$, the inner range reducing to the vertical axis.

Figure 3 shows the variation of the instability growth rate with the rotation rate τ, for $P_r = 15$ and $\epsilon = 0.1$. For $\tau = 10$, only the small angle instability is present. The Küppers-Lortz instability (again localized around $\theta = 58^o$) arises for $\tau \approx 40$ and is strongly amplified as τ is increased.

Figure 4a displays for $\epsilon = 0.1$, the critical value of the rotation rate τ for the onset of the Küppers-Lortz instability, as a function of the Prandtl number, as long as the latter is large enough for the two instabilities to be separated. Figure 1b shows the most unstable angle (in degrees) for the Küppers-Lortz instability, versus the Prandtl number, for a rotation rate corresponding to the onset of the instability.

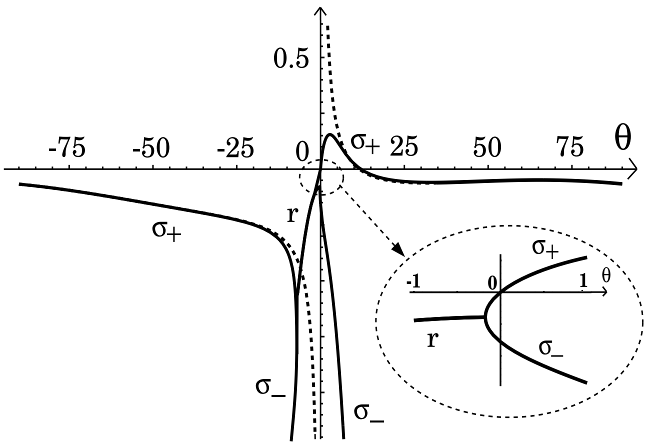

Figure 1: Instability growth rates σ^+ and σ^- or their real part r when complex conjugate (full line), together with the diverging "outer solution" (dashed line), versus the perturbation angle θ (in degrees), for $P = 10$, $\tau = 10$ and $\epsilon = 0.1$.

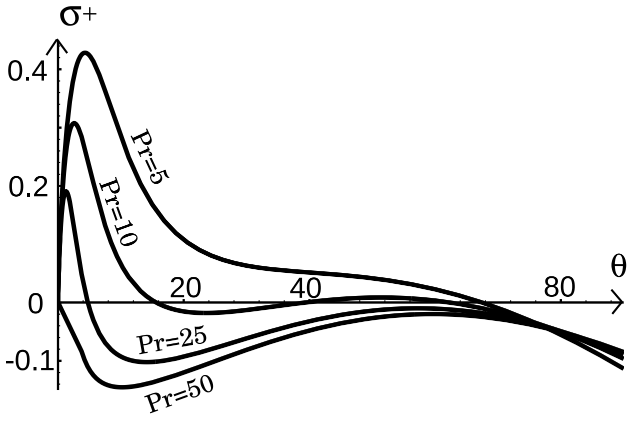

Figure 2: Growth rate σ^+, versus the perturbation angle $\theta > 0$, for $\tau = 38$, $\epsilon = 0.1$ and different values $P_r = 5, 10, 25, 50$ of the Prandtl number.

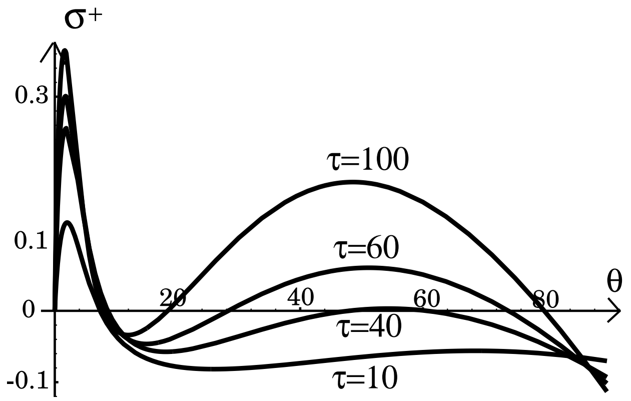

Figure 3: Growth rate σ^+, versus the perturbation angle $\theta > 0$, for $P = 15$, $\epsilon = 0.1$ and different values $\tau = 10$, 40, 60, 100 of the rotation rate τ.

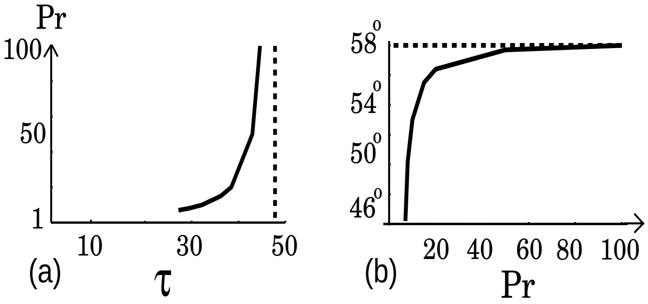

Figure 4: Küppers-Lortz instability boundary in the (P_r, τ)-plane (a), and angle associated to the unstable perturbation at the critical Taylor number versus the Prandtl number (b).

5 Nature of the instability and nonlinear developments

We showed in Section 4 that in a rotating horizontal fluid layer with moderate Prandtl number, limited by top and bottom free-slip boundaries, convective rolls are linearly unstable with respect to perturbations in the form of rolls making a small angle with that of the basic pattern. This instability occurs even when the rotation rate is too low for the existence of the Küppers-Lortz instability. It is related to the divergence of the growth rate (52) which, at finite Prandtl number, occurs when the direction of the wavevector of the perturbation, approaches that of the basic rolls. We here chosed the associated wavenumbers to be critical, but the effect survives whatever their values.

The above instability was obtained in an infinite domain. Its persistence with lateral boundaries requires the presence of a large number of rolls, and thus a convective cell with a large aspect ratio μ^{-1}. The mesh size in Fourier space scaling like μ, the minimum angle θ between two wavevectors, behaves like $\mu^{1/2}$. Since for the small-angle instability $\sigma \sim \epsilon^{4/3}$ and $\theta \sim \epsilon^{2/3}$, it follows that $\sigma \sim \mu$, a growth rate intermediate between that (of order unity) of a pure amplitude instability and a phase instability, for which σ scales like μ^2.

As shown in [13] and [14], in the absence of rotation, parallel rolls may also be unstable (for wavenumbers larger than critical) to a skewed-varicose instability whose growth rate also varies like the inverse aspect ratio μ, a scaling resulting from the strong magnitude of the mean flow in the case of free-slip boundary conditions. This instability is however not captured by the present formalism since the roll distortions involved in this instability cannot be represented within the class of perturbations (superposition of two families of straight rolls) we have considered.

In order to investigate the relation between the small-angle and the skewed-varicose instabilities, and to analyze their nonlinear developments, a system of equations in the spirit of the Swift-Hohenberg equation, but coupling the leading vertical mode to the mean flow, was derived by a perturbation expansion near threshold [15]. This system which preserves the rotational invariance of the problem, generalizes equations obtained by Manneville [16] at finite Prandtl number in the absence of rotation. In a simplified version where the non-local couplings are suppressed and only a few representative nonlinear terms are retained, it is also consistent with models used in [17] and [18] for rotating convection at infinite Prandtl number. A similar model was considered in [19].

As discussed in [15], the phase equation derived in the context of the generalized Swift Hohenberg equations, shows that the skewed varicose instability occurring without rotation near onset, becomes asymmetric with respect to the angle of the phase perturbation, in the presence of rotation. This model also shows that both the asymmetric skewed varicose and the small angle instabilities lead, by means of reconnection, to a progressive rotation of the convective rolls in the direction of the external rotation, an effect due to the mean flow which develops shear layers.

We are thus, led to conclude that the small-angle divergence of the Küppers-Lortz instability growth rate pointed out in [9], results from the presence of a small-angle instability, which can be identified as an asymmetric skewed-varicose instability. In contrast with the (symmetric) skewed varicose instability arising without rotation, the asymetric one developing in presence of rotation exists whatever value of the basic roll wavenumber. Both instabilities are produced by the mean flow and deaseapear in the limit of infinite

Prandtl numbers.

Acknowlegments:

We are grateful to F.Busse for suggesting the relation with the skewed varicose instability and to the anonymous referee for pointing out reference.[19] to our attention.

[1] G. Küppers and D. Lortz "Transition from laminar convection to thermal turbulence in a rotating fluid layer", J. Fluid Mech. **35**, 609 (1969).

[2] R.M. Clever and F.H. Busse, "Nonlinear properties of convection rolls in a horizontal layer rotating about a vertical axis", J. Fluid Mech. **94**, 609 (1979).

[3] M.C. Cross and P.C. Hohenberg, "Spatio-temporal chaos", Science **263**, 1569 (1994).

[4] L.Ning and R.E. Ecke, "Küppers-Lortz transition at high dimensionless rotation rates in rotating Rayleigh-Bénard convection", Phys. Rev. E **47**, R2291 (1993).

[5] M.C. Cross, D. Meiron, Y. Tu, "Chaotic domains: a numerical investigation", Chaos **4**, 607 (1994).

[6] Y. Hu, R.E. Ecke, G. Ahlers, "Time and length scales in rotating Rayleigh-Bénard convection", Phys. Rev. Lett. **74**, 5040 (1995).

[7] F.H. Busse and K.E. Heikes, "Convection in a rotating layer: a simple case of turbulence", Science **208**, 173 (1980).

[8] G. Küppers, "The stability of steady finite amplitude convection in a rotating fluid layer", Phys. Lett. **32 A**, 7 (1970).

[9] T. Clune and E. Knobloch, "Pattern selection in rotating convection with experimental boundary conditions", Phys. Rev. E **47**, 2536 (1993).

[10] S. Chandrasekhar, "Hydrodynamic and Hydromagnetic Stability", *Oxford University Press* (1961).

[11] M.J. Ablowitz and D.J. Benney, "The evolution of multi-phase modes for nonlinear dispersive waves", Stud. Appl. Math. **49**, 225 (1970).

[12] A.C. Newell, "Solitons in Mathematics and Physics", CBMS-NSF Regional conference series in Applied Mathematics **48**, SIAM (Philadelphia) (1985).

[13] A. Zippelius and E.D. Siggia "Stability of finite-amplitude convection", Phys. Fluids **26**, 2905 (1983).

[14] F. H. Busse and E. W. Bolton "Instabilities of convection rolls with stress-free boundaries near threshold", J. Fluid Mech. **146**, 115 (1984).

[15] Y. Ponty, T. Passot and P.L . Sulem, "Pattern dynamics in rotating convection at finite Prandtl number", in preparation.

[16] P. Manneville, "A two-dimensional model for three-dimensional convective patterns in wide containers", J.Physique **44**, 759 (1983).

[17] M. Neufeld, R. Friedrich and H Haken, “Order parameter equation for high Prandtl number Rayleigh-Bénard convection in a rotating large aspect ration system”, Z. Phys. **B 92**, 243 (1993).

[18] M. Fantz, R. Friedrich, M. Bestehorn and H. Haken, “Pattern formation in Bénard convection”, Physica D **61**, 147 (1992).

[19] H. Xi, J. D. Gunton and G. A. Markish “Pattern formation in a rotating fluid: Küppers-Lortz instability”, Physica A **204**, 741 (1994).

Chapitre C

Convection avec rotation dans un système étendu.

La dynamique des textures produites par la convection avec rotation est un bon exemple de transition vers un chaos spatio-temporel. En effet, les textures sont déstabilisées par l'instabilité de Küppers-Lortz dès que le nombre de Rayleigh est supérieur au Rayleigh critique [2]. Cette instabilité, présente au dessus d'une rotation critique, a surtout été étudiée dans le cas de nombre de Prandtl infini. Le modèle à trois modes de Busse-Heikes [24] présente la dynamique non linéaire comme un changement des modes convectifs, changeant d'orientation par des bonds successifs d'angle de 60^o. Cette dynamique est retrouvée avec des modèles traitant les textures de manière isotropes. Ces modèles sont une extension au cas avec rotation du modèle de Swift-Hohenberg [25], [10].

A nombre de Prandtl fini sans rotation, la dynamique des textures est liée à un écoulement moyen qui joue un rôle très important à faible nombre de Prandtl [16]. Près du seuil de convection, ce courant de dérive induit des modifications sur les instabilités à grandes échelles. Un peu plus loin du seuil, cette dynamique conduit à un chaos spatio-temporel avec des textures diverses, comme par exemple la formation de spirales. Des modèles de convection du type de Swift-Hohenberg ont été construits en couplant la dynamique du mode convectif et la fonction de courant de l'écoulement moyen [17]. Avec des conditions aux limites libres ou rigides, ces modèles ont permis de retrouver et d'étudier cette dynamique [20].

A nombre de Prandtl fini et avec rotation, l'écoulement moyen est dynamisé par la force de Coriolis. Avec des conditions aux limites libres, nous avons montré l'existence d'une instabilité d'amplitude à petit angle [6] présente pour des faibles rotations et dominant l'instabilité de Küppers-Lortz à faible nombre de Prandtl. Avec des conditions aux limites rigides, Küppers (1970) [4], Clune et Knobloch (1993) [5] ont montré que l'instabilité de

Küppers-Lortz est sensiblement modifiée à nombre de Prandtl fini. En effet, l'angle le plus instable θ_{KL} diminue fortement à faible nombre de Prandtl ($\theta_{KL} \approx 38$ pour $P = 0.8$). Dans leurs expériences avec rotation à faible nombre de Prandtl, Hu et al. [31] ont montré que la longueur de corrélation des domaines de rouleaux ayant la même orientation, évolue en ϵ^a, où a est un exposant qui dépend de la rotation. Ce résultat est contraire aux prédictions théoriques de Cross et al. [25] en $\epsilon^{-\frac{1}{2}}$, obtenues par une extension du modèle à trois modes et confirmées avec des simulations sur un modèle restreint aux nombres de Prandtl infinis.

Dans ce contexte, le modèle à trois modes de Busse-Heikes et les modèles de convection du type de Swift-Hohenberg avec rotation ne faisant pas intervenir l'écoulement moyen, ne sont plus suffisants pour décrire la dynamique.

Cela nous a conduit à nous intéresser à l'élaboration de modèles de convection avec rotation à nombre de Prandtl fini, avec des conditions aux limites libres afin d'explorer la dynamique engendrées par l'instabilité à petit angle. Nous nous sommes également intéressés au cas avec des conditions aux limites rigides plus adaptées aux expériences.

1 Modèle de convection à nombre de Prandtl fini

Pour des conditions aux limites libres, nous avons dérivé un modèle de convection près du seuil à partir des équations de Boussinesq, projetant la dynamique tridimensionnelle des écoulements convectifs en un modèle bidimensionnel produisant une dynamique de texture. L'écart au nombre de Rayleigh critique est le paramètre de développement. Les composantes verticales de l'écart à la température moyenne, du potentiel irrotationnel et de la fonction courant rotationnelle de la vitesse sont développées sur une base de Galerkin. En supposant que les textures sont une superposition de rouleaux légèrement modulés ayant un nombre d'onde proche du nombre d'onde critique, il est possible de développer les opérateurs horizontaux comme une modulation à grande échelle autour du nombre d'onde critique. Les textures sont ainsi traitées de manière isotrope. Cette approche a été utilisée par Manneville (1983) [17] pour dériver un modèle de convection à nombre de Prandtl fini sans rotation.

En développant sur les deux premiers modes de Galerkin et en prenant une échelle temporelle proportionnelle à l'écart au nombre de Rayleigh critique, nous trouvons un système d'équations fermées (voir l'Appendice), où le mode convectif est couplé avec la fonction de courant du champ moyen [17], mais dépend aussi des termes du deuxième harmonique. L'importance de garder la dépendance des termes du deuxième harmonique a été soulevée par Roberts (1992) [18].

Une première étape a consisté à étudier la stabilité linéaire de rouleaux perturbés. Etant donnée la complexité du système d'équations, un logiciel de calcul formel a été utilisé pour développer les termes non linéaires. Cette analyse a permis de retrouver le taux de rotation critique et l'angle critique de l'instabilité de Küppers-Lortz calculés sur les équations primitives de Boussinesq à nombre de Prandtl infini [2] et à nombre de Prandtl fini [6] (voir Figure 1 et Chapitre B).

L'étape suivante consiste à simplifier ce modèle, tout en conservant les propriétés de stabilité linéaire relatives à l'instabilité de Küppers-Lortz.

En localisant et en simplifiant les opérateurs agissant sur les termes du second harmonique, on obtient un modèle formé de l'équation du mode convectif couplée à l'équation du champ moyen. Dans ce cas, le calcul de stabilité des rouleaux droits a montré que la localisation des termes du second harmonique ne permet pas de retrouver exactement le taux de croissance calculé sur les équations primitives.

Dans le but de construire un modèle plus simple, nous avons été amené à choisir et à simplifier les termes non linéaires pour le mode convectif dominant, en gardant intégralement l'équation de la vorticité verticale du modèle complet. Les termes ont été choisis de manière à préserver les propriétés linéaires du modèle complet, afin de retrouver le profil du taux de croissance de la perturbation des rouleaux droits (Figure 3).

Nous avons aussi construit un modèle de convection avec des conditions aux limites rigides. Le mode convectif est projeté sur une fonction obéissant aux contraintes des conditions aux limites rigides [13]. La fonction de courant du champ moyen dépend désormais de la composante verticale avec un profil en $\sin(\pi z)$ qui est une bonne approximation d'un écoulement de Poiseuille. L'équation de la vorticité verticale est donc reconstruite. On obtient un terme linéaire supplémentaire qui modélise les frottements de l'écoulement moyen sur les limites supérieures et inférieures de la couche de fluide [17]. Les termes non linéaires de l'équation de la vorticité verticale du modèle aux conditions aux limites libres sont présents avec, en plus, un terme nouveau proportionnel à la rotation.

Les coefficients des termes non linéaires du mode convectif sont calculés de manière à obtenir les valeurs critiques de la rotation et de l'angle de l'instabilité de Küppers-Lortz [5]. Le coefficient du terme couplant la vitesse verticale et la fonction courant de l'écoulement moyen est pris proportionnel au temps de relaxation τ_0. Il est ajusté pour obtenir la localisation, en nombre de Rayleigh et en nombre d'onde, l'instabilité zig-zag dans le cas sans rotation.

2 Relation entre l'instabilité d'amplitude à petit angle et l'instabilité de phase varicose oblique.

Le chapitre B a montré l'existence d'une instabilité d'amplitude à petit angle de perturbation et les simulations sur le modèle simplifié montrent que la dynamique faiblement non linéaire a toutes les caractéristiques d'une modulation de phase (Figure B.i).

L'analyse de la modulation de phase sur le modèle sans rotation a permis de retrouver la présence de l'instabilité varicose oblique pour des rouleaux ayant un nombre d'onde supérieur au nombre d'onde critique, (Siggia et Zippelius (1983) [16] et Busse et Bolton (1984) [15]).

Cette analyse a montré que cette instabilité se transforme avec la rotation en une instabilité varicose oblique asymétrique (Figure 5a et 5b). Le taux de croissance des perturbations de grandes longueurs d'ondes devient toujours instable, mais dans un domaine angulaire de signes différents de chaque côté du nombre d'onde critique.

En reliant l'angle de la perturbation de l'instabilité à petit angle au rapport d'aspect, on remarque que le taux de croissance de l'instabilité varicose oblique asymétrique est du même ordre que le taux de l'instabilité à petit angle dans la couche limite angulaire.

Dans l'espace physique, ces deux instabilités produisent une distorsion des rouleaux, qui est associée à de larges bandes d'étirement du champ moyen. Cette compression et dilatation, conduisent à une reconnection des rouleaux, et engendrent une rotation globale.

Dans le formalisme d'amplitude, le mode de perturbation est un mode de Fourier qui est instable, son vecteur d'onde associé forme un angle avec le vecteur d'onde des rouleaux de base dans le même sens que la rotation. Dans un formalisme de phase, le mode de perturbation prend en fait la forme d'un couple de modes séparés d'une distance inversement proportionnelle au rapport d'aspect. Ces modes forment un angle qui change de signe lorsque le nombre d'onde critique est franchi.

Une perturbation prise initialement du type varicose oblique présentant un angle positif (ou négatif) et un nombre d'onde supérieur (ou respectivement inférieur) au nombre d'onde critique peut évoluer de deux manières différentes. Pour une rotation fixée, si le rapport d'aspect de la boîte convective est suffisant, les deux modes sont résonnants et conduisent à une rotation globale des rouleaux dans le sens opposé à la rotation. En effet, le mode le plus proche du nombre d'onde critique va être amplifié, et étant donné le changement de signe avec passage du nombre d'onde critique, le mode instable le plus proche de l'anneau critique provoque une rotation globale des rouleaux dans le sens opposé à la rotation (Figure C.ia).

Si le rapport d'aspect n'est pas suffisamment grand, la distance entre les deux modes composant le couple de la perturbation n'est plus assez faible, et conduit à dissocier les modes perturbés en deux perturbations d'amplitudes indépendantes. Ils obéissent désormais au mécanisme d'amplitude de l'instabilité à petit angle et produisent une rotation globale des rouleaux dans le sens de la rotation.

Dans le cas d'une perturbation prise initialement proche ou égale au nombre d'onde critique, la configuration des deux modes est symétrique (Figure C.ib) et le mécanisme d'amplitude va dominer.

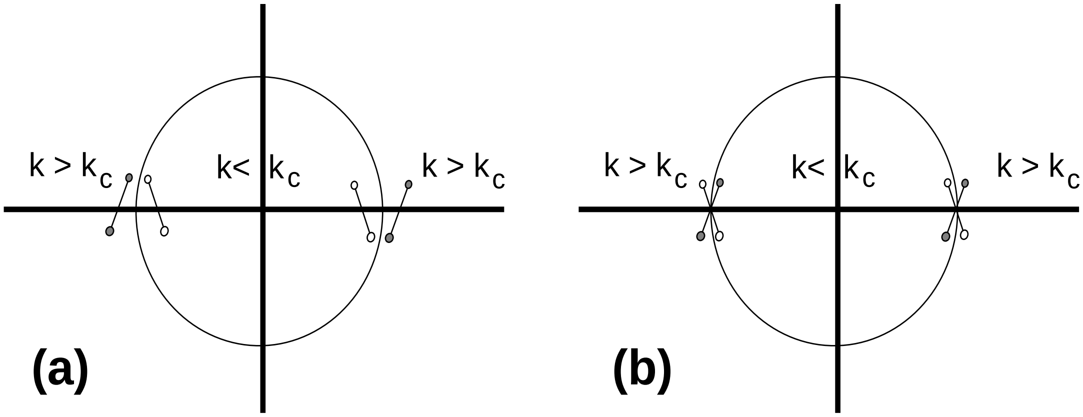

Figure C.i: Représentation des modes instables de l'instabilité varicose oblique asymétrique, dans l'espace spectral de la vitesse verticale. (a) représentation des modes instables pour des nombres d'ondes supérieurs ou inférieurs au nombre d'onde critique, (b) représentation des mêmes modes instables pour des nombres d'ondes proches ou égaux au nombre d'onde critique.

La Figure C.ii montre différents temps d'une simulation sur le modèle simplifié avec des conditions aux limites libres. La condition initiale est prise sous la forme de rouleaux ayant un nombre d'ondes de 0.9 fois la valeur du nombre d'onde critique et perturbée par une pure modulation de phase d'angle inverse à la rotation (Figure C.iia). Comme le prédit le formalisme de phase, les rouleaux tournent globalement dans le sens contraire de la rotation (Figure C.iic), en replaçant le nombre d'onde des rouleaux sur le cercle unité (Figure C.iid). Les rouleaux peuvent désormais être déstabilisés dans le cadre du formalisme en amplitude (Figure C.iif) et tourner dans le sens de la rotation (Figure C.iig).

On peut donc voir l'instabilité varicose oblique asymétrique et l'instabilité à petit angle comme la manifestation d'une même instabilité qui conduit à un mécanisme d'instabilité de phase ou d'amplitude.

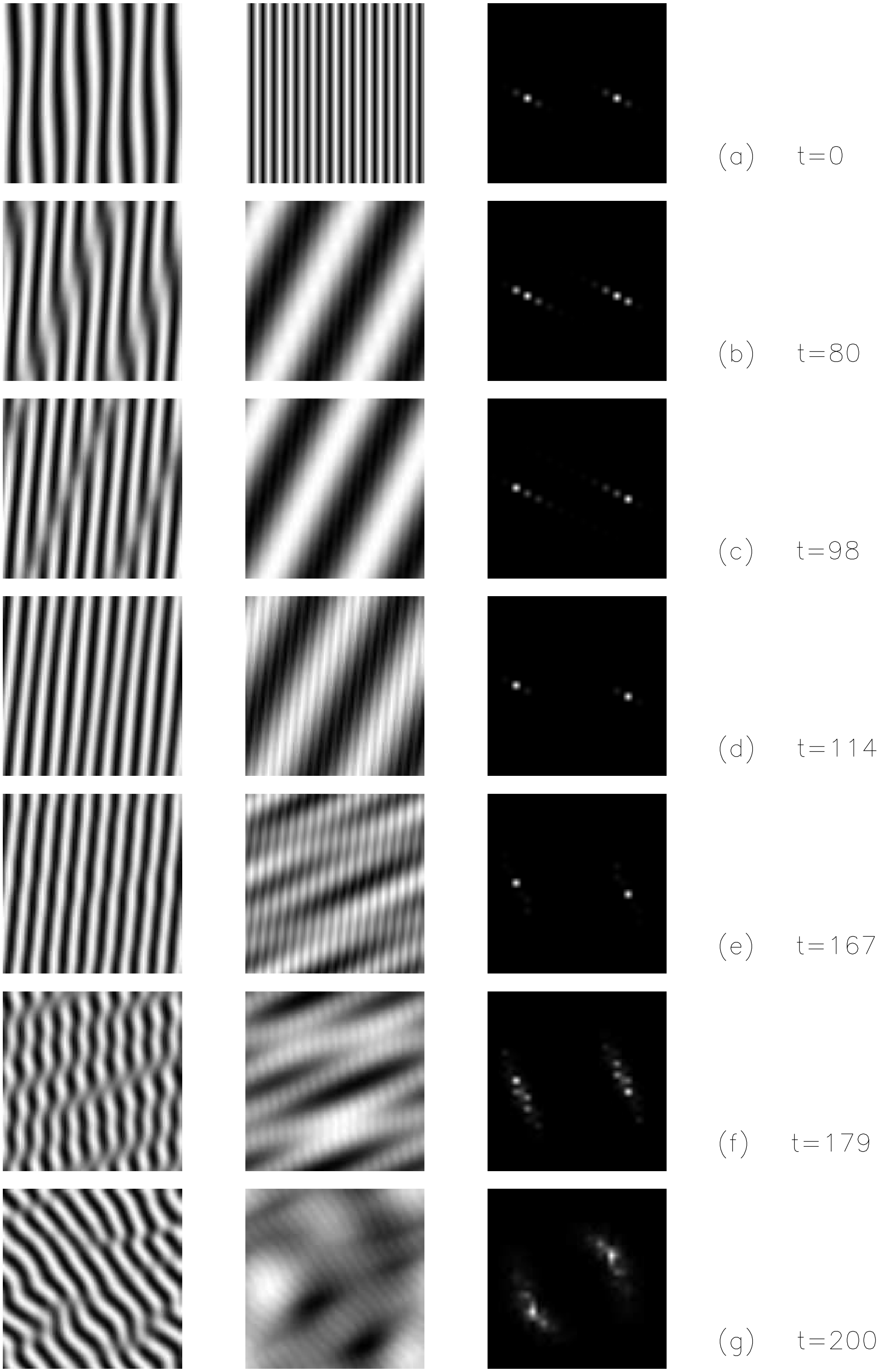

Figure C.ii: Visualisation d'une évolution de rouleaux perturbés initialement par une modulation de phase d'angle négative, avec $k = 0.9\ k_c$, $\tilde{\epsilon} = 0.3$, $\tau = 10$ et un rapport d'aspect $\Gamma = 8$. La colonne de gauche représente le mode convectif, la colonne du milieu la fonction de courant du champ moyen et la colonne de droite le spectre bidimensionnel

3 Dynamique non linéaire du modèle simplifié avec des conditions aux limites libres.

Les simulations du modèle simplifié avec des conditions aux limites libres ont été explorées dans un domaine périodique, en utilisant une méthode pseudo-spectrale pour des résolutions allant de 128^2 à 512^2 points de collocation. Le régime faiblement non linéaire a permis d'explorer et de visualiser les instabilités de phase et l'instabilité d'amplitude à petit angle prévues par la théorie (Figures C.ii et B.i).

Pour des régimes avec ou sans rotation à nombre de Prandtl infini, nous retrouvons la dynamique de texture connue. Sans rotation, à un nombre de Rayleigh suffisant, les structures apparaissent sous forme de labyrinthe (Figure 10). Avec rotation, au dessus de la rotation critique, l'instabilité de Küppers-Lortz est présente, produisant une dynamique chaotique de front de dislocation séparant et déplaçant les zones de rouleaux de même orientation (Figure 12). Dans un régime sans rotation à nombre de Prandtl fini, nous retrouvons une dynamique de défaut produisant des textures sous forme de spirale ou de cible (Figure 11).

A faible nombre de Prandtl et avec une faible rotation, nous avons découvert une dynamique nouvelle. En partant de conditions initiales aléatoires, d'une texture turbulentes, le système va s'organiser progressivement pour former des structures cohérentes sous forme de cible (Figure 13) . Ces structures cohérentes sous l'effet de défauts émanant du centre ou traversant la structure peuvent osciller entre des textures sous forme de cible et de spirale (Figure 14).

Ces structures sont associées à la formation de tourbillons dans l'écoulement moyen. Le système converge vers un état stable (Figure 15b). La formation de telles structures peut être vue comme une augmentation et une concentration du champ moyen dans des tourbillons, organisant les textures sur une géométrie cylindrique. En effet, l'instabilité à petit angle va introduire une symétrie supplémentaire dans le système, l'invariance par rotation.

A grande rotation, de telles structures n'apparaissent pas ou sont déstabilisées très rapidement. En effet, l'instabilité de Küppers-Lortz est présente et empêche la formation de ces structures cohérentes.

La présence de ces structures cohérentes a été confirmée par la simulation du modèle complet (Appendice) (Figure C.iii)

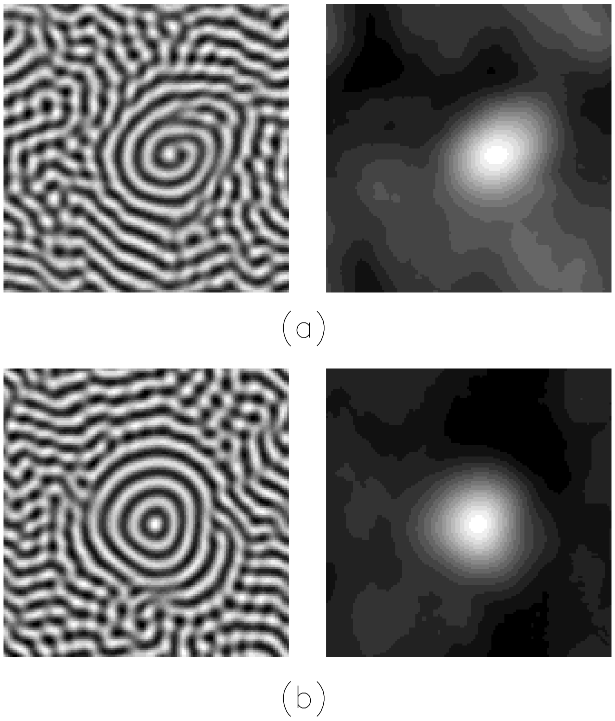

Figure C.iii: Visualisation de l'émergence d'une structure cohérente oscillant entre des structures sous forme de spirale (a) et sous une forme de cible (b). Simulation du modèle complet aux conditions aux limites libres, avec $\epsilon = 0.08$, $\tau = 10$ et un rapport d'aspect $\Gamma = 16$. La colonne de gauche représente le mode convectif, la colonne de droite la fonction de courant du champ moyen.

4 Dynamique non linéaire du modèle avec des conditions aux limites rigides.

Nous avons exploré la dynamique non linéaire du modèle aux conditions aux limites supérieures et inférieures rigides et avec des conditions horizontales périodiques, pour différentes rotations et nombres de Prandtl.

En l'absence de rotation, nous retrouvons les textures sous forme de spirale à faible nombre de Prandtl et de labyrinthe à fort nombre de Prandtl.

En augmentant la rotation, la longueur de corrélation des textures augmente (Figure 17). La Figure 16b montre une augmentation de la taille des structures par rapport aux cas sans rotation (Figure 16a). On peut aussi noter que le sens de rotation de l'écoulement moyen associé aux spirales se conforme au sens de la rotation, la symétrie de chiralité est brisée et le sens de rotation des zones de tourbillon de l'écoulement moyen suit celui de la couche de fluide [37].

Pour des rotations proches de la rotation critique de l'instabilité de Küppers-Lortz, il est possible d'obtenir une structure de rouleaux droits animés de défauts (Figure 16c). En effet, la rotation va activer le déplacement des défauts qui avec un phénomène d'annihilation par paire va produire une texture ayant une plus grande longueur de corrélation. Ce phénomène d'annihilation des défauts a été vu par Millàn-Rodrìgez et al. [8] dans des simulations sur les équations primitives de Boussinesq avec des conditions aux limites horizontales périodiques. .

Dans le cas où l'instabilité de Küppers-Lortz est présente, et lorsque la texture converge vers des rouleaux droits (Figure 16c), il y a création de nouveaux fronts de défauts qui déstabilisent la structure, pour ensuite se restructurer en rouleaux laminarisés par la dynamique des défauts. La Figure 18c illustre cette dynamique, montrant la longueur de corrélation au cours du temps produissant des pics de corrélation.

Pour des rotations plus fortes, l'instabilité de Küppers-Lortz joue un rôle déstabilisant, brisant les grandes structures (Figure 16d). On obtient des longueurs de corrélation beaucoup plus faibles (Figure 17).

Dans des expériences avec rotation, Hu et al. [31] (1995) ont mesuré les longueurs de corrélation. Ils ont montré que la dépendance avec l'écart au Rayleigh critique se comporte avec un exposant qui dépend de la rotation.

Nous avons retrouvé avec nos simulation une augmentation de la longueur de corrélation autour de la rotation critique (Figure 17). Hu et al. (1995) dans [31] ont présenté un graphique qui n'a pas été commenté qui montre la longueur de corrélation augmenter puis diminuer avec la rotation, le maximum se situant autour de la rotation critique.

Ce nouveau phénomène peut être interprété comme la manifestation d'une dynamique de défauts activée par la rotation et qui organise les structures de façon laminaire.

Les expériences de Hu et al. étaient confinées dans une géométrie cylindrique avec des bords horizontaux. Sachant que les effets de bord produisent des défauts, nous avons élaboré un code en géométrie cylindrique avec des bords qui simule le modèle de convection avec des conditions rigides.

Une étude est en cours, cherchant à évaluer s'il existe un équilibre entre l'annihilation par paire des défauts et leur création par les effets de bord. Cette étude a aussi pour objectif d'étudier le comportement de la longueur de corrélation avec l'écart au nombre de Rayleigh critique en fonction de la rotation.

5 Appendice

Modèle complet valide pour des conditions aux limites libres
(Dérivé dans la section 2.a):

$$\tau_0 \partial_t w_1 \quad = \quad (\epsilon - \xi_0 (\Delta_h + q_c^2)^2) w_1 - g \ \mathcal{Q}(w_1, \theta_2, w_2, \phi_2, \psi_2, \psi_0)$$

$$(\partial_t - P\Delta_h)\Delta_h \psi_0 = \frac{\pi^2}{2q_c^4}(1-\beta^2)\mathcal{N} - \frac{\tau\pi^2}{q_p^2 q_c^4}((\Delta_h w_1)^2 + \nabla_h w_1 . \nabla_h \Delta_h w_1) \ .$$

$$\Delta_h \phi_2 = -2\pi w_2$$

$$\mathcal{D} \begin{pmatrix} w_2 \\ \psi_2 \\ \theta_2 \end{pmatrix} = \mathcal{F} \begin{pmatrix} \mathcal{M} \\ \mathcal{N} \\ \mathcal{H} \end{pmatrix}$$

avec

$$\mathcal{D} = \begin{pmatrix} (\Delta_h - 4\pi^2)^2 & -2\pi\tau\Delta_h & \Delta_h \\ 2\pi\tau & -(\Delta_h - 4\pi^2)\Delta_h & 0 \\ Ra_c & 0 & (\Delta_h - 4\pi^2) \end{pmatrix}$$

$$\mathcal{F} = \begin{pmatrix} \frac{\pi {q_p}^2 \Delta_h}{2P{q_c}^4} & \frac{\beta\pi^3}{P{q_c}^4} & \frac{2\beta^2\pi^3}{P{q_c}^4} \\ -\frac{\beta\pi^2\Delta_h}{2P{q_c}^4} & \frac{(1-\beta^2)\pi^2}{2P{q_c}^4} & \frac{2\beta\pi^2}{P{q_c}^4} \\ \frac{3\pi}{2}\frac{{q_p}^2}{{q_c}^2} & 0 & 0 \end{pmatrix}$$

où

$$\begin{aligned} \mathcal{M} &= (\nabla_h w_1)^2 + q_c^2 w_1^2 \\ \mathcal{N} &= (\nabla_h(\Delta_h w_1) \times \nabla_h w_1).\mathbf{e}_z \\ \mathcal{H} &= (\partial_{xx} w_1 \partial_{yy} w_1 - (\partial_{xy} w_1)^2) \ . \end{aligned}$$

et

$$g = \frac{1}{q_c^2 R_c} \ , \ \xi_0 = \frac{1}{q_c^2 q_p^2} \ , \ \tau_0 = \frac{1}{q_p^2}(1 + \frac{1}{P}(1 - \frac{2\tau^2\pi^2}{R_c q_c^2})) \ .$$

avec $\mathcal{Q}(w_1, \theta_2, w_2, \phi_2, \psi_2, \psi_0) =$

$$
\begin{array}{l}
(P^{-1}(\Delta_h - \pi^2)(1 + \tfrac{\pi^2}{q_c^2}) - 3{q_p}^2)\Delta_h(\nabla_h w_1 \ \times \ \nabla_h \psi_0)\hat{z} + \\
(-P^{-1}(\Delta_h - \pi^2) \ \tfrac{\pi^2}{{q_c}^2}) \ (\nabla_h w_1 \ \times \ \nabla_h \Delta_h \psi_0)\hat{z} + \\
(P^{-1}(\Delta_h - \pi^2) \ \tfrac{2\pi^2}{{q_c}^2} \ \beta)(2 \ \partial_{xy}\psi_0 \ \partial_{xy} w_1 - \partial_{xx}\psi_0 \ \partial_{yy} w_1 - \partial_{yy}\psi_0 \ \partial_{xx} w_1) + \\
(\tfrac{\tau\pi^2}{P \ {q_c}^2}) \ (2 \ \Delta_h w_1 \ \Delta_h \psi_0 + \nabla_h w_1 \ \nabla_h \Delta_h \psi_0 + \nabla_h \psi_0 \ \nabla_h \Delta_h w_1 + {q_c}^2 \ (w_1 \ \Delta_h \psi_0 + \nabla_h w_1 \ \nabla_h \psi_0)) + \\
(-\beta \tfrac{\tau\pi^2}{P \ {q_c}^2}) \ (\nabla_h w_1 \ \times \ \nabla_h \Delta_h \psi_0 + \nabla_h \psi_0 \ \times \ \nabla_h \Delta_h w_1)\hat{z} + \\
(-\tfrac{\pi}{2 \ {q_c}^2}\Delta_h) \ (\nabla_h w_1 \ \nabla_h \theta_2 - 2 \ {q_c}^2 \ w_1 \ \theta_2)\hat{z} + \\
(-\beta \tfrac{\pi}{2 \ {q_c}^2}\Delta_h) \ (\nabla_h \theta_2 \ \times \ \nabla_h w_1) + \\
((\Delta_h - \pi^2) \ (-\tfrac{\pi^3}{2P{q_c}^2}) - \tfrac{3\beta\tau\pi^3}{2P{q_c}^2}) \ (w_2 \ \Delta_h w_1) + ((2\pi^3 - \tfrac{\pi}{2}\Delta_h)P^{-1}(\Delta_h - \pi^2) - \tfrac{3\pi{q_p}^2}{2}\Delta_h)w_2 \ w_1 + \\
(\beta \tfrac{\pi}{2{q_c}^2} \ P^{-1}(\Delta_h - \pi^2) \ (\Delta_h - 3\pi^2) + \tfrac{\tau\pi^3}{2P{q_c}^2}) \ (\nabla_h w_2 \ \times \ \nabla_h w_1)\hat{z} + \\
((\tfrac{\pi}{2{q_c}^2} \ P^{-1}(\Delta_h - \pi^2) \ (\Delta_h - 3\pi^2)) - \beta \tfrac{\tau\pi^3}{2P{q_c}^2})(\nabla_h w_1 \ \nabla_h w_2) + \\
(-P^{-1}(\Delta_h - \pi^2) \ (\tfrac{3}{2}\pi^2 + \tfrac{1}{2}\Delta_h) + \tfrac{3{q_p}^2}{2}\Delta_h) \ (\nabla_h w_1 \ \nabla_h \phi_2) + \\
(\tfrac{\pi^2}{{q_c}^2}P^{-1}(\Delta_h - \pi^2)) \ (2 \ \partial_{xy}\phi_2 \ \partial_{xy} w_1 + \partial_{xx}\phi_2 \ \partial_{xx} w_1 + \partial_{yy}\phi_2 \ \partial_{yy} w_1) + \\
(\beta \tfrac{\pi^2}{{q_c}^2}P^{-1}(\Delta_h - \pi^2)) \ (\partial_{xy} w_1 \ (\partial_{xx} - \partial_{yy})\phi_2 - \partial_{xy}\phi_2 \ (\partial_{xx} - \partial_{yy})w_1) + \\
(\tfrac{\tau\pi^2}{2P{q_c}^2}) \ [((\nabla_h \phi_2 \ \times \ \nabla_h \Delta_h w_1) + {q_c}^2(\nabla_h w_1 \ \times \ \nabla_h \phi_2))\hat{z} + \beta(\nabla_h \phi_2 \ \nabla_h \Delta_h w_1)] + \\
(-P^{-1}(\Delta_h - \pi^2) \ (\tfrac{3}{2}\pi^2 + \tfrac{1}{2}\Delta_h) + \tfrac{3{q_p}^2}{2}\Delta_h) \ (\nabla_h w_1 \ \times \ \nabla_h \psi_2)\hat{z} + \\
(\tfrac{\pi^2}{{q_c}^2}P^{-1}(\Delta_h - \pi^2)) \ (\partial_{xy}\psi_2 \ (\partial_{xx} - \partial_{yy})w_1 - \partial_{xy} w_1 \ (\partial_{xx} - \partial_{yy})\psi_2) + \\
(\beta \tfrac{\pi^2}{{q_c}^2}P^{-1}(\Delta_h - \pi^2)) \ (2 \ \partial_{xy}\psi_2 \ \partial_{xy} w_1 - \partial_{xx}\psi_2 \ \partial_{yy} w_1 - \partial_{yy}\psi_2 \ \partial_{xx} w_1) + \\
(\tfrac{\tau\pi^2}{2P{q_c}^2}) \ (2 \ \Delta_h \psi_2 \ \Delta_h w_1 + \nabla_h w_1 \ \nabla_h \Delta_h \psi_2 + \nabla_h \psi_2 \ \nabla_h \Delta_h w_1 - {q_c}^2(\nabla_h w_1 \ \nabla_h \psi_2 + w_1 \ \Delta_h \psi_2)) + \\
(-\beta \tfrac{\tau\pi^2}{2P{q_c}^2}) \ (\nabla_h w_1 \ \times \ \nabla_h \Delta_h \psi_2 + \nabla_h \psi_2 \ \times \ \nabla_h \Delta_h w_1)\hat{z}
\end{array}
$$

Pattern dynamics in rotating convection at finite Prandtl number

Y. Ponty, T. Passot and P.L. Sulem,
CNRS UMR 6529,
Observatoire de la Côte d'Azur
B.P. 4229, 06304 Nice cedex 4, France

Phys. Rev. E (sous presse)

Abstract

A Swift-Hohenberg type model is derived for rotating convection in a Boussinesq fluid at moderate Prandtl number, for both free-slip and rigid top and bottom boundary conditions. In the former case, a phase dynamics analysis is used to relate the skewed-varicose instability which can occur in the absence of rotation, and the small-angle instability which develops for arbitrary rotation rate and leads to a continuous rotation of the rolls. Numerical simulations show the ordering effect of a moderate rotation which counterbalances the destructuring effect of the mean flow. In the free-slip case, this effect induces the formation of coherent targets, associated to large vortices of the same sign as the external rotation. In the no-slip case, this leads to a maximum correlation of the patterns for a rotation rate of the order of the critical value for the onset of the Küppers-Lortz instability.

PACS numbers: 47.27.Te, 47.20.Lz, 47.52.+j, 47.54.+r

1 Introduction

In addition to its relevance in the context of astrophysical and geophysical fluid dynamics, rotating convection provides a prototype to study the transition to spatio-temporal chaos [1]. The reason is that, close to onset, a chaotic dynamics can result from the destabilization of the basic patterns through the Küppers-Lortz (KL) instability [2]-[5]. It turns out that at finite Prandtl number, special dynamical features can appear. With free-slip boundaries, due to the presence of an intense mean flow, straight parallel rolls have been shown to be linearly unstable relative to a small-angle instability for any value of the rotation rate [6]. With rigid boundaries, experiments in cylindrical boxes have also revealed that the KL instability can arise below the critical rotation, a phenomenon attributed to the influence of sidewall defects [7], [8]. A recent thorough experimental study of convective patterns with moderate rotation [9] demonstrates the richness of the system and points out a number of still unresolved questions that deserve theoretical and numerical investigation.

Several models in the spirit of the Swift-Hohenberg equation have been built in the limit of infinite Prandtl number [10] -[12]. In this regime, the main observation is that when the Taylor number T_a exceeds the critical value for the Küppers-Lortz instability, the destabilization of straight parallel rolls (which arises as soon as the Rayleigh number R exceeds the convection threshold R_c), leads to the formation of patches of straight rolls penetrating each other in a chaotic way: rolls disappear and are replaced by other rolls tilted by an angle close to 60 degrees.

The aim of the present paper is to address the problem of rotating convection at moderate Prandtl number, taken larger than the critical value (0.677 in the case of free-slip boundary conditions) above which over-stability is not possible and the convective instability leads near onset to the formation of steady straight parallel rolls [13]. In Section 2, a model is derived in the context of both rigid and free-slip top and bottom boundary conditions whose strong influence on the mean flow significantly affects the dynamics. In the horizontal directions, the flow is assumed periodic. It improves a model given in [14] in the case of rigid boundaries, by the inclusion of additional couplings and by a better prescription of the coefficients, resulting in more accurate values for the KL instability threshold.

The phase dynamics is analyzed in Section 3 where in the case of free-slip boundaries, a particular attention is paid to the relation between the small-angle instability and the skewed varicose instability which can arise in the absence of rotation [15], [16]. In the fully nonlinear regime, a main conclusion concerns the relaminarization which takes place for rotation rates comparable to the critical rotation for the onset of the Küppers-Lortz instability. In the case of free-slip boundaries (Section 4), this effect leads to the formation of coherent targets and vortices. With rigid boundaries (Section 5), dislocations can totally annihilate each other and lead to the stabilization of straight parallel rolls. The last section briefly summarizes the main results.

2 A model for rotating convection

2.1 An asymptotic model near threshold for free-slip boundaries

The Boussinesq equations in a horizontal fluid layer heated from below and rotating around a vertical axis $\hat{\mathbf{z}}$ are written in the non-dimensional form

$$\Delta\mathbf{V} + \hat{\mathbf{z}}\theta - \nabla\Gamma - \tau\hat{\mathbf{z}} \times \mathbf{V} = P^{-1}(\mathbf{V}.\nabla\mathbf{V} + \partial_t\mathbf{V}) \tag{1}$$

$$\nabla.\mathbf{V} = 0 \tag{2}$$

$$\Delta\theta + R\hat{\mathbf{z}}.\mathbf{V} = \mathbf{V}.\nabla\theta + \partial_t\theta, \tag{3}$$

where the vertical diffusion time is taken as time unit. The other parameters are the Rayleigh number R and the square root τ of the Taylor number (twice the Rossby number) which, to be specific, is taken positive.

It is convenient to rewrite the velocity field $\mathbf{V} = (\mathbf{u}, w)$ in terms of a potential ϕ and a stream function ψ, in the form

$$\mathbf{u} = (u, v) = (\nabla_h\phi - \mathbf{e}_z \times \nabla_h\psi) \tag{4}$$

$$\Delta_h\phi = -\partial_z w \tag{5}$$

where the subscript h refers to the horizontal directions. Applying successively the operators curl and curl^2 on eq. (1) and projecting the resulting equations on the vertical axis, we get

$$(\partial_t - P\Delta)\Delta_h\psi = -\tau P\partial_z w + \partial_x(\mathbf{V}\cdot\nabla v) - \partial_y(\mathbf{V}\cdot\nabla u) \tag{6}$$

$$P^{-1}(\partial_t\Delta w + \mathcal{Q}_1) = \Delta^2 w + \Delta_h\theta + \tau\partial_z\Delta_h\psi \tag{7}$$

with

$$\mathcal{Q}_1 = \Delta_h(\mathbf{V}\cdot\nabla w) - \partial_z\left(\partial_x\left(\mathbf{V}\cdot\nabla u\right) + \partial_y\left(\mathbf{V}\cdot\nabla v\right)\right) \ . \tag{8}$$

Applying the operators $(\partial_t - \Delta)$ on eq. (7), Δ_h on eq. (3) and $-\tau P^{-1}\partial_z$ on eq. (6), and summing the resulting equations, we obtain

$$-P^{-1}\partial_{tt}^2\Delta w + (1 + P^{-1})\partial_t\Delta^2 w + \mathcal{Q}_2 \ = \ \Delta^3 w - R\Delta_h w + \tau^2\partial_{zz}w - \tau(1 - P^{-1})\partial_z\partial_t\Delta_h\psi) \tag{9}$$

where

$$\mathcal{Q}_2 = P^{-1}(\Delta - \partial_t)\mathcal{Q}_1 - \Delta_h(\mathbf{V}\cdot\nabla\theta) + \tau P^{-1}\partial_z(\partial_x(\mathbf{V}\cdot\nabla v) - \partial_y(\mathbf{V}\cdot\nabla u)) \ . \tag{10}$$

As already mentioned, we assume that the Prandtl number exceeds the value $P^* \approx 0.677$, required in the case of free-slip boundary conditions for the convective instability to first set in as stationary convection, and define the stress parameter $\epsilon = \frac{R-R_c}{R_c}$ where R_c is the critical Rayleigh number. Denoting by q_c the critical wavenumber, we have [13]

$$R_c = (\tau^2\pi^2 + (\pi^2 + q_c^2)^3)/q_c^2 \ , \tag{11}$$

with q_c given by

$$2q_c^6 + 3\pi^2 q_c^4 = \pi^6 + \pi^2\tau^2 \ . \tag{12}$$

Near threshold, we perform the Galerkin expansion

$$w = w_1 \sin\pi z + w_2 \sin 2\pi z + \cdots \tag{13}$$
$$\phi = \phi_1 \cos\pi z + \phi_2 \cos 2\pi z + \cdots \tag{14}$$
$$\psi = \psi_0 + \psi_1 \cos\pi z + \psi_2 \cos 2\pi z + \cdots \tag{15}$$
$$\theta = \theta_1 \sin\pi z + \theta_2 \sin 2\pi z + \cdots \tag{16}$$

where w_1, ϕ_1, ψ_0, ψ_1 and θ_1 are of order $\epsilon^{\frac{1}{2}}$, while w_2, ϕ_2, ψ_2 and θ_2 are of order ϵ. Furthermore, time derivatives are assumed to be of order ϵ. The horizontal structure is left unspecified, in order to preserve isotropy. We nevertheless assume that the pattern can locally be viewed as a superposition of slowly modulated rolls with critical wavenumber q_c. When acting on a field locally periodic in the horizontal variables, the Laplacian operator Δ_h thus reduces, to leading order, to the multiplication by $-q_c^2$. The horizontal gradient ∇_h is of order one in the direction across the roll and of order $\epsilon^{1/4}$ in the direction along the roll. Since the direction of the structure is not specified, ∇_h must in general be considered of order unity. However, when acting on slowly varying quantities, ∇_h will be of order $\epsilon^{1/4}$ and Δ_h of order $\epsilon^{1/2}$, as used in [17]. We thus write $\Delta_h w_1 = (-q_c^2 + \mathcal{L})w_1$ with $\mathcal{L} = \mathcal{O}(\epsilon^{1/2})$. In this approach which combines an ϵ and a Galerkin expansion in the vertical direction, it turns out that subdominant terms are possibly retained at each order of approximation.

At order $\epsilon^{1/2}$, the linear analysis is recovered. Defining $q_p^2 = q_c^2 + \pi^2$, we have

$$-q_p^6 w_1 + R_c q_c^2 w_1 - \tau^2\pi^2 w_1 = 0 \tag{17}$$
$$q_p^2 q_c^2 \psi_1 = \tau\pi w_1 \tag{18}$$
$$q_p^2 \theta_1 = R_c w_1 \tag{19}$$
$$q_c^2 \phi_1 = \pi w_1 \tag{20}$$

At order ϵ, when projecting on the first Galerkin mode, we have

$$3q_p^4\mathcal{L}w_1 - R_c\mathcal{L}w_1 = 0\ . \tag{21}$$

At order $\epsilon^{3/2}$, using eq. (18), we get from eq. (7),

$$3q_p^2q_c^2(1+\frac{1}{P}(1-\frac{2\tau^2\pi^2}{R_cq_c^2}))\partial_t w_1 = (\epsilon q_c^2R_c - 3q_p^2\mathcal{L}^2)w_1 - \mathcal{Q}. \tag{22}$$

The nonlinear term $\mathcal{Q}$ stands for the $\epsilon^{3/2}$ contribution arising from the quantity $\mathcal{Q}_2$ defined in eq. (10), when projected on $\sin\pi z$. After straightforward algebra, we get

$$\begin{gathered}\mathcal{Q} = P^{-1}(\Delta_h-\pi^2)\Delta_h[(\mathbf{u_0}.\nabla_h w_1)+\tfrac{1}{2}(\mathbf{u_1}.\nabla_h w_2-\mathbf{u_2}.\nabla_h w_1)-\tfrac{\pi}{2}(w_1w_2)]\\ +\pi P^{-1}((\Delta_h-\pi^2)\nabla_h\cdot -\tau\mathbf{e_z}\cdot\nabla_h\times)[(\mathbf{u_1}.\nabla_h\mathbf{u_0}+\mathbf{u_0}.\nabla_h\mathbf{u_1})\\ +\tfrac{1}{2}(\mathbf{u_1}.\nabla_h\mathbf{u_2}+\mathbf{u_2}.\nabla_h\mathbf{u_1})-\tfrac{\pi}{2}(w_2\mathbf{u_1}+2w_1\mathbf{u_2})]\\ -\Delta_h[3q_p^2\mathbf{u_0}.\nabla_h w_1+\tfrac{1}{2}(\mathbf{u_1}\nabla_h\theta_2-3q_p^2\mathbf{u_2}.\nabla_h w_1)-\pi w_1\theta_2+\tfrac{3\pi}{2}q_p^2w_1w_2)]\end{gathered} \tag{23}$$

where, writing $\beta=\frac{\tau}{q_p^2}$, we defined

$$\mathbf{u_0} = \begin{pmatrix}\partial_y\psi_0\\ -\partial_x\psi_0\end{pmatrix} \tag{24}$$

$$\mathbf{u_1} = \frac{\pi}{q_c^2}\begin{pmatrix}\partial_x w_1+\beta\partial_y w_1\\ \partial_y w_1-\beta\partial_x w_1\end{pmatrix} \tag{25}$$

$$\mathbf{u_2} = \begin{pmatrix}\partial_x\phi_2+\partial_y\psi_2\\ \partial_y\phi_2-\partial_x\psi_2\end{pmatrix} \tag{26}$$

and neglected terms involving derivatives of the slowly varying field $\mathbf{u_0}$.

Similarly, the contribution of order ϵ to the projection of eq. (7) on $\sin 2\pi z$ reads

$$(\Delta_h-4\pi^2)^2w_2+\Delta_h\theta_2-2\pi\tau\Delta_h\psi_2 = \frac{q_p^2\pi}{2Pq_c^4}\Delta_h\mathcal{M}+\frac{\pi^3}{Pq_c^4}\beta\mathcal{N}-\frac{2\pi^3}{Pq_c^4}\beta^2\mathcal{H} \tag{27}$$

where

$$\mathcal{M} = (\nabla_h w_1)^2+q_c^2w_1^2 \tag{28}$$

$$\mathcal{N} = (\nabla_h(\Delta_h w_1)\times\nabla_h w_1).\mathbf{e}_z \tag{29}$$

$$\mathcal{H} = (\partial_{xx}w_1\partial_{yy}w_1-(\partial_{xy}w_1)^2)\ . \tag{30}$$

From eqs. (3) and (6), we have at this order

$$(\Delta_h-4\pi^2)\theta_2+R_cw_2 = \tfrac{3\pi}{2}\tfrac{q_p^2}{q_c^2}\mathcal{M} \tag{31}$$

$$(\Delta_h-4\pi^2)\Delta_h\psi_2-2\pi\tau w_2 = \tfrac{\beta\pi^2}{2Pq_c^4}\Delta_h\mathcal{M}-\tfrac{\pi^2}{2Pq_c^4}(1-\beta^2)\mathcal{N}-\tfrac{2\beta\pi^2}{Pq_c^4}\mathcal{H}. \tag{32}$$

Finally, the equation for the mean flow is also derived from eq. (6) in the form

$$(\partial_t - P\Delta_h)\Delta_h\psi_0 = \frac{\pi^2}{2q_c^4}(1-\beta^2)\mathcal{N} - \frac{\beta\pi^2}{q_c^4}((\Delta_h w_1)^2 + \nabla_h w_1 . \nabla_h \Delta_h w_1) \ . \tag{33}$$

Note that the term involving the time derivative is smaller by a factor $\epsilon^{1/2}$ than the other terms. It must nevertheless be kept when dealing with the large-scale, long-time dynamics. This term is in particular necessary for a uniform description of the instability growth rate of straight parallel rolls perturbed by other rolls turned by an arbitrary angle [6]. We finally get the set of equations

$$\tau_0\partial_t w_1 \ = \ (\epsilon - \xi_0(\Delta_h + q_c^2)^2)w_1 - g\ \mathcal{Q} \tag{34}$$

$$(\partial_t - P\Delta_h)\Delta_h\psi_0 = \frac{\pi^2}{2q_c^4}(1-\beta^2)\mathcal{N} - \frac{\tau\pi^2}{q_p^2 q_c^4}((\Delta_h w_1)^2 + \nabla_h w_1 . \nabla_h \Delta_h w_1) \tag{35}$$

$$\Delta_h \phi_2 = -2\pi w_2 \tag{36}$$

$$\mathcal{D}\begin{pmatrix} w_2 \\ \psi_2 \\ \theta_2 \end{pmatrix} = \mathcal{F}\begin{pmatrix} \mathcal{M} \\ \mathcal{N} \\ \mathcal{H} \end{pmatrix} \tag{37}$$

with $\mathcal{Q}$ given by eqs. (23)-(26) and $\mathcal{M}$, $\mathcal{N}$ and $\mathcal{H}$ by eqs. (28)-(30). Furthermore

$$\mathcal{D} = \begin{pmatrix} (\Delta_h - 4\pi^2)^2 & -2\pi\tau\Delta_h & \Delta_h \\ 2\pi\tau & -(\Delta_h - 4\pi^2)\Delta_h & 0 \\ Ra_c & 0 & (\Delta_h - 4\pi^2) \end{pmatrix} \tag{38}$$

$$\mathcal{F} = \begin{pmatrix} \frac{\pi {q_p}^2 \Delta_h}{2P{q_c}^4} & \frac{\beta\pi^3}{P{q_c}^4} & \frac{2\beta^2\pi^3}{P{q_c}^4} \\ -\frac{\beta\pi^2\Delta_h}{2P{q_c}^4} & \frac{(1-\beta^2)\pi^2}{2P{q_c}^4} & \frac{2\beta\pi^2}{P{q_c}^4} \\ \frac{3\pi}{2}\frac{{q_p}^2}{{q_c}^2} & 0 & 0 \end{pmatrix} \ , \tag{39}$$

and we define the parameters

$$g = \frac{1}{q_c^2 R_c} \ , \ \xi_0 = \frac{1}{q_c^2 q_p^2} \ , \ \tau_0 = \frac{1}{q_p^2}(1 + \frac{1}{P}(1 - \frac{2\tau^2\pi^2}{R_c q_c^2})) \ . \tag{40}$$

2.2 Linear stability analysis

In order to validate the model derived in Section 2.1, it is of interest to compare its predictions relatively to the Küppers-Lortz instability, with the results derived from the primitive Boussinesq equations [6].

In the context of eqs. (34)-(35), straight parallel rolls with critical wavenumber $|\vec{k}_1| = q_c$ are given to leading order by $w_1 = ae^{i\vec{k}_1.\vec{x}} + c.c.$ and $\psi_0 = \frac{\tau\pi^2}{8q_p^2 P}a^2 e^{2i\vec{k}_1.\vec{x}} + c.c$, with an amplitude $a = \epsilon^{\frac{1}{2}} \left(\frac{1}{2q_p^2}(1 - \frac{\tau^2\pi^2}{q_c^4 R_c P^2}) \right)^{-\frac{1}{2}}$. We consider an infinitesimal perturbation of this steady solution given to leading order by

$$\begin{aligned} \tilde{w} &= b(t)e^{i\vec{k}_2.\vec{x}} + c.c. && (41) \\ \tilde{\psi} &= h_1(t)e^{i(\vec{k}_1 - \vec{k}_2).\vec{x}} + h_2(t)e^{i(\vec{k}_1 + \vec{k}_2).\vec{x}} + c.c. \ , && (42) \end{aligned}$$

where the wave-vector $\vec{k}_2$ has the same modulus as $\vec{k}_1$ and makes an angle θ with the latter. Introducing the variables $z_1 = ah_1^*$ and $z_2 = a^*h_2$, and neglecting higher order harmonics, we get the linear system

$$\partial_t \begin{bmatrix} b \\ z_1 \\ z_2 \end{bmatrix} = \begin{bmatrix} \epsilon\tilde{G}(\theta) & v_1(\theta) & v_2(\theta) \\ \epsilon p & -4q_c^2 P \sin^2\frac{\theta}{2} & 0 \\ \epsilon p & 0 & -4q_c^2 P\cos^2\frac{\theta}{2} \end{bmatrix} \begin{bmatrix} b \\ z_1 \\ z_2 \end{bmatrix} \qquad (43)$$

where $p = \frac{\tau\pi^2}{q_p^2 q_c^2}|a|^2$. The precise form of the functions $\tilde{G}, v_1$ and v_2 was computed using the Mathematica software for symbolic calculations.

In the limit of infinite Prandtl number, the Küppers-Lortz instability is accurately recovered: when the rotation rate τ exceeds the critical value 47.8, two-dimensional rolls become unstable for perturbations making an angle $\theta_c \approx 58.11^o$ with the basic rolls. More generally, at finite Prandtl number, the growth rate σ obeys

$$\begin{aligned} &-\sigma^3 + (\epsilon\tilde{G}(\theta) - 4Pq_c^2)\sigma^2 + (4\epsilon q_c^2 P\tilde{G}(\theta) - 4P^2q_c^4\sin^2\theta)\sigma + \\ &\epsilon(\tilde{G}(\theta)4P^2q_c^4\sin^2\theta + 4pPq_c^2(v_1(\theta)\cos^2\frac{\theta}{2} + v_2(\theta)\sin^2\frac{\theta}{2}) = 0. \qquad (44) \end{aligned}$$

Figure 1 displays for various values of the Prandtl number, of the rotation rate and of the distance from threshold, the growth rate of the unstable mode as obtained from the above model (solid line) and as derived in [6] from the primitive equations (dashed lines). An excellent agreement is obtained throughout the range of perturbation angles. Note that the present model directly exhibits the “small-angle instability” derived in [6] from the primitive equations using matched asymptotic expansions. The effect on the nonlinear dynamics of this instability which results from the presence of an intense mean flow at small θ and which exists for arbitrary small rotation is discussed in Section 4.

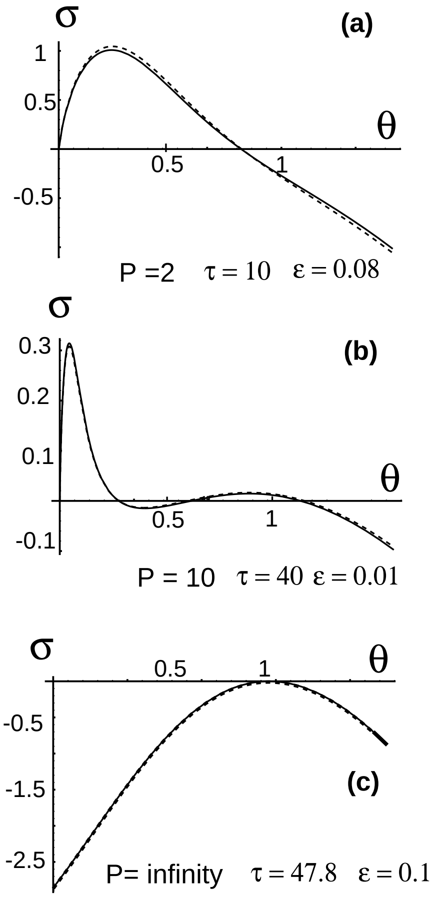

Figure 1: Growth rate of the small-angle and Küppers-Lortz instabilities obtained from the complete model (34)-(40) (dashed line) and from the primitive Boussinesq equations (solid line), for different values of the Prandtl number P, of the Taylor number $T_a = \tau^2$ and of the stress parameter ϵ, in the case of free-slip boundary conditions.

2.3 A simplified model

The model considered in Section 2.2 correctly reproduces the destabilization of convective rolls in rotating convection, but is relatively cumbersome. It is thus desirable to simplify it heuristically, in a way which preserves quantitatively its most prominent features. In this Section, we also extend the model to the case of no-slip top and bottom boundaries. In the latter case, we systematically derive all the linear terms and also the nonlinear terms entering the mean flow equation, but resort to model the nonlinear couplings arising in the equation for the convective mode w.

Assuming that the field w can be viewed as a superposition of straight rolls with different wave vectors, the nonlinear term $\mathcal{N}$ vanishes and $\Delta_h\mathcal{M} = 4\mathcal{H}$. This leads to replace eqs. (37)-(40) by

$$(\Delta_h - 4\pi^2)^2 w_2 - 4\pi r_0 \Delta_h \psi_2 + \Delta_h \theta_2 = \frac{3}{2}\frac{\pi}{q_c^2 P}\Delta_h\mathcal{M} \tag{45}$$

$$4\pi r_0 w_2 - (\Delta_h - 4\pi^2)\Delta_h \psi_2 = 0 \tag{46}$$

$$R_c w_2 + (\Delta_h - 4\pi^2)\theta_2 = \frac{3}{2}\frac{\pi}{q_c^2} q_p^2 \mathcal{M}. \tag{47}$$

Applying the operators $(\Delta_h - 4\pi^2)$ on eq. (45), $-4\pi r_0\Delta$ on eq. (46) and $-\Delta_h$ on eq. (47), and combining the resulting equations, we obtain

$$[(\Delta_h - 4\pi^2)^3 - (4\pi r_0)^2 - R_c\Delta_h] w_2 = -\frac{3}{2}\pi\frac{q_p^2}{q_c^2}\Delta_h\mathcal{M} + \frac{3}{2}\frac{\pi}{q_c^2 P}(\Delta_h - 4\pi^2)\Delta_h\mathcal{M}. \tag{48}$$

The action of the horizontal Laplacian Δ_h on straight rolls reduces to the multiplication by $-q_c^2$. For rotations sufficiently slow to keep q_c small enough compared to 2π, we replace $(\Delta_h - 4\pi^2)$ by $-4\pi^2$, an approximation also used in [17]. Note that, although often neglected, nonlocal effects may in some instance be relevant, as stressed in [18].

Performing this localization as a first step, eqs. (45)-(47) become

$$-[(4\pi^2)^3 + (4\pi r_0)^2] w_2 = -\pi[\frac{3}{2}\frac{q_p^2}{q_c^2}(1 + \frac{4\pi^2}{q_p^2 P})]\Delta_h\mathcal{M} \tag{49}$$

and

$$w_2 = \pi\lambda\Delta_h\mathcal{M} \tag{50}$$

$$\phi_2 = -2\pi^2\lambda\mathcal{M} \tag{51}$$

$$\theta_2 = -\kappa\mathcal{M} \tag{52}$$

$$\psi_2 = -r_0\lambda\mathcal{M} \tag{53}$$

with

$$\lambda = \frac{3}{2}\frac{q_p^2}{q_c^2}\frac{(1+\frac{4\pi^2}{q_p^2 P})}{[(4\pi^2)^3+(4\pi r_0)^2]}\ ,\ \kappa = \frac{3q_p^2}{8\pi q_c^2}\ . \tag{54}$$

Rescaling the spatial variables by q_c, the time by q_c^2, defining $W = w(\frac{g\pi\kappa q_c^4}{q_c^4\xi_0})^{\frac{1}{2}}$ and $\Psi = \psi_0(q_c^2\frac{g\pi\kappa q_c^4}{q_c^4\xi_0})$, and dropping the subscript h in the horizontal derivatives, we get

$$\tilde{\tau}_0\partial_t W = (\tilde{\epsilon}-(\Delta+1)^2)W - \mathcal{N}_l(W,\mathcal{M},\Psi) \tag{55}$$

$$\begin{aligned}(\partial_t - P\Delta)\Delta\Psi &= \frac{\pi^2}{2q_c^2}(1-(\frac{\tau}{q_p^2})^2)(\nabla\Delta W\times\nabla W)\cdot\hat{\mathbf{z}} \\ &- \frac{\tau\pi^2}{q_p^2 q_c^2}[(\Delta W)^2+\nabla W\cdot\nabla\Delta W]\ ,\end{aligned} \tag{56}$$

where $\tilde{\tau}_0 = (1+\frac{1}{P}(1-\frac{2\tau^2\pi^2}{R_c q_c^2}))$, $\tilde{\epsilon} = \frac{\epsilon}{q_c^4\xi_0}$ and $\mathcal{M} = W^2+(\nabla W)^2$.

The nonlinear coupling $\mathcal{N}_l$, resulting from the localization of eq. (23), is a complicated expression which, in the infinite Prandtl number limit, reduces to

$$\mathcal{N}_l^\infty = -\Delta\left(w\mathcal{M}+\alpha w\Delta\mathcal{M}-(\frac{1}{2}-2\alpha)\nabla w.\nabla\mathcal{M}+\frac{\tau}{2}\delta(\nabla w\times\nabla\mathcal{M})\cdot\hat{\mathbf{z}}\right) \tag{57}$$

with $\alpha = \frac{6q_p^2}{((4\pi^2)^3+(2\pi\tau)^2)}$ and $\delta = \frac{1}{q_p^2}(1+\frac{6q_p^4 q_c^2}{((4\pi^2)^3+(2\pi\tau)^2)})$. In this limit, the model is similar to that of [10] and [11]. In particular, the coefficient δ identifies with that arising in eq. (75) of [10] and the growth rate of the Küppers-Lortz instability is identical in both models. When the Prandtl number is decreased, this growth rate deviates however significantly from that obtained with the primitive Boussinesq equations. The localization procedure thus appears to be inadequate for rotating convection at small Prandtl number and we resorted to heuristically modify the nonlinear couplings resulting from the localization in a way which both simplifies their expressions and improves the description of the Küppers-Lortz and the small-angle instabilities. For this purpose, we select a few representative nonlinear terms originating from $\mathcal{N}_l$, retaining (with modified coefficients) the terms present at infinite Prandtl number, except the term proportional to $W\Delta\mathcal{M}$ since its contribution in the linear analysis is similar to that originating from $\nabla w\cdot\nabla\mathcal{M}$. Among the terms involving the stream function Ψ, we retain the advection term $(\nabla W\times\nabla\Psi)\cdot\hat{\mathbf{z}}$ and two additional terms, $W\Delta\Psi$ and $\nabla W\cdot\nabla\Delta\Psi$, which appear to be necessary in order to accurately reproduce the Küppers-Lortz instability growth rate. We also remove the outer Laplacian which does not affect the Küppers-Lortz stability. The effect of this operator is however significant far enough from onset where it contributes to distort the Busse balloon in a way similar to the non-variational terms added by Cross and Greenside [19]. The equation for the mean flow is kept unchanged. We finally get the simplified system

$$\tilde{\tau}_0 \partial_t W = (\tilde{\epsilon} - (\Delta + 1)^2) W - \mathcal{N}_l(W, \Psi) \tag{58}$$

$$\begin{aligned} (\partial_t - P\Delta)\Delta\Psi &= \alpha_0 (\nabla\Delta W \times \nabla W) \cdot \hat{\mathbf{z}} \\ &+ \alpha_6 [(\Delta W)^2 + \nabla W \cdot \nabla \Delta W] \end{aligned} \tag{59}$$

where $\mathcal{N}_l$ is now given by

$$\begin{aligned} \mathcal{N}_l(W, \Psi) &= \mathcal{M} W + \alpha_1 \nabla W \cdot \nabla \mathcal{M} + \alpha_2 (\nabla W \times \nabla \mathcal{M}) \cdot \hat{\mathbf{z}} \\ & \alpha_3 (\nabla W \times \nabla \Psi) \cdot \hat{\mathbf{z}} + \alpha_4 W \Delta \Psi + \alpha_5 \nabla W \cdot \nabla \Delta \Psi. \end{aligned} \tag{60}$$

In this system,

$$\tilde{\tau}_0 = (1 + \frac{1}{P}(1 - \frac{2\tau^2\pi^2}{R_c q_c^2})) \tag{61}$$

$$\tilde{\epsilon} = \frac{\epsilon}{q_c^4 \xi_0} \tag{62}$$

$$\alpha_0 = \frac{\pi^2}{2q_c^2}(1 - \beta^2) \tag{63}$$

$$\alpha_3 = 8\tilde{\tau}_0 \tag{64}$$

$$\alpha_4 = -\frac{8}{P}\frac{\pi^2}{q_c^2}\beta \tag{65}$$

$$\alpha_5 = \frac{16}{3P}\frac{\pi^2}{q_c^2}\beta \tag{66}$$

$$\alpha_6 = -\frac{\pi^2}{q_c^2}\beta \tag{67}$$

with $\beta = \frac{\tau}{q_p^2}$. The values of α_0, α_3 and α_6 directly result from the localization procedure. In contrast, the coefficients α_1 and α_2, are prescribed by fitting with the asymptotic model derived in Section 2.1. Indeed, a stability analysis similar to that leading to eqs. (42)-(43), gives in the present context

$$\partial_t \begin{bmatrix} b \\ z_1 \\ z_2 \end{bmatrix} = \begin{bmatrix} \tilde{\epsilon} g(\theta) & v_1(\theta) & v_2(\theta) \\ \tilde{\epsilon} p & -4P\sin^2\frac{\theta}{2} & 0 \\ \tilde{\epsilon} p & 0 & -4P\cos^2\frac{\theta}{2} \end{bmatrix} \begin{bmatrix} b \\ z_1 \\ z_2 \end{bmatrix} \tag{68}$$

with

$$g(\theta) = \frac{1}{\tilde{\tau}_0}(1 - \frac{(8 + 4\alpha_1 \sin^2\theta - 2\alpha_2 \sin 2\theta)}{(4 + \frac{\alpha_6}{8P}(4\alpha_4 + 8\alpha_5))}$$

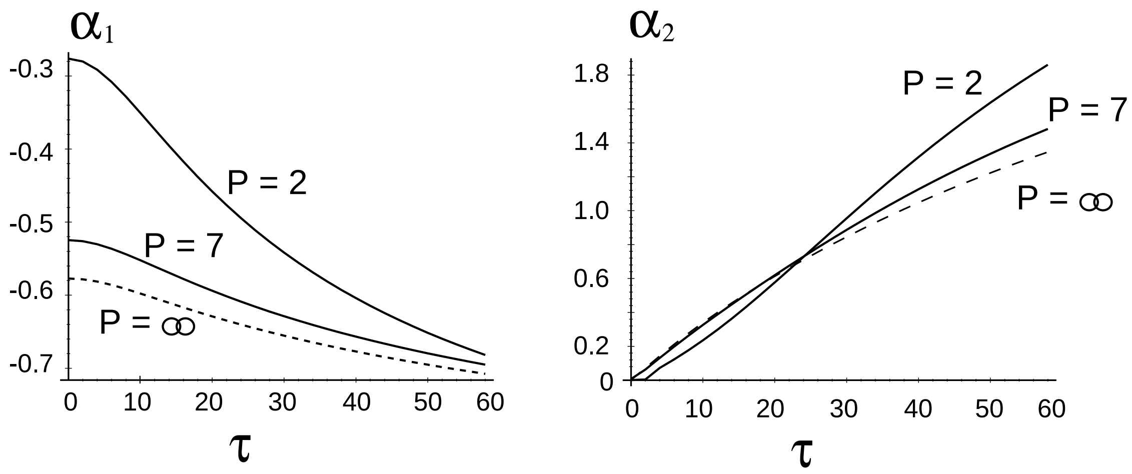

Figure 2: Variation with the rotation rate of the coefficients α_1 and α_2 entering eq. (60) of the simplified model for free-slip boundary conditions and different values of the Prandtl number.

$$\begin{aligned}
v_1(\theta) &= \frac{1}{\tilde{\tau}_0}(\alpha_3 \sin\theta + 4\alpha_4 \sin^2\frac{\theta}{2} + 8\alpha_5 \sin^4\frac{\theta}{2}) \\
v_2(\theta) &= \frac{1}{\tilde{\tau}_0}(-\alpha_3 \sin\theta + 4\alpha_4 \cos^2\frac{\theta}{2} + 8\alpha_5 \cos^4\frac{\theta}{2}) \\
p &= -\frac{\alpha_6}{(4 + \frac{\alpha_6}{8P}(4\alpha_4 + 8\alpha_5))} \;. \qquad (69)
\end{aligned}$$

The coefficients α_1 and α_2 are prescribed by minimizing $|G(\theta) - g(\theta)|^2$ by a mean-square method. The variation of the resulting coefficients with the rotation rate is illustrated for various Prandtl numbers in Fig. 2.

In order to test the validity of the above determination, we compare in Fig. 3 the growth rate obtained in Section 2.2 with that resulting from the primitive equation [6]. The fit is very accurate in the range of moderate Prandtl numbers we are here mostly interested in, but slightly deteriorates at infinite Prandtl number where the critical rotation rate given by the simplified model is $\tau_c = 45$ instead of $\tau_c = 47.8$. Simulations in the nonlinear regime also provide satisfactory agreement concerning the pattern formation between the simplified and asymptotic models. Note that further simplification like those corresponding to the model of [14] leads to a significant loss of accuracy in the estimate of the critical rotation for the Küppers-Lortz instability.

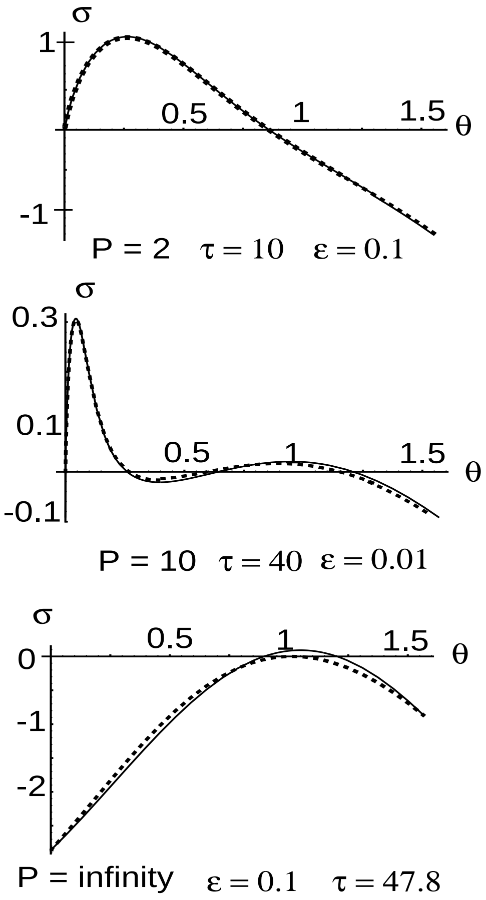

Figure 3: Growth rates of the small-angle and Küppers-Lortz instabilities obtained from the primitive equations (dashed line) and the simplified model (58)-(60) (solid line) for different values of P, τ and ϵ in the case of free-slip boundary conditions.

2.4 Modeling rigid boundaries

It is customary in the context of Swift-Hohenberg type equations, to model the effect of rigid boundaries by adding a term in the mean flow equation which takes into account the friction of the mean flow on the top and bottom plates. Indeed, while with free-slip boundaries, the mean flow is to leading order independent of the vertical coordinate, in the case of rigid boundaries it is to a good approximation a Poiseuille-type flow whose stream function can be modeled by $\Psi(x,y)\sin\pi z$. Projecting eq. (6) on this mode, the operator $\partial_t - P\Delta$ when acting on $\Psi(x,y)$, reads $\partial_t - P(\Delta_h + \pi^2)$, which after normalization leads to replace the l.h.s. of eq. (59) (where the subscript h has been dropped in the derivative operators with respect to the horizontal variables) by $(\partial_t - P(\Delta_h + \nu))\Delta_h$, with $\nu = \frac{\pi^2}{q_c^2}$. The value $\nu = 2$ used the literature [20], can be understood if one keeps $q_c = \frac{\pi}{\sqrt{2}}$, even in the case of rigid boundaries. In the presence of rotation, the effect of top and bottom rigid boundaries is in fact more subtle, and this led us to derive in a more systematic way, appropriate equations for this case.

Proceeding like in [13], we expand the temperature on the set of functions $\sin(2\pi nz)$ (in order to satisfy the boundary conditions $\theta(0) = \theta(1) = 0$), and use the eigenmodes of the operator $\frac{d^4}{dz^4}$ which vanish together with their first derivatives on $z = 0$ and $z = 1$, to expand the vertical velocity w. To leading order, we take $w = w_1 g(\pi z)$ where

$$g(z) = \frac{\cosh\lambda_1(\frac{z}{\pi} - 1/2)}{\cosh\lambda_1/2} - \frac{\cos\lambda_1(\frac{z}{\pi} - 1/2)}{\cos\lambda_1/2}, \tag{70}$$

with $\lambda_1 \approx 4.73004074$. Note that $\langle g(\pi z)^2\rangle \equiv \int_0^1 g^2(\pi z)dz = 1$. We also project ϕ and ψ on $g'(\pi z)$ and ψ_0 on $\sin\pi z$.

In the following, we systematically derive the linear part of the generalized Swift-Hohenberg system for rigid boundaries and model the nonlinear terms in the spirit of the couplings obtained with free-slip boundaries. We proceed like in Section 2, assuming the amplitude of w_1 of order $\epsilon^{\frac{1}{2}}$, the time derivative of order ϵ, with a Rayleigh number $R = (1+\epsilon)R_c$. We also write the horizontal Laplacian $\Delta_h = -q_c^2 + \mathcal{L}$. Since the nonlinear terms in the Boussinesq equations arise only at order $\epsilon^{\frac{3}{2}}$, we restrict ourselves to the linear terms. Projecting eq. (7) on $g(\pi z)$, eq. (6) on $g'(\pi z)$ and eq. (3) on $\sin(\pi z)$, we obtain

$$\begin{aligned} P^{-1}\partial_t(\Delta_h - g_1\pi^2)w_1 &= (\Delta_h - 2\pi^2\Delta_h g_1 + \pi^4 g_4)w_1 + g_s\Delta_h\theta_1 \\ &\quad -\pi\tau g_1\Delta_h\psi_1 \end{aligned} \tag{71}$$

$$(\partial_t - P(\Delta_h - g_2\pi^2)\Delta_h\psi_1 = -\tau P\pi w_1 \tag{72}$$

$$\partial_t\theta_1 - (\Delta_h - \pi^2)\theta_1 = 2Rg_s w_1 \tag{73}$$

with $g_1 = \langle g'(\pi z)^2 \rangle$, $g_2 = \frac{\langle g''(\pi z)^2 \rangle}{\langle g'(\pi z)^2 \rangle}$, $g_4 = \langle g(\pi z) g^{(4)}(\pi z) \rangle$ and $g_s = \langle g(\pi z) \sin(\pi z) \rangle$.

Applying the operators $(\Delta_h - g_2\pi^2)(\partial_t - (\Delta_h - \pi^2))$ on eq. (71), $(\Delta_h - g_2\pi^2) g_s \Delta_h$ on eq. (73), $P^{-1}\tau\pi g_1(\Delta_h - \pi^2)$ on eq. (72) and summing the resulting equations, we obtain at leading order, the critical Rayleigh number

$$R_c = \frac{q_p^2(q_c^4 + 2\pi^2 q_c^2 g_1 + \pi^4 g_4)}{2 g_s^2 q_c^2} + \frac{q_p^2 \pi^2 \tau^2 g_1}{2 g_s^2 q_c^2 q_{p2}^2}\ , \tag{74}$$

with $q_p^2 = q_c^2 + \pi^2$ and $q_{pi}^2 = q_c^2 + g_i\pi^2$, the critical wavenumber q_c being given by the condition $\frac{\partial R_c(q_c)}{\partial q} = 0$ which arises at the order ϵ of the expansion.

At order $\epsilon^{\frac{3}{2}}$, the nonlinear terms are relevant but, as already mentioned, they will be specified phenomenologically. The linear part of the equation for the convective mode reads

$$\tau_0 \partial_t w_1 = \epsilon w_1 - \xi_0 \mathcal{L}^2 w_1 \tag{75}$$

where

$$\tau_0 = \frac{1}{q_p^2}\left(1 + P^{-1}\left(\frac{q_p^4 q_{p1}^2}{2 R_c g_s^2 q_c^2} - \frac{q_p^4 g_1 \pi^2 \tau^2}{2 R_c g_s^2 q_{p2}^4 q_c^2}\right)\right) \tag{76}$$

and

$$\xi_0 = \frac{2 q_{p1}^2 + q_p^2}{2 R_c g_s^2 q_c^2} - \frac{g_1 \pi^2 \tau^2}{2 g_s^2 q_c^2 R_c q_{p2}^2}\left(1 - \frac{q_p^2}{q_{p2}^2}\right). \tag{77}$$

In the absence of rotation, we thus have $\tau_0 = (1 + 0.5143 P^{-1})/19.46$, to be compared with the value $\tau_0 = (1 + 0.5117 P^{-1})/19.65$ obtained using a projection on three Galerkin modes [25]. Similarly, we obtain for $\bar{\xi}_0^2 = 4 q_c^2 \xi_0$ (a quantity usually denoted ξ_0^2 in the literature) the value 0.151 instead of 0.148. The leading order of the vertical vorticity equation (72) gives $\psi_1 = \frac{\pi}{q_c^2}\beta w_1$ where $\beta = \frac{\tau}{q_{p2}^2}$, and the incompressibility condition implies $\phi_1 = \frac{\pi}{q_c^2} w_1$. We thus write

$$\mathbf{V} = \begin{bmatrix} \frac{\pi^2}{q_c^2}(\partial_x + \beta\partial_y) w_1\ g'(\pi z) + \partial_y \psi_1\ \sin(\pi z) \\ \frac{\pi^2}{q_c^2}(\partial_y - \beta\partial_x) w_1\ g'(\pi z) - \partial_x \psi_1\ \sin(\pi z) \\ w_1\ g(\pi z) \end{bmatrix}. \tag{78}$$

Using eq. (78) in the next order contribution to the equation for the vertical vorticity, projecting on the $\sin(\pi z)$ mode and rescaling the dependent and independent variables like in the free-slip case, we get

$$\begin{aligned} (\partial_t - P(\Delta - \nu))\Delta\Psi &= \alpha_0(\nabla_h \Delta W \times \nabla W) \\ &+ \alpha_6((\Delta W)^2 + \nabla W . \nabla \Delta W) + \alpha_7 \Delta(W^2) \end{aligned} \tag{79}$$

where

$$\begin{aligned}
\alpha_0 &= (4\langle g'^2(\pi z)\sin(\pi z)\rangle)\frac{\pi^2}{2q_c^2}(1-\beta^2) && (80)\\
\alpha_6 &= -(4\langle g^2(\pi z)\sin(\pi z)\rangle)\frac{\beta\pi^2}{q_c^2} && (81)\\
\alpha_7 &= -\langle (g''(\pi z)g(\pi z)+g'^2(\pi z))\sin(\pi z)\rangle\frac{\beta\pi^2}{q_c^2} && (82)\\
\nu &= \frac{\pi^2}{q_c^2}. && (83)
\end{aligned}$$

It is noticeable that, when compared to its analog in the case of free-slip boundaries, eq. (79) includes an additional term proportional to $\Delta(W^2)$ originating from the vertical Reynolds stress.

Returning to the equation for the vertical velocity, we model the nonlinear couplings like in the case of free-slip boundaries. Neglecting the last two terms in the r.h.s. of eq. (59) which are used to refine the stability analysis of straight parallel rolls in the case of free-slip boundary conditions, we find

$$\tilde{\tau}_0\partial_t W = (\tilde{\epsilon}-(\Delta+1)^2)W - [W\mathcal{M} + \alpha_1\nabla W.\nabla\mathcal{M} + \alpha_2\nabla W\times\nabla\mathcal{M} + \alpha_3\nabla W\times\nabla\Psi] \quad (84)$$

with

$$\tilde{\tau}_0 = \frac{\tau_0 q_c^2}{q_c^4\xi_0}\ , \quad \tilde{\epsilon} = \frac{\epsilon}{q_c^4\xi_0}. \quad (85)$$

The coefficients α_1, α_2 and α_3 are prescribed as follows. Like in the case of free-slip boundaries, we take $\alpha_3 = \gamma_3\tilde{\tau}_0$, with a coefficient γ_3 to be determined. Similarly, we take $\alpha_2 = \gamma_2\tilde{\tau}_0$, since in the free-slip case, the variation of α_2 with the rotation rate is almost linear. Finally, we choose $\alpha_1 = -\gamma_1\tilde{\tau}_0$ since the corresponding term disappears in the absence of rotation. The coefficients γ_1, γ_2 and γ_3 are determined in such a way as to recover accurately the Küppers-Lortz instability for moderate Prandtl numbers and the zig-zag instability boundary in the absence of rotation. The latter constraint is met by comparing the predictions of the phase equation analysis made in Section 3 (see eq. (104)), with that performed on the primitive Boussinesq equations with rigid boundary conditions [21]. Note that an accurate description of the right hand boundary of the Busse balloon (skewed-varicose instability) requires the inclusion of non-variational additional terms [19]. In a neighborhood of threshold (whose extension increases with the Prandtl number), the present model however provides an adequate representation of the long wavelength instabilities.

In practice the model has been considered for different values of the Prandtl number for which the onset of the Küppers-Lortz instability is computed in [4] or [5]. This leads to the numerical values of the coefficients γ_1, γ_2 and γ_3 given in Table 1.

P	θ_{KL}	τ_{KL}	$(\tilde{\epsilon}_{\text{zig-zag}}, k_{\text{zig-zag}})$	γ_1	γ_2	γ_3
0.8	38.4^o	23.6	$(0.232, 0.866)$	-0.010	0.04904	1.4187
1.2	46^o	29.6	$(0.232, 0.875)$	0.0106	0.02005	2.1644
2	50^o	38	$(0.4708, 0.847)$	0.0112	0.02077	2.3076
6.8	59.1^o	46.2	$(0.4754, 0.8502)$	0.0147	0.00759	8.809
50	59.7^o	54.8	$(0.8, 0.9778)$	0.0120	0.02002	5.0
∞	59.7^o	54.8	- -	0.0120	0.02132	0

Table 1: Values of the coefficients γ_1, γ_2 and γ_3 entering the model with rigid boundary conditions (see text) for various values of the Prandtl number, together with characteristics of the KL and zig-zag instabilities.

3 Weakly nonlinear dynamics

3.1 Nonlinear development of the small-angle instability

At finite Prandtl number and moderate rotation, the development of the small-angle instability is visualized by solving the model equations (58)-(60), starting with straight parallel rolls of critical wave number, perturbed by a small isotopic noise. Under the effect of the small-angle instability, the rolls distort and shear layers are formed as seen in Fig. 4. The reconnection of the rolls leads to a global rotation of the pattern in the direction of the external rotation. Indeed, the vorticity generated by the last term in the right hand side of eq. (59) has preferentially the sign of the external rotation. This process is easily seen in Fourier space where the leading mode rotates on the critical circle.

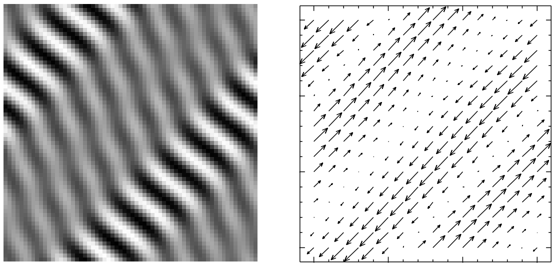

Figure 4: Weakly nonlinear dynamics resulting from the small-angle instability for $P = 2$, $\tau = 10$ and $\tilde{\epsilon} = 0.1$: (a) convection rolls; (b) mean flow stream function.

3.2 Derivation of the phase-mean drift equations

In order to describe the phase modulation of straight parallel rolls, we proceed as in [22] and introduce the slow variables $\vec{X} = \eta\vec{x}$, $T = \eta^2 t$. We also denote by θ the phase variable, by $\Theta = \eta^{-1}\theta$ the slow phase and $\vec{K} = \nabla_X\Theta$ the local wave-vector. We are thus led to replace, in the models with free slip (eqs. (58) and (59)) or rigid (eqs. (84) and (79)) boundary conditions , the time derivative ∂_t by $\eta\partial_T\Theta\partial_\theta + \eta^2\partial_T$, the gradient ∇ with respect to X by $\vec{K}\partial_\theta + \eta\nabla$ and the Laplacian ∇^2 by $K^2\partial_\theta^2 + \eta D_1\partial_\theta + \eta^2\nabla^2$ with $D_1 = 2\vec{K}.\nabla + \nabla\vec{K}$. We expand the solution $\mathcal{S} = \begin{pmatrix} W \\ \Psi \end{pmatrix}$ as

$$\mathcal{S} = \mathcal{S}_0 + \eta\mathcal{S}_1 + \ldots = \begin{pmatrix} w_0 & + & \eta\, w_1 + \ldots \\ \psi_0 + \zeta_0 & + & \eta\, (\psi_1 + \zeta_1) + \ldots \end{pmatrix} \tag{86}$$

where the contributions depending on the fast phase θ are isolated in the quantities ζ_i.

At leading order, we have

$$\mathcal{L}_0 S_0 \equiv \begin{pmatrix} \hat{O}_{11} & \hat{O}_{12} \\ \hat{O}_{21} & \hat{O}_{22} \end{pmatrix} = 0 \ , \tag{87}$$

where

$$\begin{aligned} \hat{O}_{11} &= (-\epsilon + (K^2\partial_\theta^2 + 1)^2)w_0 + [w_0^3 + w_0(\partial_\theta w_0\vec{K})^2 \\ &\quad +\alpha_1(K^2\partial_\theta w_0\partial_\theta(w_0^2) + K^4\partial_\theta w_0\partial_\theta(\partial_\theta w_0)^2) \\ &\quad +\alpha_4(w_0K^2\partial_\theta^2\psi_0) + \alpha_5(K^4\partial_\theta w_0\partial_\theta^3\psi_0)] \qquad (88) \\ \hat{O}_{12} &= \alpha_4(w_0K^2\partial_\theta^2\psi_0) - \alpha_5(K^4\partial_\theta w_0\partial_\theta^3\psi_0) \qquad (89) \\ \hat{O}_{21} &= P(-K^2\partial_\theta^2 + \nu)\partial_\theta^2\psi_0 \qquad (90) \\ \hat{O}_{22} &= -\alpha_6(K^4\partial_\theta w_0\partial_\theta^3 w_0 + K^4(\partial_\theta^2 w_0)^2) - \alpha_7 K^2\partial_\theta^2 w_0^2. \qquad (91) \end{aligned}$$

Retaining only the first mode in a Galerkin expansion, we write the solution in the form ($w_0 = A\cos\theta,\ \psi_0 = A^2\phi\cos 2\theta$), with $\phi = -\frac{\alpha_6 K^2 - 2\alpha_7}{4P(\nu + 4K^2)}$ and

$$A^2 = \frac{(\tilde{\epsilon} - (K^2-1)^2)}{\frac{3}{4} + \frac{K^2}{4} + \frac{1}{2}\alpha_1 K^2(1-K^2) - 2K^2\phi(\alpha_4 + 2K^2\alpha_5)}. \tag{92}$$

The evolution of ζ_0 is determined at the next order of the expansion.

At order η, the equation takes the form

$$\delta\mathcal{L}_0\mathcal{S}_1 = \mathcal{F}_1 \tag{93}$$

where $\delta\mathcal{L}_0$ is the linearization of the operator $\mathcal{L}_0$ about the steady solution and $\mathcal{F}_1$ collects the terms of order η not involving S_1. The solvability conditions are obtained by taking the scalar product $\langle a, b\rangle = \frac{1}{2\pi}\int_0^{2\pi} ab\ d\theta$ of the r.h.s. of eq. (93) with the vectors which span the null space of the adjoint $\delta\mathcal{L}_0^\dagger$ of the operator $\mathcal{L}_0$, namely $e_1 = (\sin\theta, \gamma\sin 2\theta)$ where $\gamma = -A\frac{(\alpha_4+2\alpha_5K^2)}{2P(\nu+4K^2)}$, and $e_2 = (0,1)$. The first solvability condition gives the phase diffusion equation

$$\tau(K)\ \partial_T\Theta \quad + \quad g(K)\ \vec{K}\times\nabla\zeta_0 + a(K)\ (\vec{K}\cdot\nabla)K^2 + b(K)\ (\vec{K}\times\nabla)K^2 + c(K)\ \nabla\cdot\vec{K} = 0 \qquad (94)$$

with

$$\begin{aligned}
\tau(K) &= \frac{1}{2}\tau_0 A^2 - 4\gamma K^2 A^3\phi && (95)\\
g(K) &= \frac{1}{2}\alpha_3 A^2 && (96)\\
a(K) &= -A^2 + (1-K^2)\frac{dA^2}{d(K^2)} + \frac{1}{8}A^2\frac{dA^2}{d(K^2)}\\
&\quad +\alpha_1\left(\frac{1}{4}(1+2K^2)A^2\frac{dA^2}{d(K^2)} + \frac{3}{8}A^4\right) + \alpha_4 A^2\frac{d(A^2\phi)}{d(K^2)}\\
&\quad +\alpha_5\left(2K^2A^2\frac{d(A^2\phi)}{d(K^2)} + A^4(\phi + K^2\frac{d\phi}{d(K^2)})\right)\\
&\quad +\gamma(8PA^3(\phi + K^2\phi\frac{dA^2}{d(K^2)} + 2K^2\frac{d\phi}{d(K^2)})\\
&\quad +2P(\nu+4k^2)(A\frac{d(\phi A^2)}{d(K^2)}) + \alpha_6(K^2A\frac{dA^2}{d(K^2)} + \frac{1}{4}A^3) - 2\alpha_7 A\frac{dA^2}{d(K^2)})\\
& && (97)\\
b(K) &= -\alpha_2\left(\frac{1}{2}A^2K^2\frac{dA^2}{dK^2} + \frac{3}{8}A^4\right) - \frac{1}{4}\alpha_3A^2\left(2\phi\frac{dA^2}{dK^2} + A^2\frac{d\phi}{dK^2}\right)\\
&\quad +\gamma\alpha_0\left(\frac{1}{8}A^2(K^2-1)\frac{dA^2}{dK^2} - \frac{1}{4}A^3\right) && (98)\\
c(K) &= (1-K^2)A^2 + \frac{1}{2}\alpha_4A^2\phi + \alpha_5K^2A^2\phi + \gamma(P\phi A^3(\nu+8K^2)\\
&+ \frac{3}{4}\alpha_6A^3 - \alpha_7A^3). && (99)
\end{aligned}$$

The second solvability condition is always satisfied, and the expansion must thus be pushed to the next order.

At order η^2, we have an equation of the form

$$\delta\mathcal{L}_0\mathcal{S}_2 = \mathcal{F}_2\ , \qquad (100)$$

and the solvability condition coming from the orthogonality of $\mathcal{F}_2$ with e_2 gives the mean flow equation

$$(\eta^2(\partial_T - P\nabla^2) + P\nu)\nabla^2\zeta_0 = \frac{\alpha_0}{2}\nabla \times (\vec{K}\nabla.(\vec{K}A^2)) + \frac{\alpha_6}{2}\nabla.(\vec{K}\nabla.(\vec{K}A^2)) + \frac{\alpha_7}{2}\nabla^2 A^2 \tag{101}$$

which together with eq. (94) provides the phase-mean drift system. To study the stability of the straight parallel rolls, we linearize eqs. (94), (101) about the solution $\Theta = kX$ and $\zeta_0 = 0$. The system for the perturbations φ and ξ of the phase and of the mean flow reads

$$\tau(k)\partial_T\varphi + g(k)\partial_Y\xi + 2a(k)k^2\partial_{XX}\varphi + 2b(k)k^2\partial_{XY}\varphi + c(k)\nabla^2\varphi = 0 \tag{102}$$

$$\begin{aligned}(\eta^2(\partial_T - P\nabla^2) + P\nu)\nabla^2\xi = &-\frac{\alpha_0}{2}\left(kA(k)^2\partial_Y\nabla^2\varphi + 2k^3\frac{dA^2}{d(K^2)}(k)\partial_{XXY}\varphi\right)\\ &+\frac{\alpha_6}{2}\left(kA(k)^2\partial_X\nabla^2\varphi + 2k^3\frac{dA^2}{d(K^2)}(k)\partial_{XXX}\varphi\right) + \alpha_7 k\frac{dA^2}{d(K^2)}(k)\partial_X\nabla^2\varphi.\end{aligned} \tag{103}$$

Considering normal modes proportional to $e^{i\vec{\kappa}\cdot\vec{X}+\sigma T}$ with $\vec{\kappa} = (\kappa\cos\rho, \kappa\sin\rho)$, we obtain for the growth rate σ, a quadratic equation. One of the solutions is always negative. The other is given by

$$\begin{aligned}\frac{\sigma}{\kappa^2} \;=\; &\frac{1}{2\tau(k)\eta^2}(-(\tau(k)P(\eta^2+\nu) - \eta^2(2a(k)k^2\cos^2\rho + b(k)k^2\sin 2\rho + c(k))) +\\ &\{(\tau(k)P(\eta^2+\nu) + \eta^2(2a(k)k^2\cos^2\rho + b(k)k^2\sin 2\rho + c(k)))^2\\ &-4\tau(k)\eta^2 g(k)(\alpha_0\sin^2\rho - \alpha_6\sin\rho\cos\rho)k(\frac{A(k)^2}{2} + k^2\frac{dA^2}{d(K^2)}(k)\cos^2\rho)\\ &-4\tau(k)\eta^2 g(k)(-\alpha_7\sin\rho\cos\rho k\frac{dA^2}{d(K^2)}(k))\}^{\frac{1}{2}})\end{aligned} \tag{104}$$

In eq. (104), $\alpha_7 = \nu = 0$ in the case of free-slip boundary conditions while $\alpha_4 = \alpha_5 = 0$ for rigid boundary conditions.

3.3 Relation between the small-angle and the skewed-varicose instabilities

In the absence of rotation and for free-slip boundaries, straight parallel rolls with a wavenumber larger than critical, were shown to be unstable with respect to the skewed-varicose instability [15], [16]. This phenomenon is recovered by computing the stability balloon from eq. (104). Taking the critical wavenumber q_c as unity, the result is illustrated in Fig. 5 for $P = 2$ and $\eta = 10^{-2}$. The dependency of the growth rate of the skewed-varicose instability with the angle ρ associated to the phase perturbation is presented in Fig. 6a for rolls of wave number $k = 1.03$ and the same values of P and η as in Fig. 5. We note that, as usual, the growth rate is symmetric in terms of ρ.

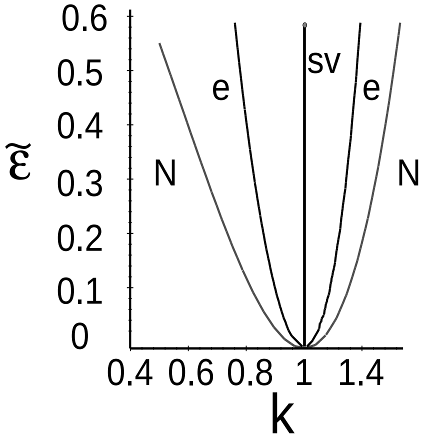

Figure 5: Stability balloon relatively to long-wave instabilities in the case of free-slip boundary conditions for $P = 2$ and $\eta = 10^{-2}$, in the absence of rotation. Here, **e** represents the frontier of the Eckhaus instability and **sv** that of the skewed-varicose instability. Furthermore, **N** is the neutral curve for convection onset.

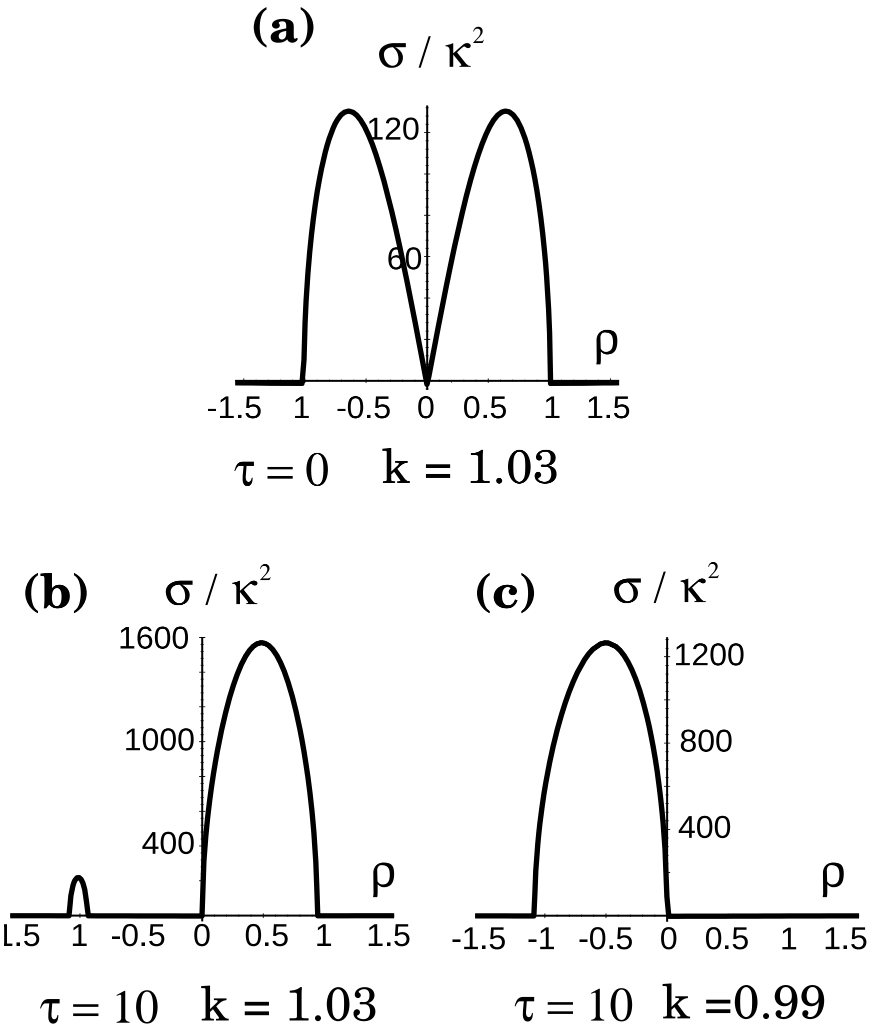

Figure 6: Growth rate σ/κ^2 relatively to long wave perturbations for $P = 2$ and $\eta = 10^{-2}$: (a) no rotation and basic rolls with wave-number $k = 1.03$, (b) rotation rate $\tau = 10$ and roll wavenumber $k = 1.03$ (in units of q_c); (c) rotation rate $\tau = 10$ and roll wavenumber $k = 0.99$.

When rotation is turned on, we observe that for $k > 1$, the skewed-varicose instability becomes "asymmetric", the growth rate being now maximum for a finite value of the angle ρ whose sign is that of the rotation (Fig. 6b). When k is smaller than critical, the unstable modes are associated to values of ρ whose sign is opposite to that of the external rotation (Fig. 6c). In physical space, a phase perturbation with an angle ρ produces a distortion of the rolls where compressed and dilated regions alternate along an axis making the same angle with k. The associated mean flow displays shear layers perpendicular to this axis. According to the angle ρ, the perturbation is amplified or not, as predicted by the phase modulation analysis. Note that the aspect ratio of the box required to validate the phase theory increases with the rotation rate.

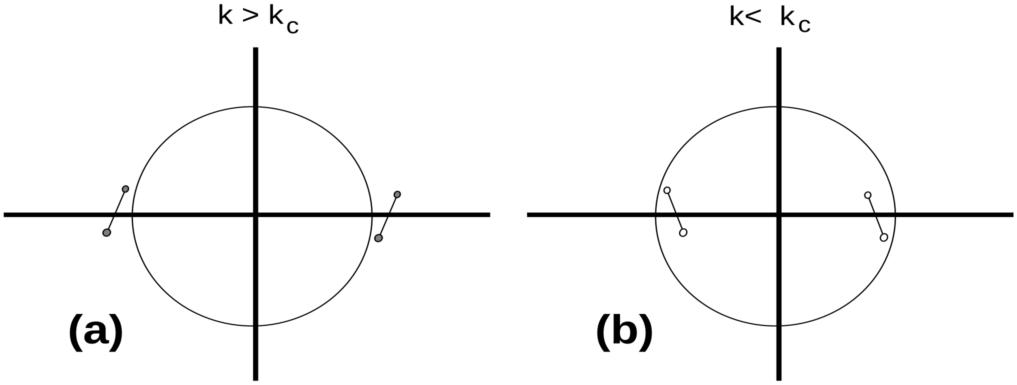

Figure 7: Sketch in Fourier space of the couples of modes $e^{\pm i(\vec{k}\pm\eta\vec{\kappa}).\vec{x}}$ associated to the phase instability, for $k > q_c$ (a) and $k < q_c$ (b), together with the critical circle (of radius q_c).

It is of interest to compare more precisely the small-angle instability resulting from an amplitude perturbation with the asymmetric skewed-varicose instability associated to a phase perturbation. By inspection of eq. (44), it is easily seen that in the small-angle boundary layer, the growth rate of the amplitude perturbation scales like θ^2, where θ is the angle between the basic and the perturbation wave vectors, while eq. (104) shows that the growth rate of the phase perturbation (in the primitive variables) scales like the inverse aspect ratio η of the box. On the other hand, in such a box, the minimum perturbation angle θ is of order $\eta^{1/2}$. It follows that both growth rates scale like the inverse aspect η and not like η^2, as usual for phase instabilities in the case of no-slip top and bottom boundaries. This larger growth rate results from the strong magnitude of the mean flow.

Furthermore, both instabilities lead to a similar dynamics in physical space, governed by the formation of shear layers which trigger the reconnection of the rolls and their global rotation. Nevertheless, the eigenmodes involved in the two descriptions of what appears to be essentially the same instability, are different. In the amplitude framework, the perturbation consists in a single Fourier mode, which is always unstable if the angle of its wave vector with that of the basic rolls, has the sign of the external rotation. In the phase formalism in contrast, the perturbing modes can be viewed as a couple of satellites whose separation scales like the inverse aspect ratio η of the convection cell. In a confined system, the distance between the two satellites is sufficient to make the associated modes evolve as two independent amplitude perturbations. In contrast, when the aspect ratio of the box is large enough, the interaction of the two satellites is resonant and a mode which alone would be unstable, may be stabilized by the presence of its companion, as predicted by the phase theory. When the wavenumber is distinct from critical, the sign of the rotation can be predicted by noticing that among the two satellite modes produced by the phase perturbation, the closest to the critical circle will be preferentially amplified (Fig. 7). For example, for positive rotation and $k > q_c$, the instability correspond to positive ρ (see Fig. 6b) and the rotation will be in the negative direction. Similarly, for $k < q_c$, modes with negative ρ are unstable (Fig. 6c) and the rotation also takes place in the negative direction. After a while, the mode close to the critical circle becomes dominant and the pattern undergoes a dynamics prescribed by the amplitude theory, possibly leading to the reversal of the rotation direction (Fig. 8).

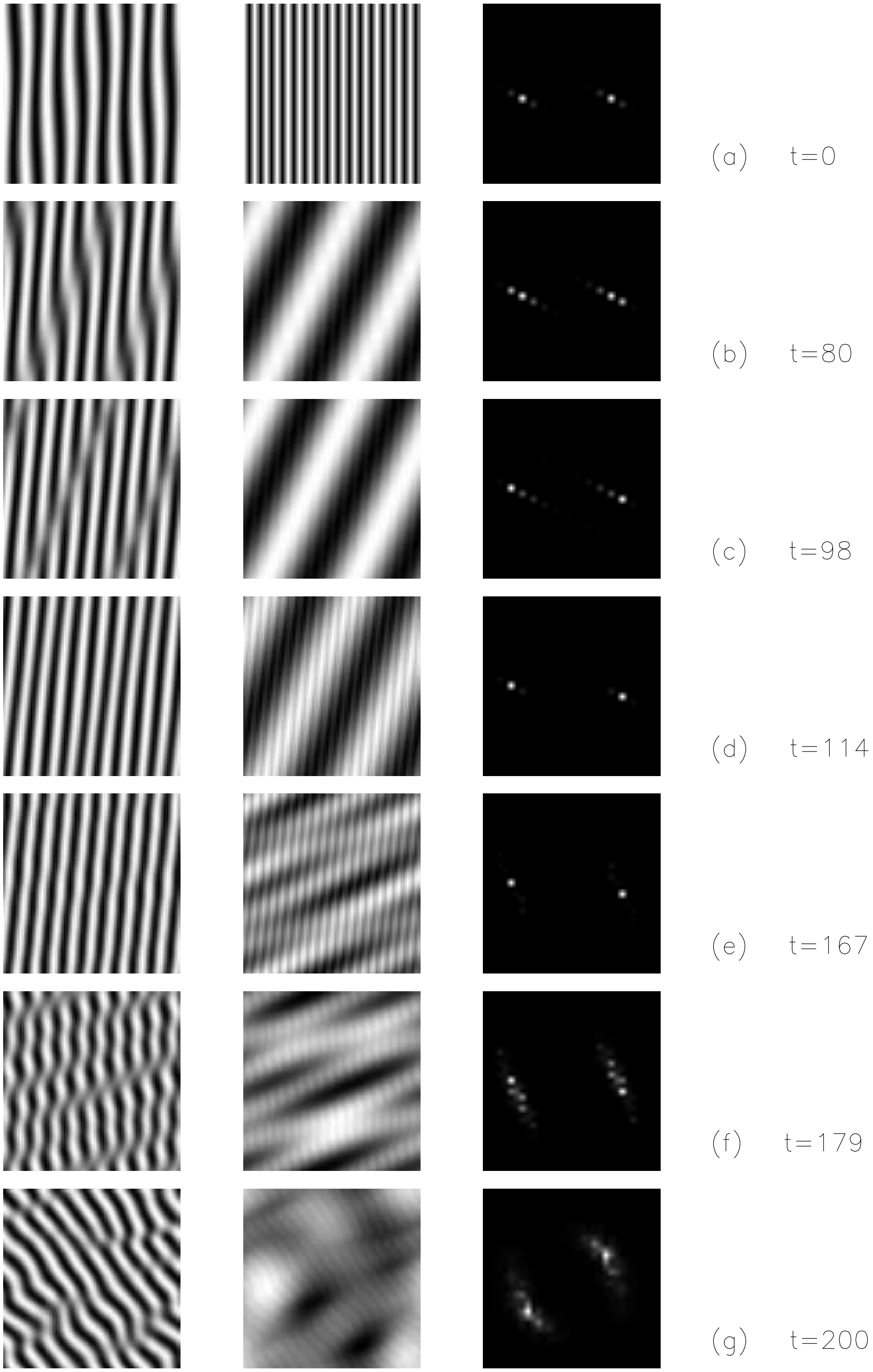

Figure 8: Time evolution of parallel rolls with wavenumber $k = 0.9$ for $\tilde{\epsilon} = 0.3$, $\tau = 10$ subject to a phase perturbation: Convective mode (left), mean flow stream function (middle) and two dimensional energy spectrum of the convective mode (right).

3.4 Busse balloons for rigid boundary conditions

We first display in Fig. 9 the stability balloon in the absence of rotation for our model with rigid boundary conditions for $P = 0.8$ and $P = 6.8$. Figure 10 displays the stability balloon for both Prandtl numbers in the presence of rotation. They qualitatively agree near threshold with those derived from the primitive equations [3]. Since our analysis is limited to a neighborhood of threshold, we did not include as in [19], corrective terms designed to bend the balloon at higher values of ϵ. In this context, it is of interest to consider more precisely the effect of the rotation on the skewed-varicose instability, a question addressed experimentally in [9]. Tables 2 and 3 show for $P = 0.8$ and $\tilde{\epsilon} = 0.3$ and 0.5, corresponding to two essentially constant values of the normalized distance ϵ to convection threshold, that the angle θ_{SV} of the wavevector perturbation decays linearly like in the experimental results displayed on figure 18 of [9]. The growth ot the critical wavenumber k_{SV} (see figure 2 of [9]) is however underestimated.

Figure 11 displays the stability border relative to long-wave instabilities in the plane (k,ρ). The symmetry (for $\tau = 0$) with respect to the phase perturbation angle ρ, which holds for $\tau = 0$ is broken in presence of rotation, like with free-slip boundary conditions.

$\Omega = \tau/2$	k_{SV}	θ_{SV}	ϵ
0	1.13867	46^o	0.108
5	1.1402	41.8^o	0.109
7	1.1411	40^o	0.1097
10	1.143	37^o	0.111
15	1.14696	33.46^o	0.1137

Table 2: Variation of the critical wavenumber and of the angle of the skewed-varicose instability for P =0.8 and $\tilde{\epsilon} = 0.3$.

$\Omega = \tau/2$	k_{SV}	θ_{SV}	ϵ
0	1.1733	44.91^o	0.1805
5	1.1759	40.68^o	0.1817
7	1.1776	38.96^o	0.1829
10	1.1806	36.66^o	0.1851
15	1.1873	32.65^o	0.1895

Table 3: Variation of the critical wavenumber and of the angle of the skewed-varicose instability for P =0.8 and $\tilde{\epsilon} = 0.5$.

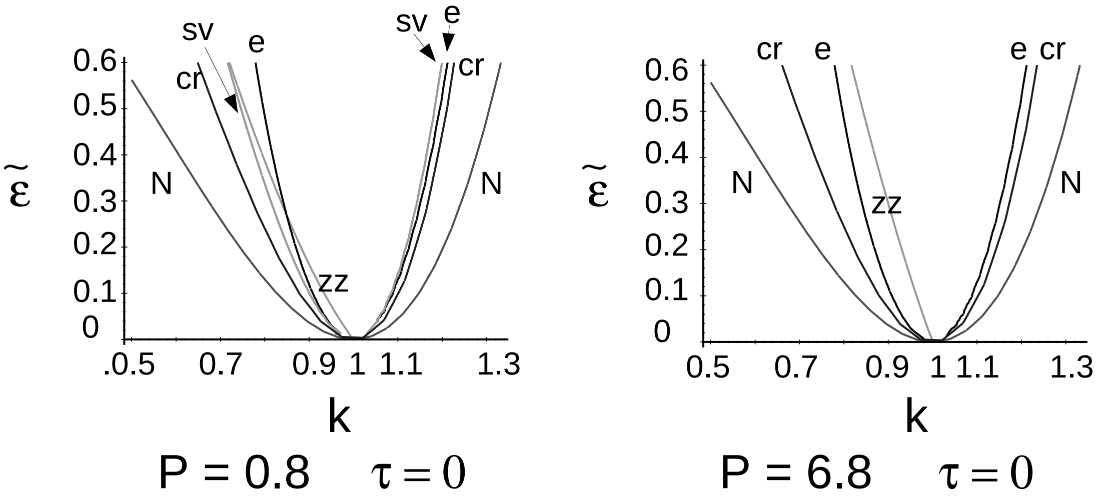

P = 0.8 $\tau = 0$ P = 6.8 $\tau = 0$

Figure 9: Instability balloon for rigid boundary conditions in the absence of rotation for Prandtl numbers $P = 0.8$ (a) and $P = 6.8$ (b). Here **e**, **sv**, **cr** and **zz** represent the frontiers of the Eckhaus, skewed-varicose, cross-roll and zig-zag instabilities respectively. **N** is the neutral curve for the onset of convection.

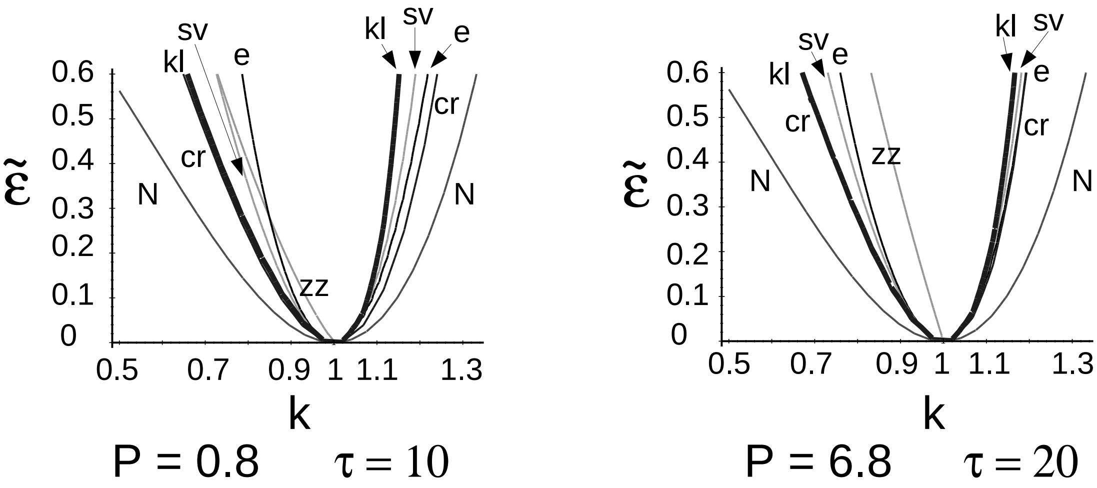

P = 0.8 $\tau = 10$ P = 6.8 $\tau = 20$

Figure 10: Instability balloon in the presence of rotation ($\tau = 20$) for rigid boundary conditions at Prandtl numbers $P = 0.8$ and $P = 6.8$. The labels if the long-wave instability boundaries are those of Fig. 9, while **kl** refers to the Küppers-Lortz instability.

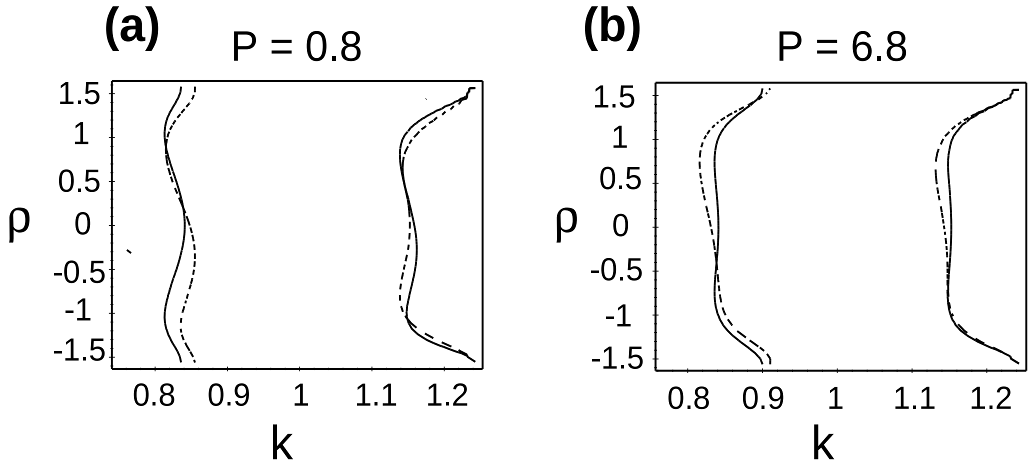

Figure 11: Stability domain in absence of rotation (solid line) and with a rotation rate $\tau = 20$ (dashed line) in the (k, ρ)-plane of the wavenumber and angle of phase perturbation, for the long-wave instabilities shown in Fig. 10, when $\tilde{\epsilon} = 0.3$, $\eta = 10^{-2}$ and $P = 0.8$ (a) or 6.8 (b).

4 Nonlinear dynamics for free-slip boundary conditions

In order to simulate the fully nonlinear regime, eqs. (58)-(60) where integrated with resolution ranging from 128^2 to 256^2 collocation points, according to the number of rolls in the convection cell. The initial conditions consist in a random noise with a spectrum localized in an annulus centered around the critical wave-number.

Typical snapshots of patterns emerging in the absence of rotation are displayed in Figs. 12 et 13. At infinite Prandtl number, labyrinthic rolls [23] are observed (Fig. 12), while the now classical spiral turbulence state is obtained for Prandtl number of order unity (Fig. 13).

The Küppers-Lortz instability regime which develops at infinite Prandtl number and moderate rotation is shown in Fig. 14 for $\tau = 50$ and $\epsilon = 0.2$. We observe the formation of patches of parallel rolls of different orientations. As time elapses, each patch is gradually replaced by another one whose rolls are rotated by an angle close to 60^o degrees, a dynamics similar to that described in [24] and [25]. The chaotic dynamics due to the KL instability is essentially governed by the propagation of dislocation arrays separating randomly oriented roll patches whose size is reduced as ϵ is increases.

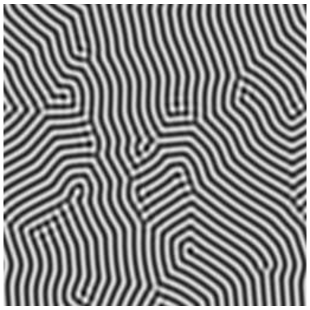

Figure 12: Labyrinthic pattern at infinite Prandtl number, for $\tilde{\epsilon} = 0.5$ and $\Gamma = 32$, in the absence of rotation.

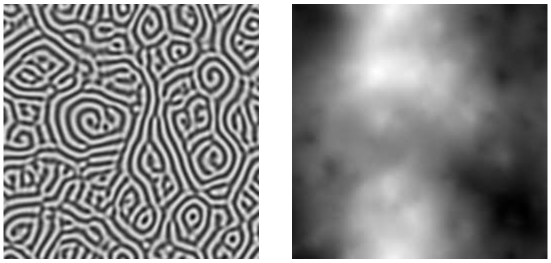

Figure 13: Convective pattern (left) and mean flow stream function (right) showing spiral turbulence in the case of free-slip boundary conditions, for $P = 1$, $\epsilon = 0.5$ and $\Gamma = 32$, in the absence of rotation.

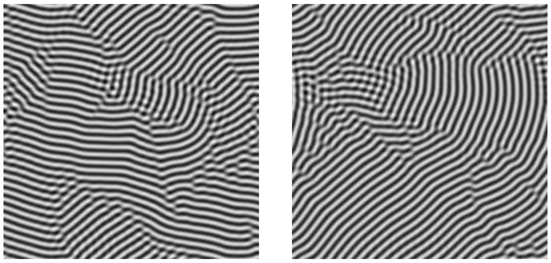

Figure 14: Snapshots of the roll patch dynamics at infinite Prandtl number for $\Gamma = 32$, $\tilde{\epsilon} = 0.2$ and a rotation rate $\tau = 50$.

Qualitatively different patterns are observed at smaller Prandtl numbers. This regime is illustrated in Fig. 15, which displays a snapshot of W and Ψ for $P = 2$, $\tau = 10$ and various values of the stress parameter ϵ. Near onset ($\epsilon = 0.01$), the pattern consists in large patches of slightly distorted parallel rolls (Fig. 15a), rotating slowly and reconnecting under the influence of the shear flow associated to the small-angle instability as discussed in Section 3.2. For $\epsilon = 0.05$, (Fig. 15b) we observe after about 10 horizontal diffusion times T_h, the emergence from the turbulent background, of a big target associated to a coherent vortex, which survives for about 13 T_h and is then destroyed by a large-scale shear. Note that in presence of rotation, the mean flow survives at the center of a perfectly isotropic target and that the targets rotate in the direction of the external rotation. For $\epsilon = 0.2$, the target keeps growing by accretion of adjacent rolls until it reaches the size of the computational domain, and then stabilizes (Fig. 15c). For an intermediate value of ϵ ($\epsilon = 0.1$), the target does not stabilize and a cyclic transition between a target and a spiral is observed (Fig. 16). When the rotation induces deformations, the most inner roll of the target meets its neighbor and a pair of dislocations is formed. One of them glides inwards, forming a spiral, while the other is rapidly convected outwards by the mean flow, producing a whirling line of low amplitude. The target reforms when a dislocation of the opposite sign reaches the center of the spiral. For larger ϵ, the target rotates more rigidly, and becomes stable.

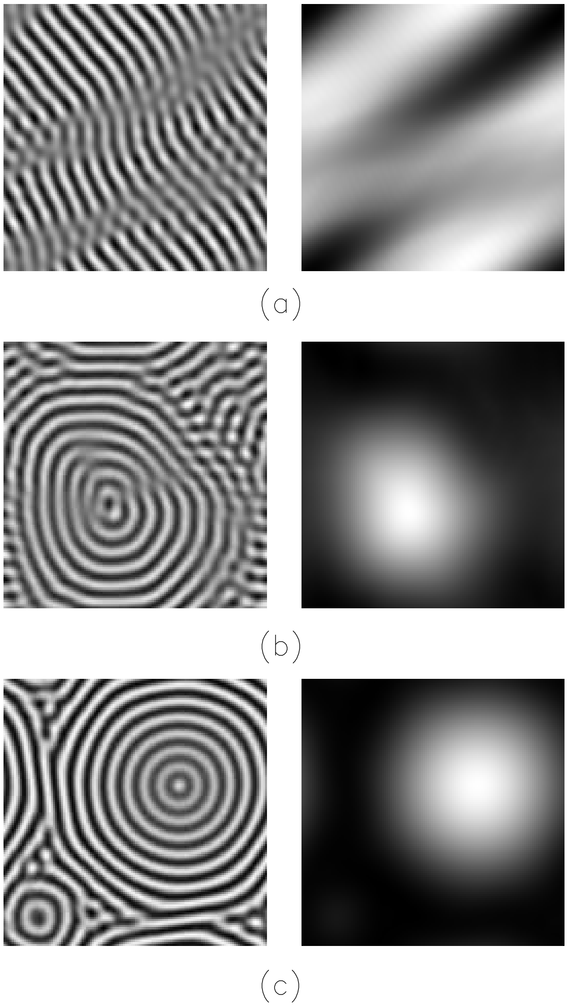

Figure 15: Convective pattern (left) and mean flow stream function (right) for free-slip boundary conditions with $P = 2$, $\tau = 10$, $\Gamma = 16$ and increasing values of the stress parameter: $\tilde{\epsilon} = 0.01$ (a), $\tilde{\epsilon} = 0.05$ (b), $\tilde{\epsilon} = 0.2$ (c).

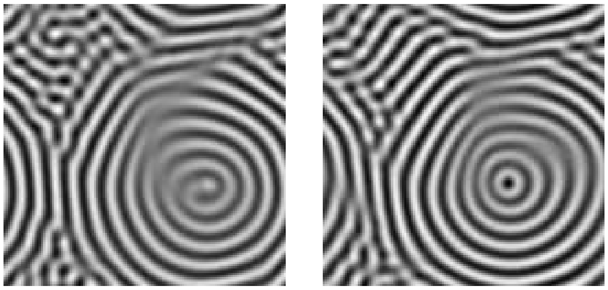

Figure 16: Transition between a spiral and a target for $P = 2$, $\tau = 10$, $\Gamma = 16$, $\tilde{\epsilon} = 0.1$ and free-slip boundary conditions.

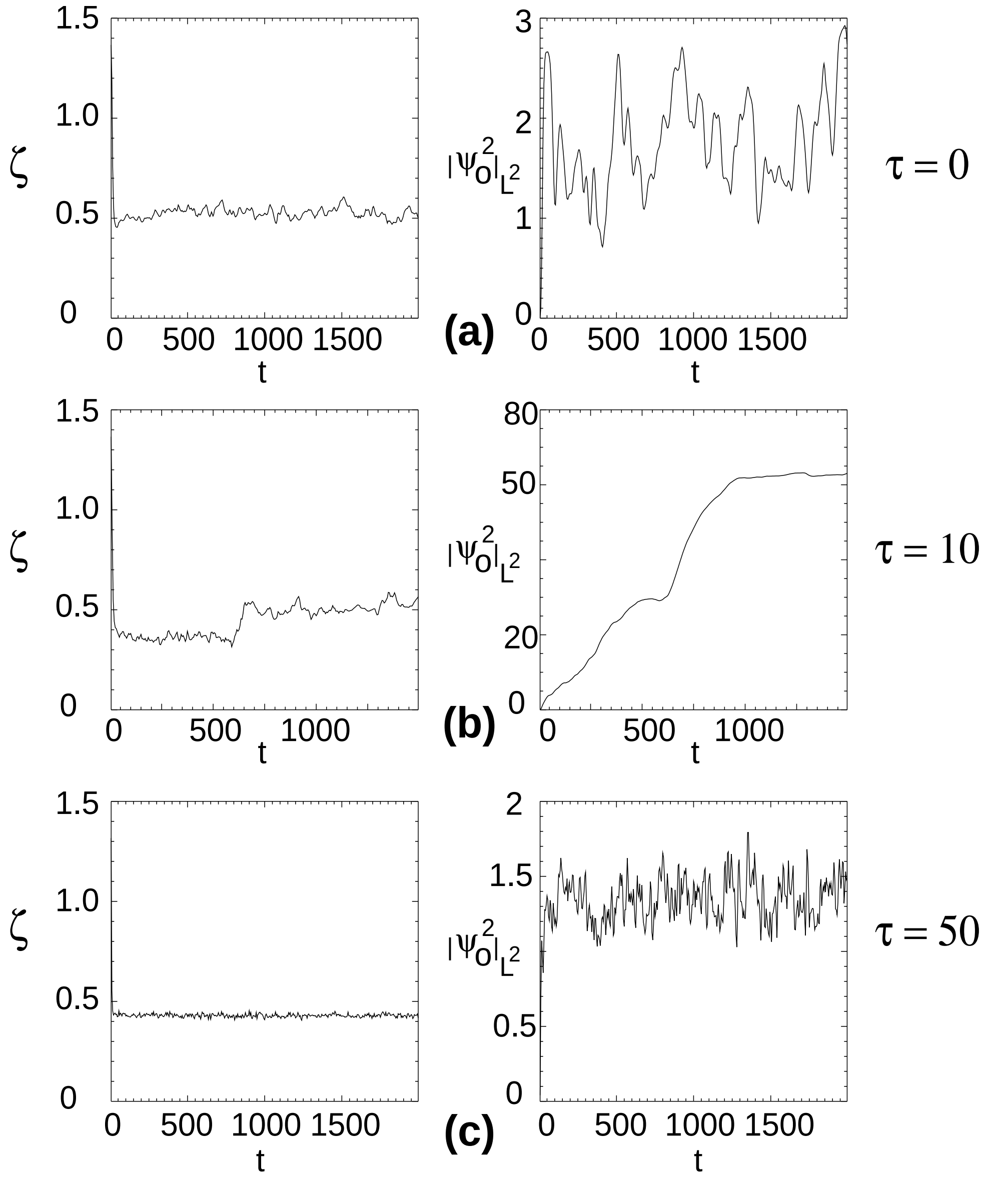

Figure 17: Time evolution of the correlation length ζ defined by eq. (106) (left) and of the L^2-norm of the mean flow stream function (right) for free-slip boundary conditions, with $P = 1.2$, $\tilde{\epsilon} = 0.7$ and rotation rates $\tau = 0$ (a), $\tau = 10$ (b) and $\tau = 50$ (c).

When analyzing the influence of the rotation rate, at fixed values of the Prandtl number ($P = 2$) and of the stress parameter ($\tilde{\epsilon} = 0.05$), we notice that the structures formed at small rotation (e.g. $\tau = 4$), are similar to those of Fig. 15a, while for larger values of τ (e.g. $\tau = 30$), the angular range of unstable modes becoming larger, the formation of coherent structures is prevented. More quantitatively, in Fig. 17, we consider for a Prandtl number $P = 1.2$ and a stress parameter $\tilde{\epsilon} = 0.7$, the time variation of the correlation length

$$\zeta = \left(\frac{\int (k - \bar{k})^2 |\hat{w}(k)|^2 \; d^2k}{\int |\hat{w}(k)|^2 \; d^2k} \right)^{-\frac{1}{2}} \tag{105}$$

where

$$\bar{k} = \frac{\int k |\hat{w}(k)|^2 \; d^2k}{\int |\hat{w}(k)|^2 \; d^2k} \; , \tag{106}$$

We observe on Fig. 17b that when targets are formed the correlation increases and so does the mean flow, as measured by the squared L_2-norm $|\psi_0|_{L_2}$ of its stream function. The dynamics is also very sensitive to the Prandtl number. With the same value of the stress parameter $\tilde{\epsilon} = 0.7$ and the same rotation rate ($\tau = 10$) but for a Prandtl number $P = 10$, straight parallel rolls are obtained when the convection cell has an aspect ratio $\Gamma = 16$, the small-angle instability being weak and the KL instability absent.

It is noticeable that the formation of stable targets is not specific to the case of periodic conditions in the horizontal directions. Such structures are also obtained in simulations performed in a cylindrical box with no-slip conditions on the side wall but free-slip top and bottom boundary conditions. In this case, the pattern adjusts to the symmetry of the container, leading to concentric rolls which occupy the whole domain [26]. In contrast, as discuss in the next section, a different dynamics develop with rigid to and bottom boundary conditions where the small-angle instability does not exist.

5 Nonlinear dynamics for rigid boundary conditions

The dynamics developing with rigid top and bottom boundaries and periodic conditions in the horizontal directions is displayed in Fig. 18, for a Prandtl number $P = 1.2$ and a stress parameter $\tilde{\epsilon} = 0.7$. In the absence of rotation (Fig. 18a), we observe the now well documented spiral turbulence [27]-[34]. The effect of a small rotation $\tau = 10$ (Fig. 18b) is to increase the size of the spirals and to force their rotating motion in the same direction as that of the external rotation [35], [36]. This last point is illustrated in Fig. 19 which displays the convective field for $\tau = -10$, 0 and +10. Up to rotation rates comparable to the critical value for the onset of the Küppers-Lortz instability, we observe a progressive "relaminarization" of the flow, characterized by the gliding and annihilation of dislocations, and leading to a highly correlated pattern in the form of quasi-parallel rolls (Fig. 18c). In the presence of lateral boundaries, this phenomenon is less conspicuous due to the continuing formation and annihilation of dislocations on the sidewalls [26]. These defects were shown to be responsible for the appearance of the Küppers-Lortz instability for rotation rates below the theoretical value for its onset [7], [8]. A maximum of the correlation length around τ_{KL} is nevertheless visible in experimental results for a large aspect ratio cell reported in Fig. 4 of [37], although the authors do not stress this point. We observe in Fig. 20 that the rotation rate (normalized by the critical rotation τ_{KL}) at which the relaminarization is most efficient, increases as the Prandtl number is reduced. Note that the quasi-straight roll patterns obtained after the relaminarization process, are still subject to the KL instability, but the value of τ being close to τ_{KL}, the patches have a size comparable to that of the container. As a result, the rolls rotate globally, keeping a high degree of correlation. In Fig. 21, we display the correlation length ζ and L_2 norm of the stream function ψ_0 for $P = 1.2$, $\tilde{\epsilon} = 0.7$ and various rotation rates $\tau = 0$, 10, 40. The striking features are (i) the decrease of the L^2 norm of the mean flow with time (although not monotonic) and (ii) the anti-correlation between ζ and $|\Psi_0|_{L_2}$, especially visible for $\tau = 40$. The gradual decrease of $|\Psi_0|_{L_2}$ for $\tau = 0$ is consistent with the formation of spirals and targets for which the mean flow is minimum. Although the system is not a gradient flow, it evolves as if it were trying to maximize the heat transport by creating structures for which the friction of the horizontal flow on the top and bottom boundaries is minimized. For non-zero rotation rates, the formation of very correlated structures (almost straight rolls) also corresponds to a minimization of the mean flow. It is noticeable that with free-slip boundaries, this tendency is exactly opposite. In the latter case, the coherent structures formed at $\tau = 10$, correspond to targets which maximize the mean flow (Fig. 17b). Finally, when the Küppers-Lortz instability is efficient, a highly chaotic regime is recovered (Fig. 18d).

We conclude this section by mentioning that a transition between spiral chaos and a stationary pattern of straight parallel roll was recently observed in convection experiments performed in the absence of rotation in a square cell with a fluid of Prandtl number one, in a range of parameters for which straight parallel rolls are stable in an infinite medium [38]. After convection in the system has been initialized by a jump from below onset ($\epsilon < 0$) to above onset ($\epsilon > 0$), formation of straight parallel rolls was observed near the sidewalls, while a random pattern appears in the middle of the cell. If ϵ is not too large, a competition between patches of spiral chaos and of straight parallel rolls develops and, in some instances, a patch of straight parallel rolls grow and fill the entire cell. This situation contrasts with experiments in cylindrical boxes where the roll tendency to align perpendicularly to the boundaries, results in roll curvature and, under the mean flow effect, to a persistent spiral chaos. In this context, the question arises whether there exits a relation between the above transition and the relaminarization observed in our rotating convection model, the enhancement of the defect motions due to rotation promoting faster relaminarization.

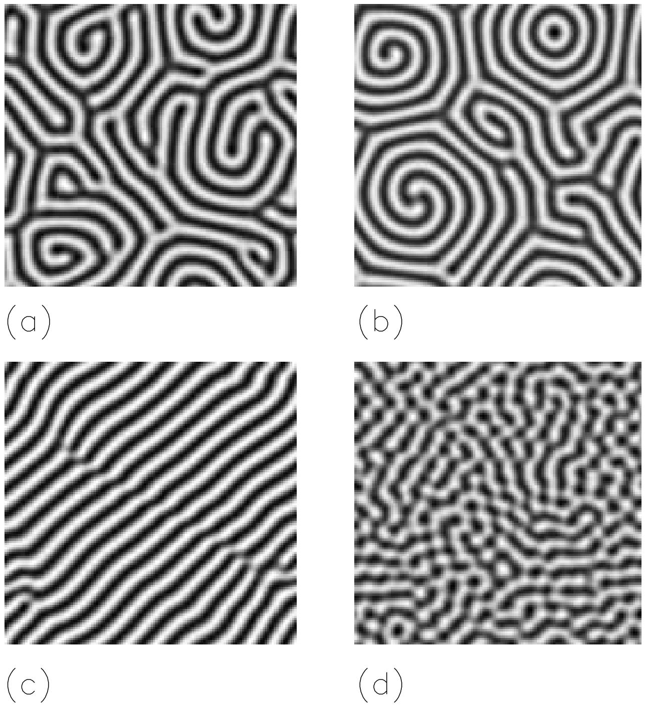

Figure 18: Convective pattern for rigid boundary conditions, with $P = 1.2$, $\tilde{\epsilon} = 0.7$ and $\tau = 0$ (a), $\tau = 10$ (b), $\tau = 40$ (c) and $\tau = 56$ (d).

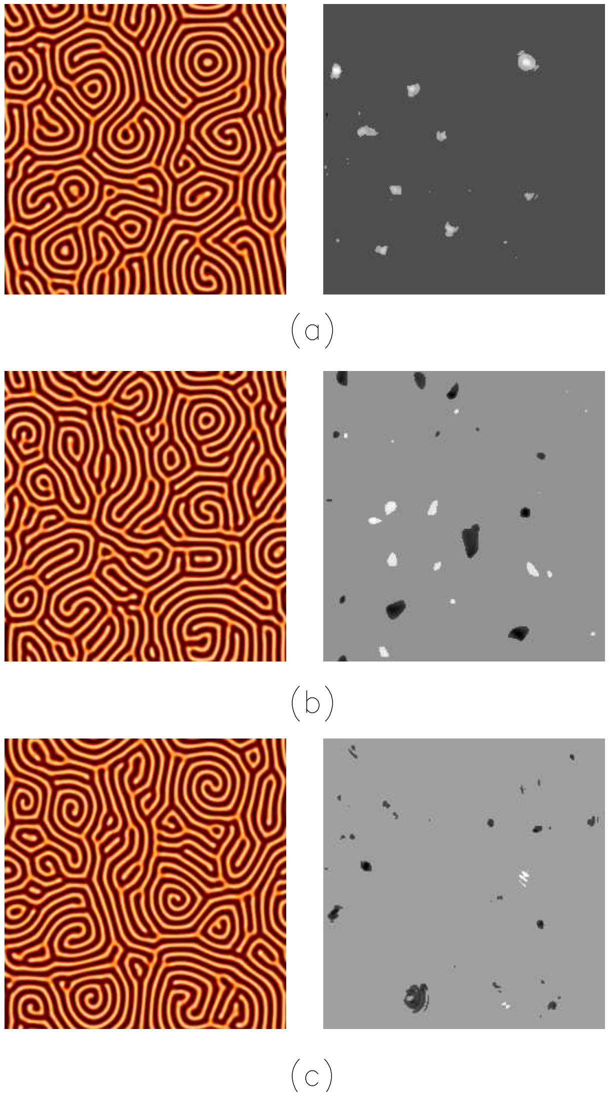

(a)

(b)

(c)

Figure 19: Convective pattern (left) and mean flow stream function filtered by the condition $|\Psi| > \sup|\Psi|/3$ (right) for rigid boundary conditions, $P = 1.2$, $\tilde{\epsilon} = 0.7$ and $\tau = 10$ (a), $\tau = 0$ (b) or $\tau = -10$ (c), showing positive or negative vortex cores according to the sign of τ.

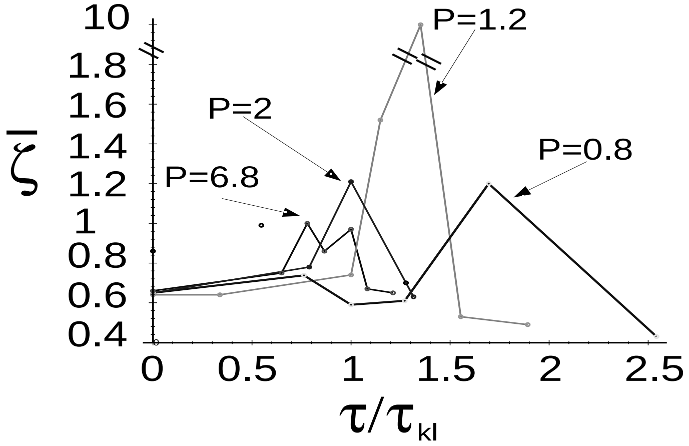

Figure 20: Time average of the correlation length $\bar{\zeta}$ versus the rotation rate τ normalized by the critical value τ_{KL} for onset of the Küppers-Lortz instability, for different Prandtl numbers.

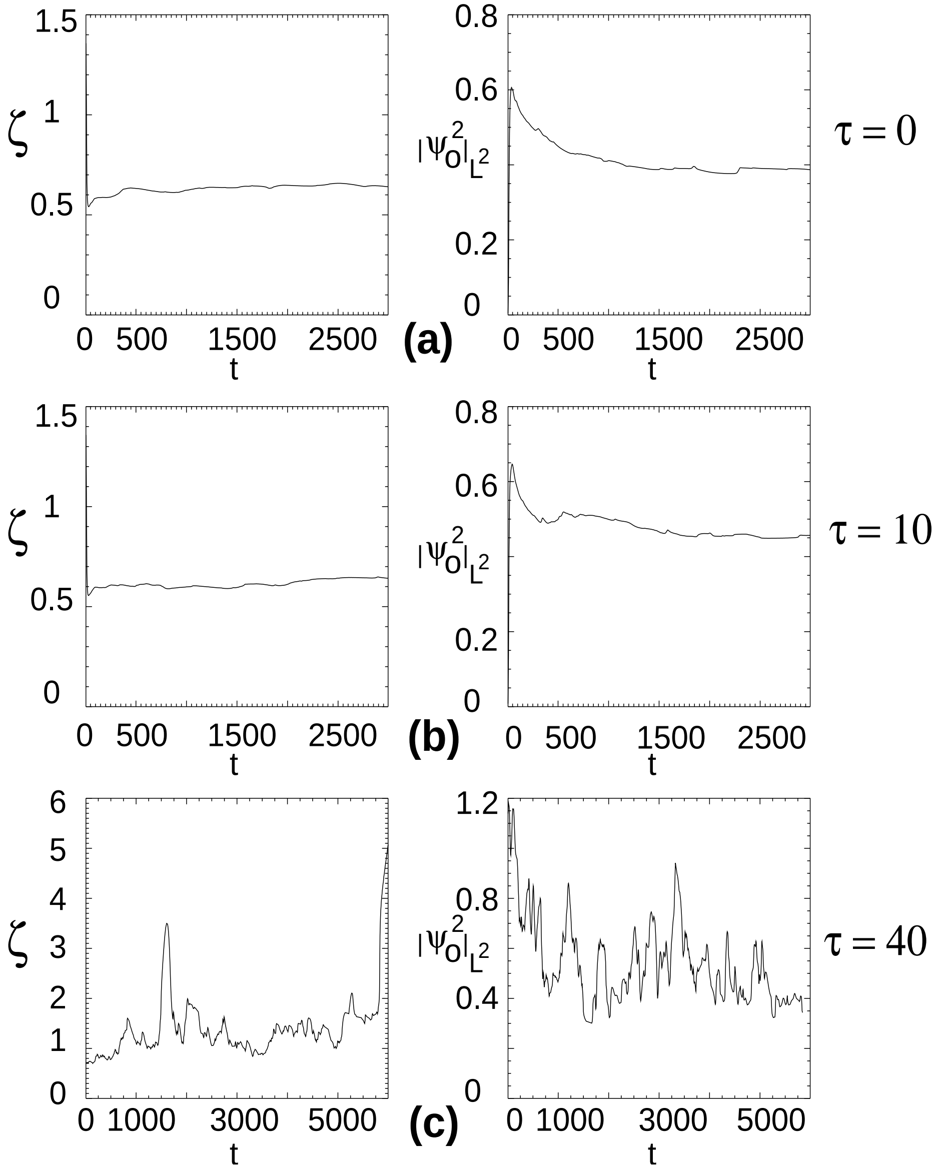

Figure 21: Time evolution of the correlation length ζ (left) and of the squared L^2-norm of the mean flow stream function (right) for rigid boundary conditions, $P = 1.2$, $\tilde{\epsilon} = 0.7$, and different rotation rates $\tau = 0$ (a), $\tau = 10$ (b) and $\tau = 40$ (c).

6 Summary

A Swift-Hohenberg-type model was derived for rotating convection at finite Prandtl number with free-slip or rigid boundary conditions. Rotation is shown to reduce the friction coefficient of the mean flow on the rigid top and bottom boundaries, and the nonlinear couplings are adjusted in such a way as to accurately reproduce both the zig-zag and the Küppers-Lortz instabilities. Numerical integration in the case of a periodic horizontal geometry points out the relaminarization effect of a moderate rotation which counterbalances the destabilizing influence of the mean flow. It is mostly a consequence of the enhanced gliding of the dislocations which in periodic geometries, can totally annihilate each other. With rigid boundaries, this leads to the reformation of straight parallel rolls, while in the case of free-slip boundary conditions, these structures, destabilized by the small-angle instability, evolve towards big coherent targets embedded in small-scale turbulence.

Numerical simulations were performed on the CRAY-C98 of IDRIS, Palaiseau. This work benefited from partial support by the European Cooperative Network ERBC HRXCT930410.

[1] M.C. Cross and P.C. Hohenberg, “Spatio-temporal chaos”, Science **263**, 1569 (1994).

[2] G. Küppers and D. Lortz, “Transition from laminar convection to thermal turbulence in a rotating fluid layer”, J. Fluid Mech. **35**, 609 (1969).

[3] R.M Clever and F.H Busse, ”Nonlinear properties of convection rolls in a horizontal layer rotating about a vertical axis” J.Fluid Mech. **94**, 609 (1979).

[4] G. Küppers, “The stability of steady finite amplitude convection in a rotating fluid layer”, Phys. Lett. **32 A**, 7 (1970).

[5] T. Clune and E. Knobloch, “Pattern selection in rotating convection with experimental boundary conditions”, Phys. Rev. E **47**, 2536 (1993).

[6] Y. Ponty, T. Passot and P.L. Sulem, “A new instability for finite Prandtl number rotating convection with free-slip boundary conditions”, Phys. Fluid. **9**, 67 (1997).

[7] F. Zhong, R. Ecke and V. Steinberg, “Rotating Rayleigh-Bénard convection; The Küppers-Lortz transition”, Physica D **51**, 596 (1991).

[8] J. Millán-Rodríguez and C. Pérez-García, “Motion of defects in rotating fluid”, Chaos, **4**, 369 (1994).

[9] Y. Hu, R.E. Ecke and G. Ahlers, “Convection under rotation for Prandtl number near on: Part I. Linear stability, wavenumber selection, and pattern dynamics”, preprint 1997.

[10] M. Neufeld, R. Friedrich and H Haken, “Order parameter equation and equation for high Prandtl number. Rayleigh-bénard convection in a rotating aspect ratio system”, Z. Phys. **B 92**, 243 (1993);

[11] M. Fantz, R. Friedrich, M. Bestehorn and H. Haken, “Pattern formation in Bénard convection”, Physica D **61**, 147 (1992).

[12] J. Millán Rodríguez, C. Pérez-García, M. Bestehorn, M. Fantz and R. Friedrich, “Pattern formation in convection of rotating fluids with broken vertical symmetry”, Phys. Rev. A **46** 4729 (1992).

[13] S. Chandrasekhar, *Hydrodynamic and Hydromagnetic Stability*, Oxford University Press (1961).

[14] Hao-wen Xi, J. D. Gunton and G. A. Markish, “Pattern formation in the rotating fluid: Küppers-Lortz instability” Physica A **204**, 741 (1994).

[15] F. H. Busse and E. W. Bolton, “Instabilities of convection rolls with stress-free boundaries near threshold”, J. Fluid Mech. **146**, 115 (1984).

[16] A. Zippelius and E. D. Siggia, ”Stability of finite-amplitude convection”, Phys. Fluid **26**, 2905 (1983).

[17] P. Manneville, ”A two-dimensional model for three-dimensional convective patterns in wide containers” J. Phys. (France) **44**, 759 (1983); “Toward an understanding of weak turbulence close to the convection threshold in large aspect ratio system” *J. Phys. (France)* **44**, 903 (1983).

[18] A.J. Roberts, “The Swift-Hohenberg equation requires non-local modifications to model spatial pattern evolution of physical problems”, J. Austral. Math. Soc. Ser. B **34**, 174 (1992).

[19] H.S Greenside and M.C. Cross, ”Stability analysis of two-dimensional models of three-dimensional convection”, Phys. Rev. A **41**, 2492 (1985).

[20] Hao-wen Xi and J.D. Gunton, ”Spatio-temporal chaos in a model of Rayleigh-Bénard convection”, Phys. Rev. E **52**, 4963 (1995).

[21] A.C. Newell, T. Passot and M. Souli, “The Phase diffusion and mean drift equations for convection at finite Rayleigh numbers in large containers”, J. Fluid. Mech. **220**, 187 (1990).

[22] M. C. Cross and A. C. Newell, “Convection pattern in large aspect ratio systems”, Physica D **10**, 299 (1984).

[23] A.C. Newell, T. Passot, N. Ercolani and R. Indik, “Elementary and Composite Defects of Striped Patterns” J. Phys. II (France) **5**, 1863 (1995).

[24] F.H. Busse and K.E. Heikes, “Convection in a rotating layer: a simple case of turbulence”, Science **208**, 173 (1980).

[25] M.C. Cross, D. Meiron and Y. Tu, ”Chaotic domain: A numerical investigation”, Chaos **4**, 607 (1994).

[26] Y. Ponty, T. Passot and P.L. Sulem, “ Chaos and structures in rotating convection at finite Prandtl number”, Phys. Rev. Lett. **79**, no 1, 7 July 1997 (in press).

[27] H. Xi, J.D. Gunton & J. Viñals, Phys. Rev. Lett. **71**, 2030(1993).

[28] Morris, S.W., Bodenschatz, E., Cannell D.S. and Ahlers, G., Phys. Rev. Lett. **71**, 2026 (1993).

[29] W. Decker, W. Pesch and A. Weber, “Spiral defect chaos in Rayleigh-Bénard convection”, Phys. Rev. Lett. **73**, 648 (1994).

[30] Y. Hu, R. Ecke and G. Ahlers, “Transition to spiral defect chaos in low Prandtl number convection”, Phys. Rev. Lett. **74**, 391 (1995).

[31] Y. Hu, R. Ecke and G. Ahlers, Phys. Rev. E **51**, 3263 (1995).

[32] M. Assenheimer and V. Steinberg, Transition between spiral and target states in Rayleigh-Bénard convection, Nature **367**, 345 (1994).

[33] S.W. Morris, E. Bodenschatz, D.S Cannell and G. Ahlers, “The spatio-temporal structure of spiral-defect chaos”, Physica D **97**, 164 (1996).

[34] M. Cross, Physica D, **97**, 65 (1996).

[35] R.E. Ecke, Y. Hu, R. Mainieri and G. Ahlers, ”Excitation of Spirals and Chiral Symmetry Breaking in Rayleigh-Bénard Convection”, Science **269**, 1704 (1995).

[36] W. Pesch, ”Complex spatio-temporal convection pattern”, Chaos **6**, 348 (1996).

[37] Y. Hu, R. Ecke and G. Ahlers, “ Time and Length scales in rotating Rayleigh-Bénard Convection”, Phys. Rev. Lett. **74**, 5040 (1995).

[38] R.V. Cakmur, D.A. Egolf, B.P. Plapp and E. Brodenschatz, “Transition from spatiotemporal chaos to ideal straight rolls in Rayleigh-Bénard convection”, preprint 1997.

Chaos and structures in rotating convection at finite Prandtl number

Y. Ponty[1], T. Passot[1,2] and P.L. Sulem[1],
[1] CNRS, UMR 6529, Observatoire de la Côte d'Azur
B.P. 4229 06304 Nice cedex 4, France.
[2] Arizona Center for Mathematical Sciences,
Department of Mathematics, University of Arizona, Tucson, AZ, 85721, USA.

Phys. Rev. lett. **79**, *juillet 1997.*

Abstract

It is shown, using a generalized Swift-Hohenberg equation, that a small rotation inhibits the spiral chaos which develops in Rayleigh-Bénard convection at moderate Prandtl number. This is due to the gliding and gradual annihilation of dislocations. For rigid top and bottom boundary conditions, a slow rotation first breaks the chiral symmetry and if sufficient leads to an unfolding of the spirals.This effect is maximum near the critical rotation for the onset of the Küppers-Lortz instability, and when the horizontal geometry is periodic, straight rolls may even reform. With free-slip boundaries, these structures are subject to a small-angle instability, which leads to the formation of large coherent targets embedded in a turbulence background.

PACS numbers: 47.27.Te, 47.20.Lz, 47.52.+j, 47.54.+r

Thermal convection in a Boussinesq fluid with high Prandtl number P, rotating around a vertical axis is known to develop spatio-temporal chaos, when the Taylor number $T_a = \tau^2$ is larger than a critical value [1]. This dynamics results from the Küppers-Lortz (KL) instability [2, 3] which destabilizes straight parallel rolls as soon as the Rayleigh number R exceeds the convection threshold R_c. It leads to the formation of patches of straight rolls penetrating each other in a chaotic way : rolls disappear and are replaced by other rolls tilted by an angle θ_{KL} close to 58 degrees.

At moderate Prandtl number (assuming $P > 0.67$ to avoid over-stability), the KL instability survives, but the angle θ_{KL} associated to the most unstable mode decreases with the Prandtl number, both for rigid [4, 5] and free-slip top and bottom boundaries [6]. In the latter case (often used in the context of astro and geophysical flows), the usual perturbation method used to analyze the KL instability near convection threshold leads to a divergence in the small angle limit [5]. This reflects the existence of an additional and stronger instability present in a small-angle boundary layer [6]. This "small-angle instability" develops whatever the value of the rotation rate and can be viewed as the continuation of the skewed-varicose instability which destabilizes critical rolls near onset in the absence of rotation [7]. At small enough Prandtl number (below $P \approx 5$), the KL and the small-angle instabilities cannot be separated as a result of the decrease of θ_{KL} and the enhancement of the unstable small-angle range when P is reduced.

Whereas for infinite Prandtl number, the KL dynamics can be qualitatively reproduced by a set of three amplitude equations [8], the description of the dynamics at moderate Prandtl numbers, where θ_{KL} is significantly smaller than 60^o ($\theta_{KL} = 38.4^o$ for $P = 0.8$), requires Swift-Hohenberg (SH) type equations reproducing the correct variation of the KL instability with the Prandtl number. Such a model was recently derived by a perturbation expansion near threshold [9]. In the case of free-slip top and bottom boundaries, it is obtained by a simplification of a systematically derived set of equations for the leading vertical velocity mode W and the (horizontal) mean flow potential Ψ. In the case of no-slip boundaries, the mean flow equation together with the linear part of the equation for the convective mode are exactly derived by projection of the mean flow on the vertical mode $\sin \pi z$ $(0 < z < 1)$ and of the vertical velocity on the first eigenmode of the fourth derivative operator with appropriate boundary conditions [10]. The nonlinear couplings arising in the equation for W are selected among those present in the free-slip case, with coefficients adjusted in such a way that the correct boundary of the zig-zag instability in the absence of rotation, and the right critical rotation and most unstable angle θ_{KL} for the KL instability be reproduced. Denoting by ϵ the normalized distance from threshold, the system reads

$$\tau_0 \partial_t W = (\epsilon - (\Delta + 1)^2) W - \mathcal{N}(W, \Psi) \tag{1}$$

$$\begin{aligned}&(\partial_t - P(\nu + \Delta))\Delta\Psi = (\nabla \Delta W \times \nabla W) \cdot \hat{\mathbf{z}} \\ &+\alpha_6[(\Delta W)^2 + \nabla W \cdot \nabla \Delta W] + \alpha_7 \Delta(W^2)\end{aligned} \tag{2}$$

with $\mathcal{M} = W^2 + |\nabla W|^2$ and

$$\begin{aligned}\mathcal{N}(W,\Psi) &= \mathcal{M}W + \alpha_1 \nabla W \cdot \nabla \mathcal{M} + \alpha_2 (\nabla W \times \nabla \mathcal{M}) \cdot \hat{\mathbf{z}} \\ &\quad \alpha_3 (\nabla W \times \nabla \Psi) \cdot \hat{\mathbf{z}} + \alpha_4 W \Delta \Psi + \alpha_5 \nabla W \cdot \nabla \Delta \Psi.\end{aligned}$$

In the case of free-slip boundaries, $\nu = \alpha_7 = 0$. Moreover, in the absence of rotation, the coefficients α_2, α_4, α_5 and α_6 vanish, and the model generalizes the equations obtained by Manneville [11] by the inclusion of an additional coupling. For rigid boundaries, $\alpha_4 = \alpha_5 = 0$. Furthermore, the friction coefficient ν is found to be $\nu = \pi^2/q_c^2$ (where q_c denotes the critical wavenumber) and thus decreases as the rotation rate is increased. Note the presence of the additional term $\alpha_7 \Delta(W^2)$ in the mean flow equation, originating from the vertical Reynolds stress. A related, although less elaborated model was independently presented in [12].

Because of the small-angle instability arising at moderate Prandtl number when free-slip boundary conditions are prescribed, the nonlinear dynamics developing in this case is expected to be significantly different from that obtained with rigid boundaries, and the two situations are to be discussed separately.

In the simpler case of no-slip boundaries, simulations were performed both in a periodic geometry and in a cylindrical box, a configuration best suited for comparison with laboratory experiments. In the periodic case, we used a standard Fourier pseudo-spectral method with resolutions of 128^2 or 256^2 collocation points, according to the aspect ratio Γ which measures the number of rolls in the convection cell. In the presence of lateral boundaries, compact finite differences were used in the radial direction and a Fourier decomposition performed for the angular variable, with a resolution of 91×240 grid points for about 16 rolls within the box. To avoid the constraint of very small time steps, the unnecessary high resolution near the center of the box was reduced by retaining a number of nonzero angular Fourier modes decreasing with the distance to the center. A random noise with a spectrum localized in an annulus centered around the critical wavenumber was used as initial conditions.

We first report on the case of a periodic geometry. In the absence of rotation, for a moderate value of the Prandtl number ($P = 1.2$) and a large enough value of the stress parameter ($\epsilon = 0.7$), the now well documented spiral turbulence state [13, 14, 15, 16, 17, 18, 19] develops. The mean flow, resulting from roll curvature gradients, consists mostly in large-scale circulation between the structures. Vanishing exactly for perfect targets, it is small in the center of the spirals that it advects in clockwise or anti-clockwise rotating motions, depending on the sign of the dislocation imprisoned in the center of the structure.

As seen in Fig. 1, with a small rotation, spirals rotating in the direction of the external

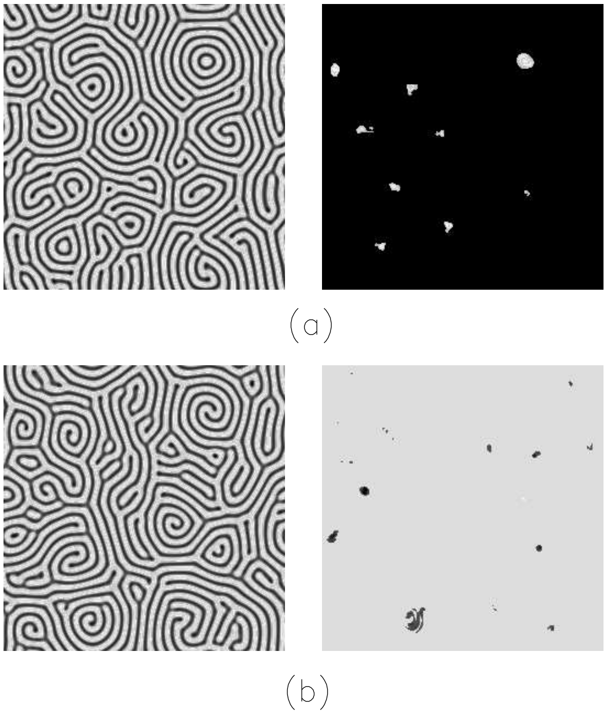

Figure 22: Convective pattern (left) and mean flow (right) filtered by the condition $|\Psi| > \sup|\Psi|/3$ for rigid boundary conditions, $P = 1.2$, $\epsilon = 0.7$ and $\tau = 10$ (a) or $\tau = -10$ (b) showing positive and negative vortices according to sign(τ).

rotation are progressively selected, like in the laboratory experiments [20]. This effect is due to the formation of vorticity patches in the center of targets and spirals, whose sign is that of the rotation, as can be seen from the mean flow equation.

As the Rossby number is increased, the spirals grow in size while their number is reduced (Figs. 2a, b). Near a critical value τ_c, the pattern evolves to almost straight rolls swept by gliding dislocations (Fig. 2c) which gradually annihilate by collisions (see also [21]). An analysis of the defect dynamics in the infinite Prandtl number limit is presented in [22]. The ratio τ_c/τ_{KL}, (where τ_{KL} denotes the critical rotation for the onset of the Küppers-Lortz instability) grows as the Prandtl number decreases. Its value is close to unity for Prandtl numbers exceeding a few units and approaches 2 for $P = 0.8$. When the rotation rate is larger than τ_c, the KL instability is sufficient to destabilize the structure and leads to the usual spatio-temporal chaotic dynamics governed by the propagation of dislocation arrays separating randomly oriented roll patches (Fig. 2d) whose size decreases as ϵ increases [23]-[25].

In order to quantitatively characterize the relaminarization effect of a moderate rotation, we have considered the correlation length $\bar{\zeta}$, defined as the time average of $\zeta =$

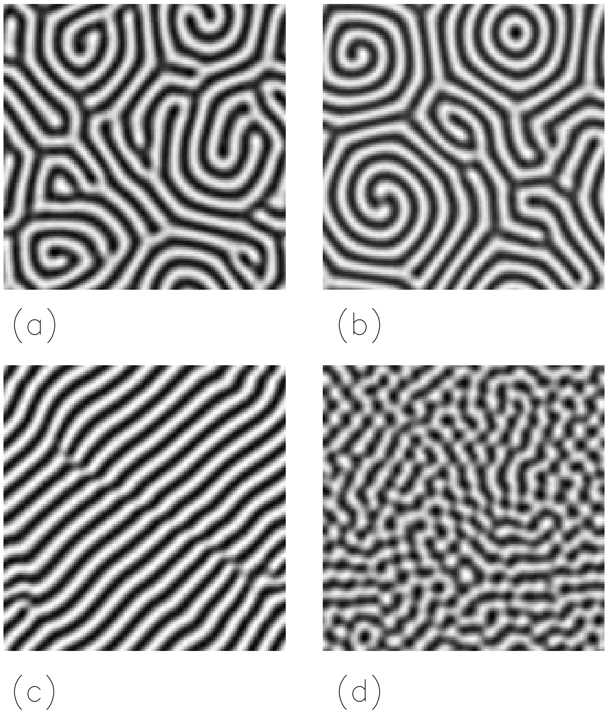

Figure 23: Convective pattern for rigid boundary conditions at $P = 1.2$, $\epsilon = 0.7$ and rotation rates $\tau = 0$ (a), $\tau = 10$ (b), $\tau = 40$ (c) and $\tau = 56$ (d), to be compared to $\tau_{KL} = 29.6$.

$(\langle k^2\rangle - \langle k\rangle^2)^{-1/2}$ where $\langle u\rangle$ stands for $\int u|\hat{W}(\vec{k})|^2 d^2\vec{k}/\int|\hat{W}(\vec{k})|^2 d^2\vec{k}$, and where $\hat{W}$ denotes the horizontal Fourier transform of the convective mode. Figure 3 displays the variation of $\bar{\zeta}$ with τ/τ_{KL} for different values of the Prandtl number. The relaminarization effect at small Prandtl number is clearly visible as a sharp maximum of the correlation length. This effect is also visible in experimental results reported in Fig. 4 of ref. [26], although the authors do not stress this point. The maximum correlation occurs near τ_{KL} for Prandtl numbers larger than unity, but is associated to faster rotations when the Prandtl number is reduced. This indicates that rotation and mean flow act in opposite direction.

In a cylindrical geometry, the dislocations cannot annihilate each other as efficiently as in the periodic case. As a result, although the patterns obtained for intermediate values of the rotation rate (Fig. 4b) still present a higher degree of correlation than in the absence of rotation, they do not reduce to straight rolls. A noticeable feature is also that the patterns globally rotate (even when the rotation rate is smaller than $\tau_{KL} = 23.6$ for $P = 0.8$), under the effect of dislocations generated on the boundary, an effect already noticed in laboratory experiments [27]. For $\tau > \tau_{KL}$, the rolls tend to break under the effect of shear layers developed by the mean flow (Figs. 4c, d).

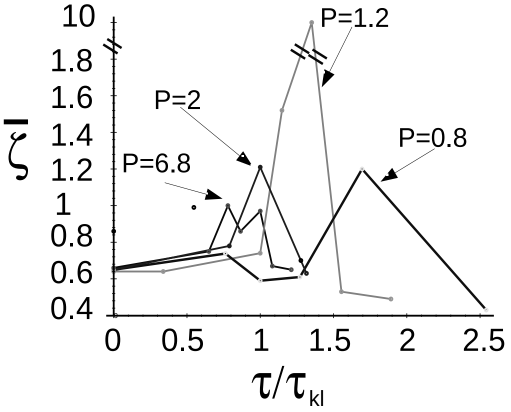

Figure 24: Variation of the correlation length ζ with τ/τ_{KL}, for different values of the Prandtl number.

In the case of free-slip boundary conditions, the above dynamics is affected by the presence of the small-angle instability which is accurately reproduced when the three terms involving Ψ in $\mathcal{N}(W, \Psi)$ are retained. In the weakly nonlinear regime, the effect of this instability is to gradually rotate the convective rolls through reconnections of dislocations produced by the shearing motion of the mean flow.

In the fully nonlinear regime at moderate Prandtl number ($\epsilon = 0.5$, $P = 2$), the dynamics is significantly different from that obtained with rigid boundaries. In the absence of rotation, targets and spirals still form (Fig. 5a) but their coherence time is much shorter. The evolution is strikingly similar to that observed in laboratory experiments performed at very large aspect ratio [14]. In both situations, the target formation is initiated by a defect instability, leading to "roll bulging, pinching and bridging" [28]. This suggests that the strength of the mean flow (which is weaker with rigid than with no-slip boundaries) can in fact be enhanced by increasing the aspect ratio of the container. With a small rotation ($\tau = 10$), targets of moderate size (Fig. 5b), associated to patches of positive vorticity for the mean flow, are rapidly formed. They subsequently grow by accreting adjacent rolls and by merging together, leading to a unique coherent structure occupying the whole domain. At a larger value of the rotation rate ($\tau = 20$), the dynamics displays an early chaotic phase followed by the emergence of almost straight rolls, visible in the upper half of Fig. 5c. Under the action of the small-angle instability, this structure, similar to that observed in the case of no-slip boundaries, is destabilized. It bends and progressively evolves towards big targets embedded in a chaotic background and displayed in Fig. 5d. In the case of a cylindrical box, the pattern adjusts to the symmetry of the container, leading to concentric rolls which occupy the whole domain. The formation of

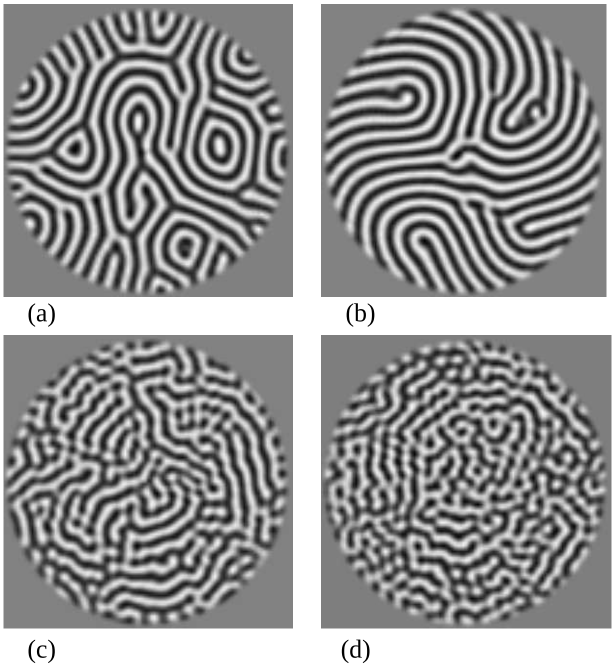

Figure 25: Convective pattern in cylindrical geometry for $P = 0.8$, $\epsilon = 0.7$, and $\tau = 0$ (a), $\tau = 18$ (b), $\tau = 40$ (c), $\tau = 60$ (d).

these coherent targets is consistent with the continuous rotation symmetry of the small-angle instability. For $\tau = 60$, the dynamics is dominated by the Küppers-Lortz instability. The coherent structures are destroyed and a fully chaotic regime develops. Similarly, when at moderate rotation ($\tau = 10$) the Prandtl number is increased, the coherent targets formed at small values of the rotation rate, become transients at $P = 6.8$, and totally disappear at $P = 50$.

Although with free-slip boundaries, the system develops strong coherent structures, the correlation length displayed in Fig. 6 is significantly different from that obtained with rigid boundaries. It does not display a maximum, because of the presence of a fully-turbulent background . Furthermore, the destabilizing effect of the mean flow is clearly reflected by the growth of the correlation length with the Prandtl number, an effect emphasized by the free-slip boundaries.

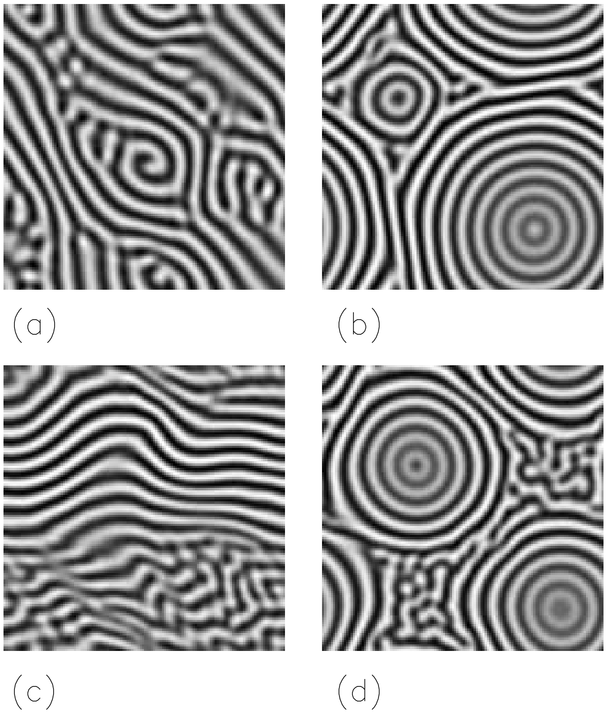

Figure 26: Convective pattern for free-slip boundary conditions at $P = 2$, $\epsilon = 0.5$, with rotation rates $\tau = 0$ (a), $\tau = 10$ (b) and $\tau = 20$ taken at two different times (c,d).

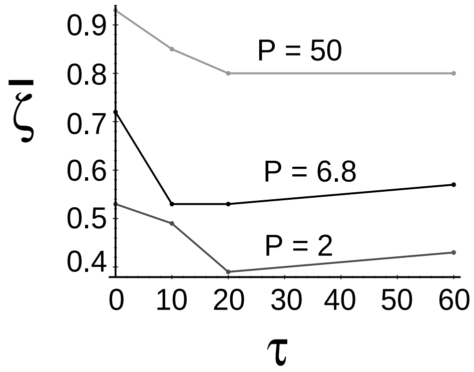

Figure 27: Variation of the correlation length ξ with τ in the case of free-slip boundaries for different Prandtl numbers.

acknowledgments T.P. acknowledges the hospitality of the Arizona Center for Mathematical Sciences. Part of this work has been supported by contract AFOSRF49620-94-1-0463 and by the European Cooperative Network ERBC HRXCT930410. Numerical simulations were performed on the CRAY-C98 of IDRIS, Palaiseau.

[1] F.H. Busse and K.E. Heikes, Science **208**, 173 (1980).

[2] G. Küppers and D. Lortz, J. Fluid Mech. **35**, **3**, 609 (1969).

[3] R.M Clever and F.H Busse, J.Fluid Mech. **94**, 609 (1979).

[4] G. Küppers, Phys. Lett. **32 A**, 7 (1970).

[5] T. Clune and E. Knobloch Phys. Rev. E **47**, 2536 (1993).

[6] Y. Ponty, T. Passot and P.L. Sulem, Phys. Fluids. **9**, 67 (1997).

[7] F. H. Busse and E. W. Bolton, J. Fluid Mech. **146**, 115, (1984).

[8] Y. Tu and M.C. Cross, Phys. Rev. Lett., **69**, 2515-2518. (199)

[9] Y. Ponty, T. Passot and P.L. Sulem, "Pattern dynamics in rotating convection at finite Prandtl number" , Phys. Rev. E. (in press).

[10] S. Chandrasekhar. "Hydrodynamic and hydromagnetic stability" *Oxford University Press* (1961).

[11] P. Manneville, J. Phys. (France) **44**, 759 (1983).

[12] Haowen. Xi, J. D. Gunton and G. A. Markish, Physica A, **204**, 741-754, (1994).

[13] Morris, S.W., Bodenschatz, E., Cannell D.S. and Ahlers, G., Phys. Rev. Lett. **71**, 2026 (1993).

[14] M. Assenheimer and V. Steinberg, Phys. Rev. Lett. **70**, 3888 (1993).

[15] W. Decker, W. Pesch and A. Weber, Phys. Rev. Lett **73**, 648 (1994).

[16] Y. Hu, R. Ecke and G. Ahlers, Phys. Rev. E **51**, 3263 (1995).

[17] J. Liu and G. Ahlers, Phys. Rev. Lett. **77**, 3126 (1996).

[18] M. Cross, Physica D bf 97, 65 (1996).

[19] Haowen Xi and J.D. Gunton, Phys. Rev. E **52**, **5**, 4963 (1995).

[20] R.E. Ecke, Y. Hu, R. Mainieri and G. Ahlers, Science **269**, 1704-1707 (1995).

[21] J. Millán- Rodríguez, M. Bestehorn, C. Pérez-García, and R. Friedrich , Phys. Rev. Lett, **74**, 530 (1995).

[22] J. Millán- Rodríguez and C. Pérez-García, Chaos, **4**, 369 (1994).

[23] M. Neufeld, R. Friedrich and H Haken, Z. Phys. **B 92**, 243 (1993).

[24] M. Fantz, R. Friedrich, M. Bestehorn and H. Haken, Physica D **61** , 147 (1992).

[25] M.C. Cross, D. Meiron and Y. Tu, Chaos **4**, 607 (1994).

[26] Y. Hu, R.E. Ecke, and G. Ahlers, Phys. Rev. Lett. **74**, 5040 (1995).

[27] F. Zong, R. Ecke and V. Steinberg, Physica D **51**, 596 (1991).

[28] M. Assenheimer and V. Steinberg, Nature **367**, 345 (1994).

Partie II

Effet dynamo dans un écoulement chaotique

Chapitre A

Introduction

La théorie de l'effet dynamo est apparue avec le désir croissant de comprendre l'origine du champ magnétique d'objets célestes. Larmor (1919) fut le premier à suggérer l'existence d'un effet dynamo responsable du champ magnétique du Soleil. Le but est d'expliquer l'apparition et la persistance du champ magnétique comme résultant de mouvements de fluides conducteurs. Les équations de la magnétohydrodynamique couplent les mouvements des particules fluides chargées électriquement et le champ magnétique du millieu. Les interactions non linéaires des deux champs couplés peuvent produire une amplification du champ magnétique, appelé effet dynamo. Deux sortes d'effet dynamo sont distinguées aujourd'hui, la dynamo rapide qui persiste à fort nombre de Reynolds magnétique et la dynamo lente qui disparaît à faible diffusivité magnétique. La recherche du mécanisme de dynamo rapide est motivée par la présence de très grandes valeurs du nombre de Reynolds magnétique en astrophysique et en géophysique (10^3 à 10^{10}). Si les premièrs travaux ont montré l'importance de l'hélicité cinétique (Parker (1955) [19], Steebeck et al (1966) [21]) pour la génération d'un champ magnétique à grande échelle, ce n'est que plus récemment que le rôle du chaos a été mis en en lumière pour ce qui est de la dynamo à petite échelle. C'est à cette dernière que l'on va s'intéresser maintenant.

1 Dynamo cinématique

Une approche simplifiée du phénomène de la génération de champ magnétique est l'étude de la dynamo cinématique qui néglige la réaction du champ magnétique sur l'écoulement.

De nombreux écoulements ont été étudiés, de manière théorique et numérique [1]. On peut distinguer trois types d'écoulements, les écoulements bidimensionnels instationnaires (Otani (1988, 1993) [16], Galloway et Proctor (1992) [10] et Hollerbach, Galloway et

Proctor (1995) [11]) et les écoulements tridimensionnels stationnaires ou instationnaires (Arnold et Korkina (1983) [2], Galloway et Frisch (1986) [9] et Soward (1987) [22]). Il faut noter que les écoulements bidimensionnels mentionnés précédemment ne dépendent que de deux variables spatiales, mais présentent une dépendance temporelle oscillante. En effet, le théorème anti-dynamo montre l'impossibilité d'obtenir une dynamo pour un pur écoulement bidimensionnel stationnaire.

Une conjecture due à Arnold stipule qu'une dynamique chaotique de l'écoulement est nécessaire pour engendrer une dynamo rapide. Des mesures sur un flot chaotique, comme l'entropie topologique et le plus grand des exposants de Lyapunov, sont des bornes supérieures possibles pour le taux de croissance exponentiel de la dynamo. Cette conjecture de Finn et Ott (1988) [7] a été vérifiée dans de nombreux exemples numériques et démontrée par Vishik (1992) [25] et Klapper et Young (1995) [13]. Des modèles sous la forme d'écoulement discret (mapping) ont permis de trouver des exemples de dynamo rapide (Bayly et Childress (1988) [3], Finn et Ott (1988) [7], Gilbert (1992) [12] et Oseledets (1993) [15]).

La distinction entre dynamo rapide et lente a été mise en avant par Vainshtein et Zeldovich (1972) [24] avec un modèle élémentaire produisant un mécanisme qui double le flux magnétique, le "stretch-twist-fold", Alfvèn d'ailleurs présentait un modèle équivalent en 1950. Ce mécanisme, maintenant appelé modèle AVZ (Alfvèn-Vainshtein-Zeldovich), étire les tubes de flux magnétique, vrille les tubes en deux parties qui vont ensuite se replier pour donner le double du flux (voir Childress (1992) [4] pour une récente mise à jour).

Ce simple mécanisme montre l'importance de la présence de zones d'étirement et d'hélicité dans l'écoulement.

De ce fait, l'écoulement ABC est un bon candidat pour réaliser une dynamo rapide.

$$\vec{u}_{ABC} = \begin{bmatrix} Asinz + Ccosy \\ Bsinx + Acosz \\ Csiny + Bcosx \end{bmatrix} \tag{1}$$

L'écoulement ABC (Arnold-Beltrami-Childress), formé de trois ondes de Beltrami (où la vitesse et la vorticité sont parallèles en tout point) a d'abord été étudié dans un contexte de dynamo α (Childress (1970)), puis utilisé dans la recherche de dynamo rapide par Galloway et Frisch (1984, 1986) [9] et Lau et Finn [14] (1993). Cet écoulement comporte des îlots intégrables, des zones chaotiques et des points de stagnation instables (Arnold (1965), Hénon (1966) et Dombre et al (1986) [5]). Galloway et Frisch (1984, 1986) et Galanti, Pouquet et Sulem (1993) [8] ont remarqué que la localisation des structures magnétiques s'effectue autour de ces points fixes, qui sont connectés par des orbites hétéroclines. Différents types de points de stagnation ont été identifiés, autour desquels le champ magnétique se concentre en structures ayant la dimension des variétés instables des points hyperboliques.

2 Dynamo dans un écoulement $2D\frac{1}{2}$

L'étude d'écoulements stationnaires tridimensionnels ne permettait pas numériquement de dépasser des nombres de Reynolds magnétique de l'ordre du millier. On peut cependant utiliser un écoulement bidimensionnel perturbé temporellement; Galloway et Proctor (1992) [10] ont trouvé un cas de dynamo rapide pour des nombres de Reynols magnétique de l'ordre 10^4, utilisant l'écoulement de Roberts (1972) [20] pertubé temporellement, appelé écoulement "CP+ϵ".

$$\vec{u}_{CP+\epsilon} = \begin{bmatrix} a\sin[z+\epsilon\sin(\omega t)] + \cos[y+\epsilon\cos(\omega t)] \\ acos[z+\epsilon\sin(\omega t)] \\ \sin[y+\epsilon\cos(\Omega t)] \end{bmatrix} \tag{2}$$

avec dans le cas de Galloway et Proctor, $\omega = 1$, $\epsilon = 1$ et $a = 1$.

Cet écoulement comporte deux points elliptiques et deux points hyperboliques. Ces derniers sont connectés par des orbites hétéroclines (pour $a = 1$) et deux orbites homoclines (pour $a \neq 1$). Les points de stagnation tournent avec une vitesse angulaire ω sur un cercle de rayon ϵ centré sur les points de stagnation du système non perturbé. Si l'on regarde une stroboscopie du système (2) (section de Poincaré aux temps $t = \frac{2\pi n}{\omega}$), les zones chaotiques occupent la majeure partie du domaine (Figure 1, Chapitre 2), menant à une dynamo efficace.

Nous avons initié une nouvelle approche, exposée dans les Chapitres B et C, tenant compte du caractère hamiltonien du système non perturbé, afin d'établir des liens entre des mesures du chaos sur un système hamiltonien faiblement perturbé et la dynamo engendrée par de tels écoulements.

[1] Childress, S. and Gilbert, A.D. 1995 Stretch, “Stretch, Twist, Fold: The Fast Dynamo ”. Springer-Verlag Lecture Notes in Physics: Monographs, **37**, 406 pages, ISBN 3-540-60258-5.

[2] Arnold,V.I. and Korkina, E.I. ”The grow of magnetic field in a incompressible flow.” *Vestn. Mosk. Univ. Mat. Mekh.* **3**, 43-46 (1983).

[3] Bayly, B. and Childress, S.” Construction of the fast dynamo using unsteady flows and map in three dimensions, *Geophys. Astrophys Fluid Dyn.* **44**, 221-240 (1988).

[4] Childress, S. ”Fast dynamo theory ” in ”Topological Aspect of the Dynamics of Fluids and Plasmas”,11-147, H.K Moffatt, G.M Zaslavsky, P.Conte and M.Tabor (eds.). *NATO ASI series E*, **218**, Kluwer (1992).

[5] Dombre. T, Frisch .U, Greene. J.M, Henon. M, Mehr. A and Soward A.M , ”Chaotic streamlines in the ABC flows”, *J. Fluid Mech.* **167**, 353-391 (1986).

[6] Du, Y., and Ott, E. ”Growth rates for fast dynamos and high Reynolds number fluid instabilities of chaotic flows”, *J. Fluid Mech.* **257** , (1993).

[7] Finn and Ott, E. ”Chaotic flows and fast magnetic dynamo”, *Phys.Fluid* **31**, 2992-3012 (1988).

[8] Galanti, B. ,Sulem, P.L., Pouquet, A.”Linear and nonlinear dynamos associated with ABC flows. *Geophys. Astrophys. Fluid Dyn* **66** (1992).

[9] Galloway, D.J. and Frisch, U.,”Dynamo action in a family of flows with chaotic stream lines” *Geophys. Astrophys .Fluid Dyn.* **36**, 53-83 (1986).

[10] Galloway, D.J. and Proctor, M.R.E. ”Numerical calculations of fast dynamo for smooth velocity field with realistic diffusion”, *Nature* **356**, 691-693 (1992).

[11] Hollerback, R., Galloway, D.J, and Proctor M.R.E. “Numerical evidence of fast dynamo action in sherical shell.”, *Phys. Rev. Lett.* **74**, 3145 (1995).

[12] Gilbert, A. ”Magnetic field evolution in steady chaotic flows”, *Phil. Trans. R. Soc. London*, **339**, 627-656 (1992).

[13] Klapper, I. and Young, L.S. ”Bounds on the fast dynamo growth rate involving topological entropy”, *Comm. Math. Phys.*, (1995).

[14] Lau, Y.-T., Finn, J.M., ”Fast dynamos with finite resitivity in steady flows with stagnation points” *Phys. Fluids*, B **5**, 365-375, (1993).

[15] Oseledets, V. "Fast dynamo problem for a smooth map on a two-torus", *Geophys. Astrophys. Fluid Dyn.* **73**, 133-145, (1993).

[16] Otani, N.F. "A fast kinematic dynamo in two-dimensional time dependent flows". *J. Fluid Mech.* **253**, 327-340 (1993).

[17] Ott, E., Du, Y., Sreenivasan, K.R., Juneja, A. and Suri, A.K. "Sign-singular measures : fast magnetic dynamos, and high-Reynolds-number fluid turbulence" *Phys. Rev. Lett.* **69**, 2654-2657 (1992).

[18] Ottino, J.M. " The Kinematics of Mixing: Stretching, Chaos and Transport", Cambridge Texts in Applied Mathematics, Cambridge University Press (1989).

[19] Parker, E.N "Hydromagnetic dynamo models.", J **122**, 293-314, (1955).

[20] Robert, G.O. "Dynamo action of fluid motions with two-dimensional periodicity". *Phil. Trans. Roy. Soc. London A* **271** , 411-454 (1972).

[21] Steenbeck, ., Krause, F., Rädler, K.-H. "A calculation of the mean electromotrice force in an electrically conducting fluid in turbulence motion, under the influence of Coriolis forces. *Z Naturforsh*, **21a**, 369-376, (1966).

[22] Soward, A.M. "Fast dynamo action in steady flow". *Fluid Mech.* , **180** , 267-295 (1987).

[23] Soward, A.M. "An asymptotic solution of a fast dynamo in two-dimensional pulsed flow". *Geophys. Astrophys. Fluid Dyn.* **73**, 179-215 (1993).

[24] Vainshtein, S.I and Zeldovich, Ya.B. "Origin of magnetic fields in astrophysics", *Usp. Fiz. Nank.* **106**, 431-457, (*Sov. Phy. Usp.* **15**, 159-172) (1972).

[25] Vishik, M.M. (1992) unpublished.

Chapitre B

Dynamo cinématique dans un flot hamiltonien faiblement perturbé

En utilisant l'écoulement CP+ϵ de Galloway et Proctor (1992) [8] comme un système hamiltonien faiblement perturbé, nous pouvons utiliser des outils évaluant la dynamique chaotique.

$$\mathbf{u}_{CP+\epsilon} = \begin{bmatrix} a\sin[z+\epsilon\sin(\omega t)] + \cos[y+\epsilon\cos(\omega t)] \\ acos[z+\epsilon\sin(\omega t)] \\ \sin[y+\epsilon\cos(\Omega t)] \end{bmatrix} \tag{1}$$

Pour une faible perturbation du système, les zones chaotiques se concentrent autour des variétés instables reliant les points hyperboliques de l'écoulement (Figure 1).

Pour une faible perturbation fixée, la taille des domaines chaotiques autour des variétés instables varie avec la fréquence de la perturbation temporelle (Figure 2). La largeur des bras chaotiques peut être estimée par la distance entre les variétés stables et instables. Cette distance est évaluée perturbativement par la méthode de Melnikov, qui est généralement utilisée pour tester la présence d'orbites homoclines transverses à la variété stable et conduisant à une dynamique chaotique. Cette distance calculée et majorée sur toute l'orbite est dépendante de la fréquence de perturbation, définissant ainsi une fonction avec la seule variable ω. Cette fonction reproduit bien la variation de la largeur de la zone chaotique en fonction de la fréquence de la perturbation (Figures 2 et 3).

Nous avons effectué des mesures classiques du chaos, comme les exposants de Lyapunov. La dépendance du plus grand des exposants de Lyapunov en fonction des grandes fréquences de la perturbation est différente de la fonction de Melnikov (Figure 3a et 4b). Contrairement à la fonction de Melnikov, les exposants de Lyapunov semblent saturer pour les grandes fréquences de la perturbation.

Un code spectral a été développé pour intégrer l'équation d'induction (2) avec l'écoulement CP+ϵ,

$$\partial_t \mathbf{b} = \nabla \times (\mathbf{u}_{CP+\epsilon} \times \mathbf{b}) + \frac{1}{R^M} \Delta \mathbf{b} \ , \tag{2}$$

Ce code utilise, comme Galloway et frisch [9], la structure particulière de l'écoulement choisi pour simplifier les interactions non linéaires. Le taux de croissance exponentiel de la dynamo pour des valeurs du nombre de Reynolds magnétique R^M variant sur quatre décades est ainsi obtenu en fonction de la fréquence de perturbation. Ces résultats sont présentés dans les Figures 6, 7 et 8. Ils montrent l'existence d'une dynamo rapide pour des fréquences autour de l'unité, et un régime de dynamo lente pour les petites et les grandes fréquences.

Les exposants de Lyapunov qui mesurent la divergence des trajectoires sont insuffisants pour expliquer la dépendance en fréquence du taux de croissance de la dynamo. La fonction de Melnikov, avec un caractère plus géométrique, semble mieux prédire la variation du taux de la dynamo avec ω (Figure 3a et 7). Les structures associées à une dynamo rapide sont localisées le long des variétes instables, avec le maximun proche des points hyperboliques (Figure 9 et 10). Dans le cas des deux orbites homoclines, la fonction de Melnikov prédit des taux de croissances différents pour les deux trajectoires homoclines. Pour une fréquence donnée, nous voyons les structures magnétiques émerger sur l'une ou l'autre des orbites homoclines en accord avec les prédictions de la fonction de Melnikov (Figure 3b et 10), résultat mis en lumière pour la première fois sur ce modèle.

Il faut aussi noter la présence de structures magnétiques plus larges, se localisant autour des points elliptiques et associées à un régime de dynamo lente.

Nous avons ainsi montré quantitativement l'importance de la largeur des zones chaotiques pour l'établissement d'une dynamo rapide dans un écoulement proche de l'intégrabilité. La largeur et le taux de la dynamo sont sensibles à la fréquence de la perturbation qui sont prédits la méthode de Melnikov.

L'effet dynamo présent dans un écoulement proche de l'intégrabilité dépend fortement de la géométrie et de la configuration des variétés instables autour des points hyperboliques. Ces résultats ont motivé une approche analytique effectuée par Childress et Gilbert presentée dans le Chapitre 8 de “Stretch, Twist, Fold: The Fast Dynamo ”. Springer-Verlag (1995). Avec une théorie perturbative, ils ont retrouvé le comportement du taux de croissance de la dynamo dans les domaines de faibles et fortes fréquences de la perturbation temporelle.

Dynamos in weakly chaotic two-dimensional flows

Y. Ponty, A. Pouquet and P.L Sulem
CNRS URA 1362, Observatoire de la Côte d'Azur
B.P. 4229, 06304 Nice Cedex 04, France

J. Geophys. Astrophys. Fluid Dyn. **79**, 239 (1995).

Abstract

The dynamo action of a time-periodic two-dimensional flow, close to integrability is analyzed. At fixed Reynolds number R^M and frequency ω, magnetic structures develop in the form of both eddies and filaments. The growth rate of the eddies appears to be the same for all frequencies and decreases with R^M, while the growth rate of filaments displays a strong ω-dependence and, except in the limit of zero or infinite frequencies, converge to a non-zero value as $R^M \to \infty$. Magnetic filaments develop in the widest chaotic zones located near the homoclinic or heteroclinic tangles, and their growth rate is strongly influenced by the width of these zones which is estimated using Melnikov formalism. This study illustrates quantitatively that not only a local stretching but also a sizable chaotic zone is requited for fast dynamo action.

1 Introduction

Dynamo action in electrically conducting fluids is often considered as the basic mechanism at the origin of the magnetic field in astro and geophysical objects. In the situation where the magnetic Reynolds number R^M is large, the growth rate of a seed magnetic field often appears to be related to the advection rather than the diffusion time scale. This provided a main motivation to the efforts devoted to the problem of existence of "fast dynamos" (Vainstein and Zeldovich 1972) which persist in the limit $R^M \to \infty$, [see Childress (1992) for a recent review]. It was often conjectured, and recently proved in the case of spatially smooth underlying flow (Vishik 1992, Klapper and Young 1994), that fluid trajectories are to be chaotic (Lagrangian chaos) for existence of a fast dynamo. Definite evidences of fast dynamos are mostly restricted to discrete flow models (mappings) (Bayly and Childress 1988, Finn and Ott 1988, Gilbert 1992), or to velocity fields displaying singularities (Soward 1987). The understanding is more limited in the case of smooth flows. A possible candidate is the steady three-dimensional ABC flow (Dombre and al. 1986), but the range of magnetic Reynolds numbers for which the magnetic growth rate was seen to be almost constant, is insufficient to conclude unambiguously (Arnold and Korkina 1983, Galloway and Frisch 1986). An explicit example of the spatial structure of the magnetic field resulting from a chaotic dynamo was given by Oseledets (1993).

Examples of flows that seem well-suited for probing the large magnetic Reynolds number limit depend on two space coordinates but are unsteady (Galloway and Proctor 1992, Otani 1993). In this context, magnetic field modes with the different wavevector component in the third direction evolve independently. Consequently, a specific value for this component can be prescribed and the magnetic field computed using a two-dimensional code. An analytical estimate of the growth rate was recently obtained for a flow obtained by pulsing two distinct Beltrami waves (Soward 1993), but the problem of the exchange of the limits (infinite Reynolds number and vanishing transition time between the pulses) remains open. In the case of time-continuous flows, convincing numerical evidence of fast dynamo action was obtained by numerical simulations at magnetic Reynolds numbers up to 10^4 of the so called "circularly polarized model" (CP) (Galloway and Proctor 1992)

$$\mathbf{u} = \begin{cases} A\sin(z+\epsilon\sin\Omega t) + C\cos(y+\epsilon\cos\Omega t) \\ A\cos(z+\epsilon\sin\Omega t) \\ C\sin(y+\epsilon\cos\Omega t) \end{cases}, \qquad (1)$$

which can be viewed as a time-dependent perturbation of the Robert cellular flow (Robert 1972). In the present paper, we concentrate on the dynamo action of the CP flow in the regime when the perturbation is assumed to be weak (small ϵ). The regions of chaos for the underlying dynamical system are then confined near the heteroclinic (when $A = C$) or homoclinic (when $A \neq C$) orbits of the Robert flow. The main issues concern the sensitivity of the dynamo growth rate to the degree of the chaos of the underlying flow and the geometry of the emerging magnetic field, when the flow parameters are varied. Preliminary investigations of the case $A = C$, were reported in Ponty and al. (1993).

2 The CP flow

The fluid trajectories of the CP flow, to be understood mod 2π, obey

$$\begin{array}{l} \dot{y} = A\cos(z + \epsilon \sin \Omega t) \\ \dot{z} = C \sin(y + \epsilon \cos \Omega t) \end{array} \quad , \qquad (2)$$

together with

$$\dot{x} = A \sin(z + \epsilon \sin \Omega t) + C \cos(y + \epsilon \cos \Omega t). \qquad (3)$$

By dividing (2) and (3) by C and rescaling time in the form $\tau = Ct$, it is easily seen that in addition to the perturbation amplitude ϵ, the dynamical system depends on the reduced frequency $\omega = \Omega/C$ and on the ratio $a = A/C$. In the absence of perturbation ($\epsilon = 0$), the two-dimensional system (2) admits two elliptic stagnation points $(0, \pi/2)$ and $(\pi,\ 3\pi/2)$, and also two hyperbolic ones $(0\ ,\ 3\pi/2)$, and $(\pi\ ,\ \pi/2)$. These latter points are connected by heteroclinic orbits for $a = 1$, while the system displays homoclinic trajectories when $a \neq 1$. For $\epsilon \neq 0$, the stagnation points rotate with angular velocity ω on circles of radius ϵ, centered at the stagnation points of the unperturbed system.

Useful insight on the dynamics of system (2) is provided by Poincaré sections (stroboscopic views) at times $\tau = \frac{2\pi n}{\omega}$ with $n \in \mathcal{N}$. Figure 1 displays such sections for $\omega = 0.8$, when $a = 1$ (on the left hand side) and $a = 0.5$ (on the right hand side), with $\epsilon = 1,\ 0.5,\ 0.2$ and 0.1 (from top to bottom). The case $a = \epsilon = 1$ is closed to the situation considered by Galloway and Proctor (1992) where $\Omega = 1$, $A = C = \sqrt{\frac{3}{2}}$, corresponding to $\omega = 0.8165$. The chaotic regions cover a significant part of the plane for ϵ of order unity but concentrate near the heteroclinic or homoclinic orbits of the unperturbed system when ϵ is decreased. For $a = 1$, these regions are connected, and only one initial condition is necessary to generate the pictures, while, for $a \neq 1$, there are two disjoint chaotic regions, when ϵ is small enough. A non trivial effect on the size of the chaotic zones is obtained by varying the frequency ω of the perturbation. Figure 2 shows the Poincaré section in the (y, z)-plane in the cases $a = 1$ and $a = 0.5$, for $\epsilon = 0.1$ and various values of the frequency

ω. Significant changes in the thickness of the chaotic regions is visible. We observe in the case $a = 0.5$ that the widths of the chaotic regions associated with distinct homoclinic orbits of the unperturbed system may be different. Note in particular the tiny chaotic zone near the "inner" homoclinic orbit when $\omega = 0.6$, and near the "outer" one when $\omega = 1.9$. As suggested by Leonard and al. (1987) and by Ottino (1989), the thickness of the chaotic zones can be estimated by the distance between the stable and unstable manifolds resulting from perturbations of homoclinic or heteroclinic trajectories. In the case of nearly integrable flows, this distance can be computed perturbatively using the Melnikov method, an approach often used to test the existence of transverse homoclinic orbits, leading to Smale horse-shoes and chaotic dynamics (Ottino 1989, Guckenheimer and Holmes 1983).

As noticed in Ponty and al. (1993), the change of variables

$$\begin{aligned} u &= z - \pi/2 + \epsilon \sin \omega\tau \\ v &= y + \epsilon \cos \omega\tau \end{aligned} \qquad (4)$$

put eq.(2) in the standard form

$$\dot{\mathbf{U}} = \mathbf{f} + \epsilon \mathbf{g} \quad , \qquad (5)$$

for the implementation the Melnikov method (Guckenheimer and Holmes 1983). Here $\mathbf{U} = (u, v)$, $\mathbf{f} = (\sin v, -a \sin u)$ and $\mathbf{g} = (\omega \cos \omega\tau, -\omega \sin \omega\tau)$. To leading order, the distance between the stable and unstable manifold is given by

$$d(\tau_0) = \epsilon \, \frac{M(\tau_0)}{\mid \mathbf{f}(\mathbf{q}_0(0)) \mid}$$

with

$$M(\tau_0) = \int_{-\infty}^{\infty} \mathbf{f}(\mathbf{q}_0(\tau)) \times \mathbf{g}(\mathbf{q}_0(\tau), \tau + \tau_0) \, d\tau \ , \qquad (6)$$

where $\mathbf{q}_0(t)$ denotes the (unperturbed) homoclinic or heteroclinic orbit. When $\mathbf{q}_0(0)$ is taken at finite distance of the hyperbolic fixed point, $\mid \mathbf{f}(\mathbf{q}_0(0)) \mid$ is of order unity.

For $\epsilon = 0$,the system (2) admits four homoclinic or heteroclinic orbits, $\mathbf{q}_0^j = (u_0^j, v_0^j)$, labelled by the subscript j. For each of them, eq.(6) becomes

$$M^j(\tau_0) = -\omega \int_{-\infty}^{\infty} \sin v_0^j(\tau) \ \sin(\omega(\tau + \tau_0)) \, d\tau + a \, \omega \int_{-\infty}^{\infty} \sin u_0^j(\tau) \ \cos(\omega(\tau + \tau_0)) \, d\tau \ . \qquad (7)$$

For $a = 1$, the chaotic regions are connected and in this case we are mostly interested in the function $F(\omega) = \sup_j \sup_{\tau_0} \mid M^j(\tau_0) \mid$ we refer to as the "Melnikov function". As shown in Ponty and al. (1993), for $a = 1$, we have $F(\omega) = \omega\pi\ \mathrm{sech}(\frac{\pi\omega}{2})$, a quantity plotted in fig.3a.

In the case $a \neq 1$, the system displays two distinct chaotic zones for small enough ϵ. The Melnikov functions associated to each of these zones are computed in the Appendix and plotted in fig.3b. Note the existence of several zeros and local maxima. The existence of tiny chaotic zones visible in fig.2 clearly correspond to the very small value of the associated Melnikov functions.

Another important characteristic of a chaotic system is provided by the Lyapunov exponents and in particular the largest one L which estimates the maximum rate of stretching of the magnetic field. The variation of L for $a = 1$, is plotted as a function of ϵ, when $\omega = 0.8$ in fig.4a, and as a function of ω for $\epsilon = 0.1$ in fig.4b. We observe that at fixed ω, the largest Lyapunov exponent (like the area of the chaotic zone) tends to saturate when ϵ is increased. Furthermore, its variation with ω when $\epsilon = 0.1$ shows that for ω close to 3 or larger (for which the chaotic zones are very small), L remains significant, indicating an important but localized stretching of the magnetic field. A similar result holds when $a \neq 1$. In this case, the chaotic zones are not connected and different although close values are obtained for the Lyapunov exponents of trajectories lying in distinct chaotic regions.

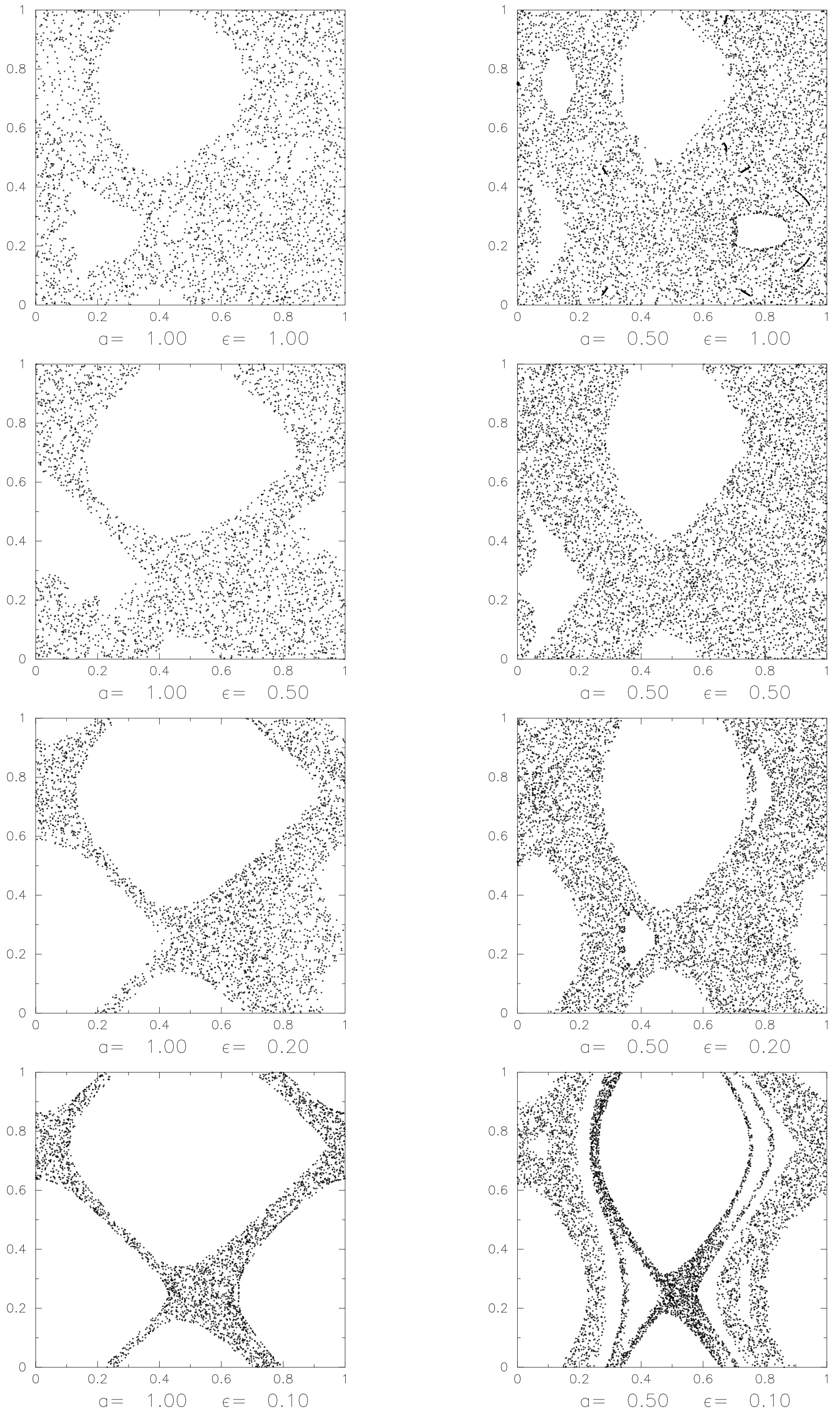

Figure 1: Stroboscopic views at times $t = \frac{2\pi n}{\omega}$ of the fluid trajectories in a 2π-periodic box of the underlying flow (2) with a = A/C = 1 (left) and a = A/C = 0.5 (right) for different amplitudes ϵ of the time periodic perturbation, when the reduced frequency is $\omega = \Omega/A = 0.8$.

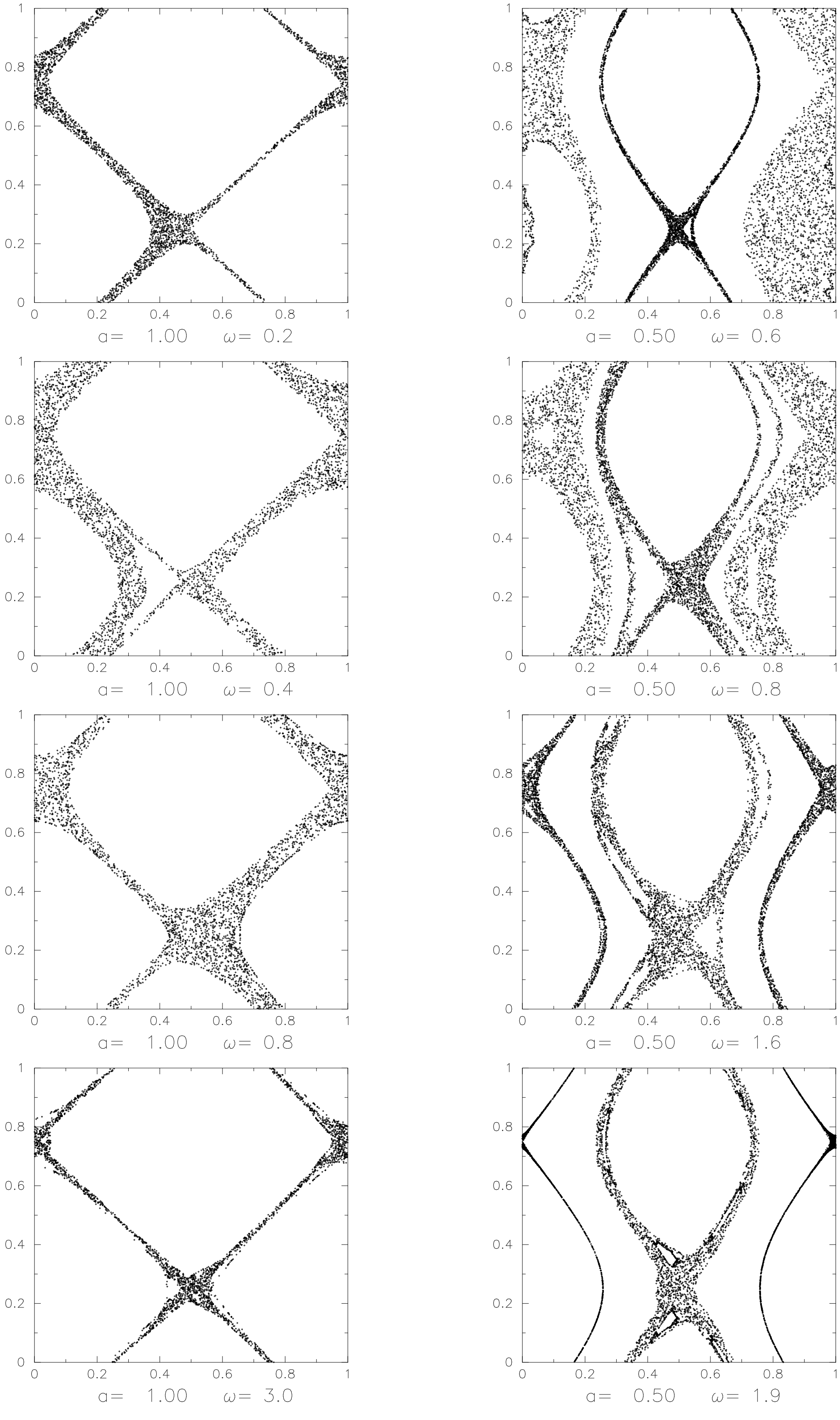

a= 1.00 ω= 0.2

a= 0.50 ω= 0.6

a= 1.00 ω= 0.4

a= 0.50 ω= 0.8

a= 1.00 ω= 0.8

a= 0.50 ω= 1.6

a= 1.00 ω= 3.0

a= 0.50 ω= 1.9

Figure 2: Same stroboscopic views as in Figure 1 with $\epsilon = 0.1$ and various ω, for $a = 1$ (left) and $a = 0.5$ (right).

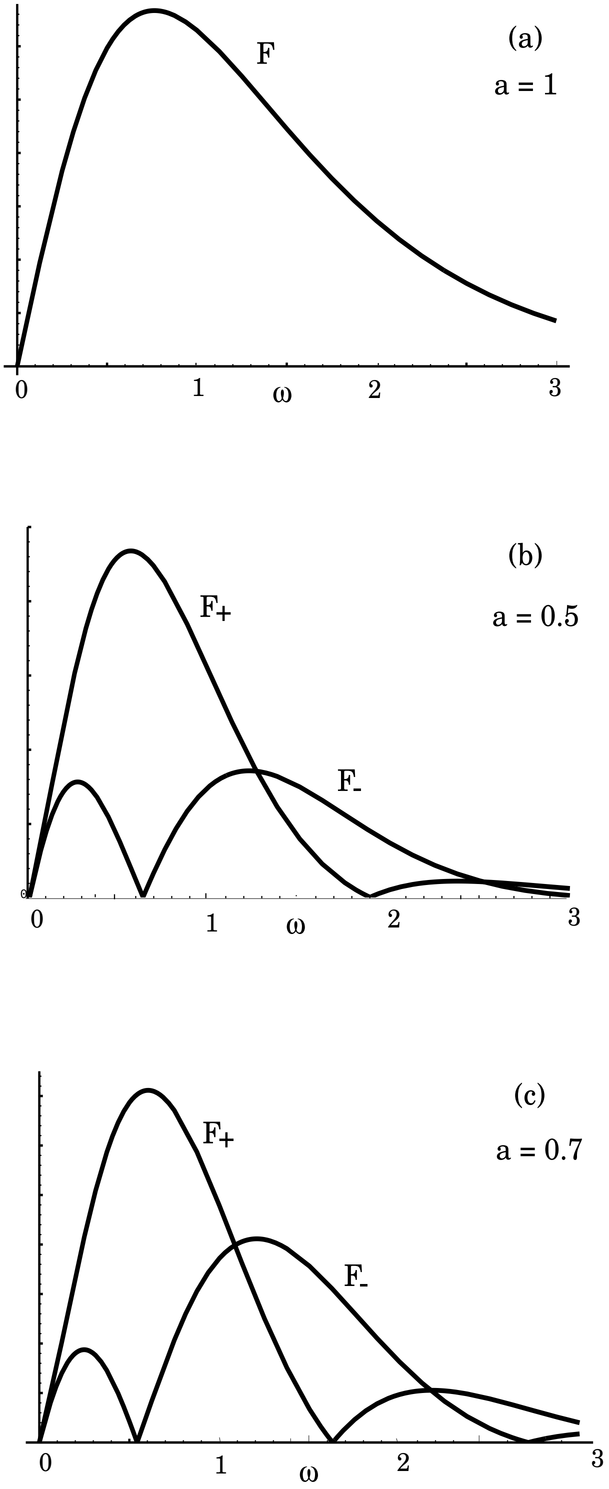

Figure 3: (a) The Melnikov function for a=1; (b) Melnikov functions F_+ and F_- associated to the outer and inner chaotic zones respectively, for a=0.5. (c) Melnikov functions F_+ and F_- for a=0.7.

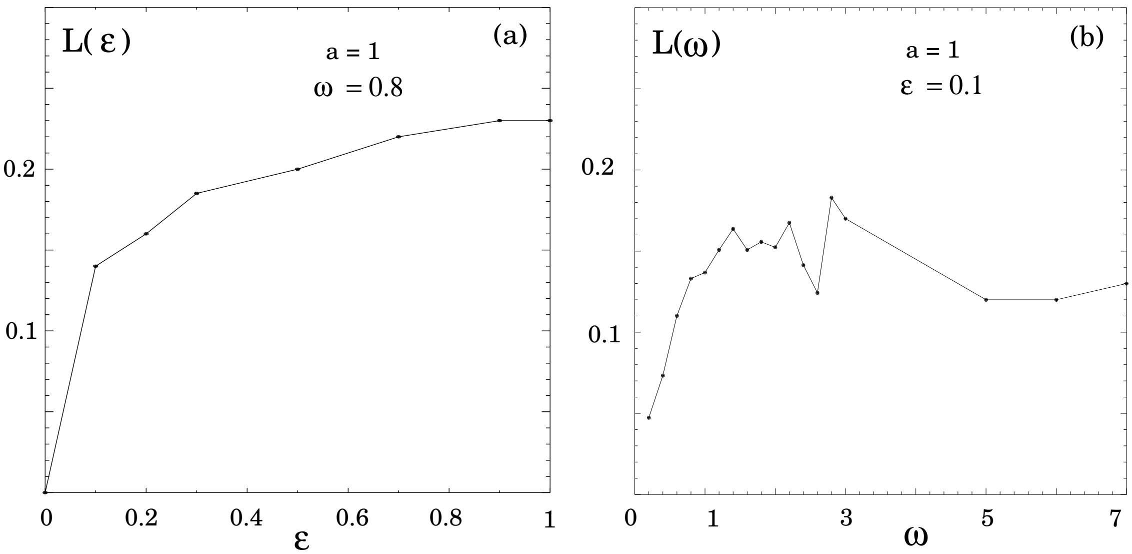

Figure 4: Largest Lyapunov exponent L for a=1: (a) versus ϵ for $\omega = 0.8$; (b) versus ω for $\epsilon = 0.1$

3 Dynamo growth rates

Two series of numerical integrations of the induction equation

$$\partial_t \mathbf{b} = \nabla \times (\mathbf{u} \times \mathbf{b}) + \frac{1}{R^M} \Delta \mathbf{b} \ , \qquad (8)$$

have been performed with the velocity field (2), one with $A = C = \sqrt{\frac{3}{2}}$ (corresponding to $a = 1$) and the other with $A = \frac{C}{2} = \sqrt{\frac{3}{5}}$ (for which $a = 0.5$). In both series of runs, the parameters ϵ and ω are varied. We concentrate on magnetic fields with a wavevector component in the x-direction $k_1 = 0.57$, as in Galloway and Proctor (1992). Furthermore, the velocity field (1) including only Fourier modes of wavenumber unity, the induction equation is efficiently solved in the spectral space, since in this case, the convolutions require, for each direction, a number of operations equal to the number of retained modes. We observe that as R^M exceeds a critical value of order of a few units (depending on the velocity field parameters), a dynamo action takes place and, after a transient, the magnetic energy $E^M = \int | B |^2 d\mathbf{x}$ grows exponentially. This "kinematic dynamo" where the flow motion is given, models the early time amplification of a seed magnetic field. Later on, the magnetic field usually reacts on the flow through the Lorentz force, leading to a saturation of the dynamo, a question which is beyond the object of the present paper.

We are here mainly interested in the influence of the velocity parameters on the dynamo growth rate $\lambda = \lim_{t\to\infty} \frac{1}{2t} ln E^M$. Special attention is devoted to the limit $R^M \to \infty$, an asymptotic regime which is approached non uniformly, and requires larger Reynolds numbers as ϵ is decreased. The influence of the deviation from integrability of the underlying flow is illustrated in fig.5a which displays the variation of λ with ϵ, for $a = 1$, $\omega = 0.8$ and $R^M = 500$. For comparison, the variation of the relative area S of the chaotic zones in the (y-z)-plane is plotted in fig.5b. A strong correlation between the two quantities is visible, although the Reynolds number is moderate.

In the context of a fast dynamo, an important issue is the variation of the growth rate λ with the magnetic Reynolds number R^M. Figure 6 shows this variation for $a = 1$ and different values of the perturbation frequency ω within the intervals (a) $0.2 \leq \omega \leq 0.8$ and (b) $0.8 \leq \omega \leq 3.0$. For low Reynolds numbers, the growth rate is essentially independent of ω, whereas a non trivial dependency emerges when R^M exceeds a few tens. The maximal growth rate occurs near $\omega = 0.8$. At this frequency, a tendency of λ to saturate is seen when the Reynolds number reaches values of order 10^4. Such large values of R^M are required because of the smallness of ϵ (here equal to 0.1). In the case $\epsilon = 1$ and ω

close to 0.8 considered by Galloway and Proctor (1992), convergence was obtained with $R^M \sim 100$. Furthermore, at both low and high frequencies within the considered range, we observe an intermediate domain of Reynolds numbers for which λ is independent of ω and decreases with R^M. At higher Reynolds numbers (depending on ω), a different behavior is observed: the growth rate increases with R^M and shows a tendency to saturate at a finite value, indicative of a fast dynamo. The Reynolds numbers we used seem insufficient to approach this asymptotic regime when $\omega > 1.6$.

The variation of the growth rate λ with ω for the simulations at the largest available magnetic Reynolds numbers is conveniently presented in fig.7. For both small and large values of ω, plateaux whose amplitude decreases with R^M, are visible. At moderate Reynolds numbers, two maxima are present near $\omega = 0.8$ and $\omega = 1.4$, and tend get nearer as R^M is increased. This picture of bumps and plateaux suggests that two types of dynamos are operating in such flows. For values of the perturbation frequency ω near unity, the convergence of the magnetic field growth rate as the Reynolds number is increased, indicates the existence of a fast dynamo. As seen on fig.5, the presumed asymptotic growth rate for $\omega = 0.8$ and $\epsilon = 0.1$ is about 0.11, roughly one third of the value gives by Galloway and Proctor (1992) for $\epsilon = 1$. On the other hand, the two plateaux are indicative of a slow dynamo, at least if the behavior we observe can be extrapolated to infinite Reynolds numbers.

When analyzing the influence of the frequency ω on the dynamo efficiency, we note the case of small ϵ (fig.7), the proximity of the largest magnetic field growth rate and the maximum of the Melnikov function (fig.3a). In contrast, this frequency range is by no way singled out for the largest Lyapunov exponent (fig.4). This suggests that, at least for weakly chaotic systems (small ϵ), the width of the chaotic zones has a dominant influence on the efficiency of the dynamo action. An estimate of the magnetic growth rate was proposed by Ott and al. (1992) and Du and al. (1993) in terms of Lyapunov exponents, and of the cancellation exponent which characterizes the complexity of the small-scale structure of the emerging magnetic field. A measure of this exponent requires huge Reynolds numbers, several orders of magnitudes in excess of those used in the present simulations where, as seen in fig.12, individual magnetic field lobes are well-resolved but scanty.

In the case $a = 0.5$, for which heteroclinic connections are replaced by homoclinic orbits in the unperturbed underlying flow, fig. 8 shows the growth rate λ versus ω at Reynolds number $R^M = 500$, for $\epsilon = 0.1$ and 0.2. In the latter case, chaotic zones in the Poincaré section which are distinct for $\epsilon = 0.1$ have merged (see fig.1) and the growth rate remains significant on a more extended range of frequencies. Although the Reynolds number is moderate, the growth rate appears to be again dominant near $\omega = 0.8$, not far from the maximum $\omega = 0.6$ of the largest Melnikov function (fig.3b), and this for both values of ϵ .

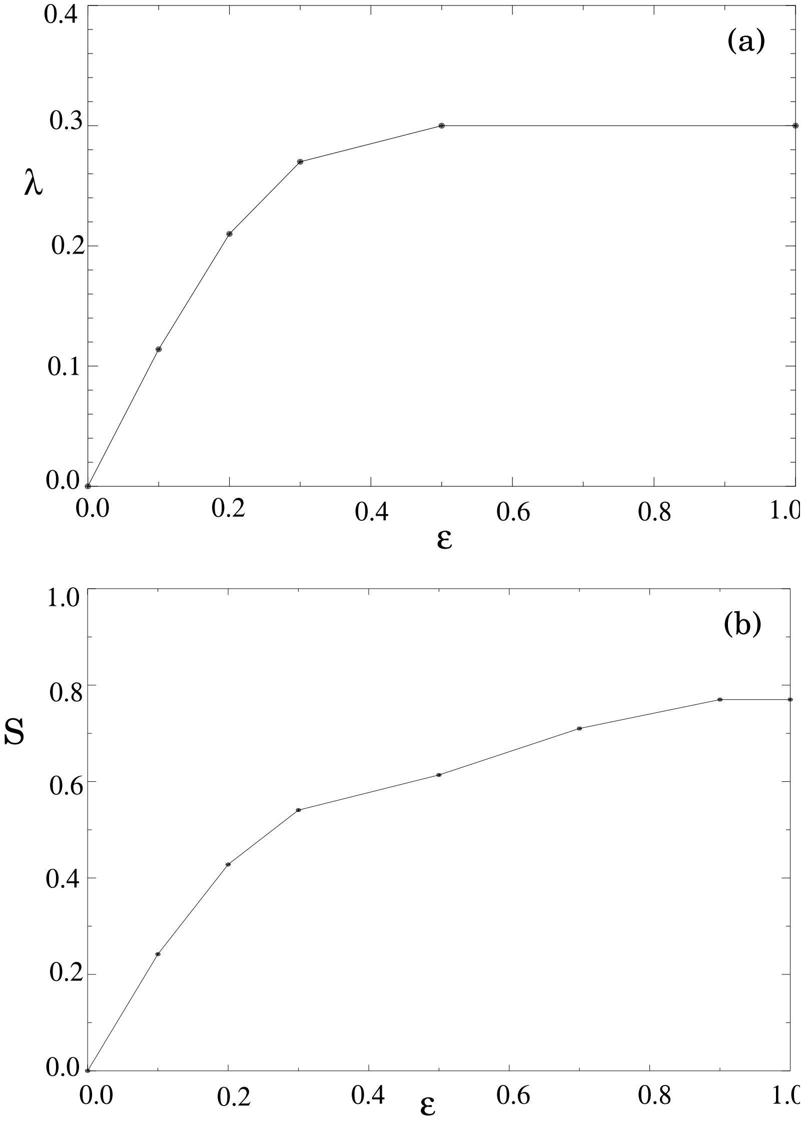

Figure 5: (a) Magnetic field growth rate λ versus ϵ for a = 1, $\omega = 0.8$ and $R^M = 500$. (b) Variation with ϵ of the fraction S of the (y-z)-domain associated with a chaotic dynamics for $\omega = 0.8$.

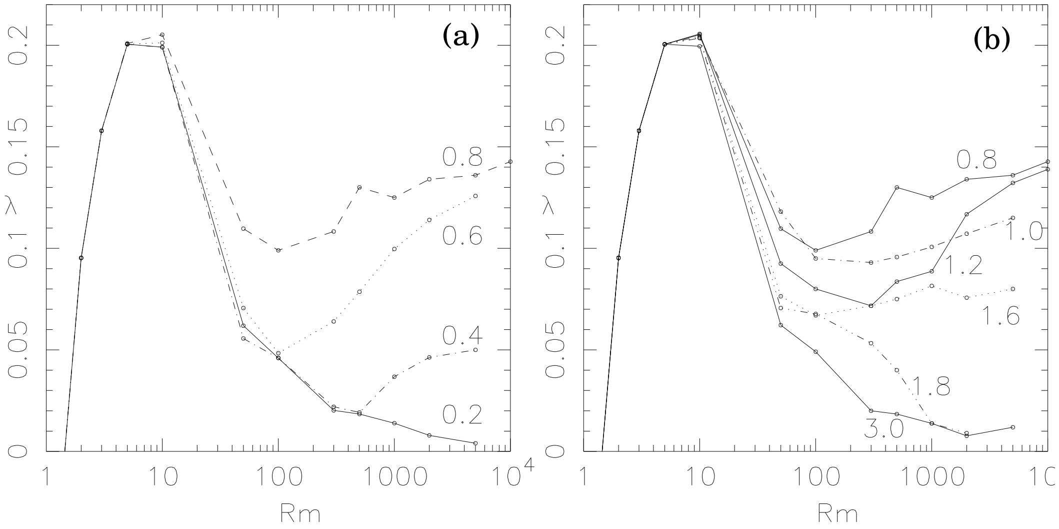

Figure 6: Magnetic field growth rate λ versus the magnetic Reynolds number R^M for $a = 1$. Curves are labelled by the corresponding values of ω.

4 Geometry of the magnetic field

Figure 9 shows for $a = 1$, $\epsilon = 0.1$ and various values of the frequency ω, the contours of the magnetic field strength $\mid b \mid$ in the plane $x = 0$, when the exponential growth is well established. Figure 10 presents similar results for $a = 0.5$. It is clear from both figures that two types of structures have emerged. Roundish magnetic eddies are dominant for both low and high values of ω, whereas elongated filaments dominate for values of ω near the maximum growth rate. Eddies are localized in the vicinity of elliptic stagnation points, while filaments are concentrated in the immediate neighborhood of the unstable manifolds of the hyperbolic stagnation points with the peak field centered close to them.

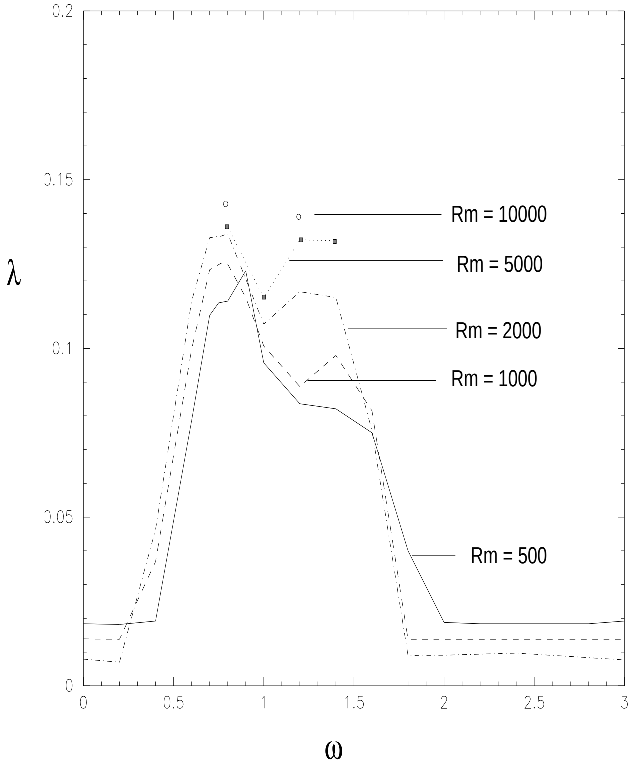

Figure 7: Magnetic field growth rate versus ω for several Reynolds numbers.

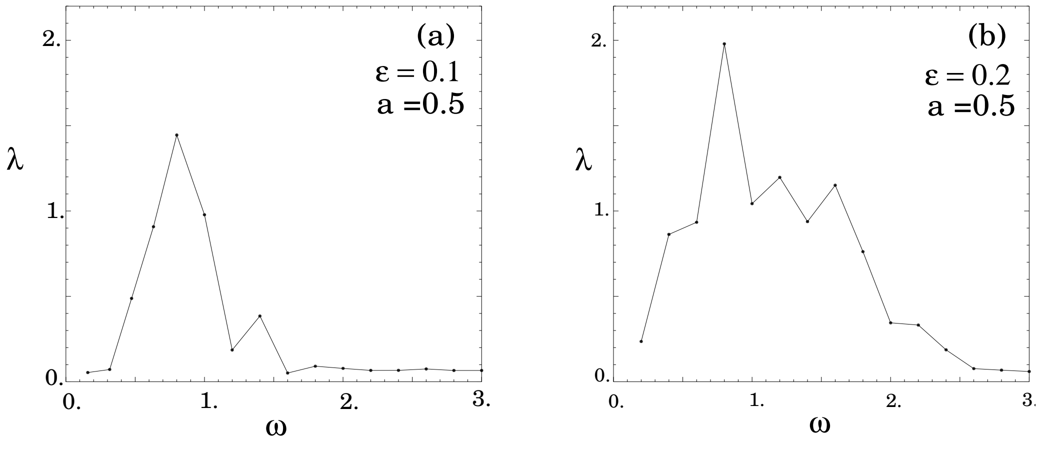

Figure 8: Growth rate λ versus ω at Reynolds numbers $R^M = 500$, for a $= 0.5$, (a) when $\epsilon = 0.1$ (a) and (b) $\epsilon = 0.2$ (b).

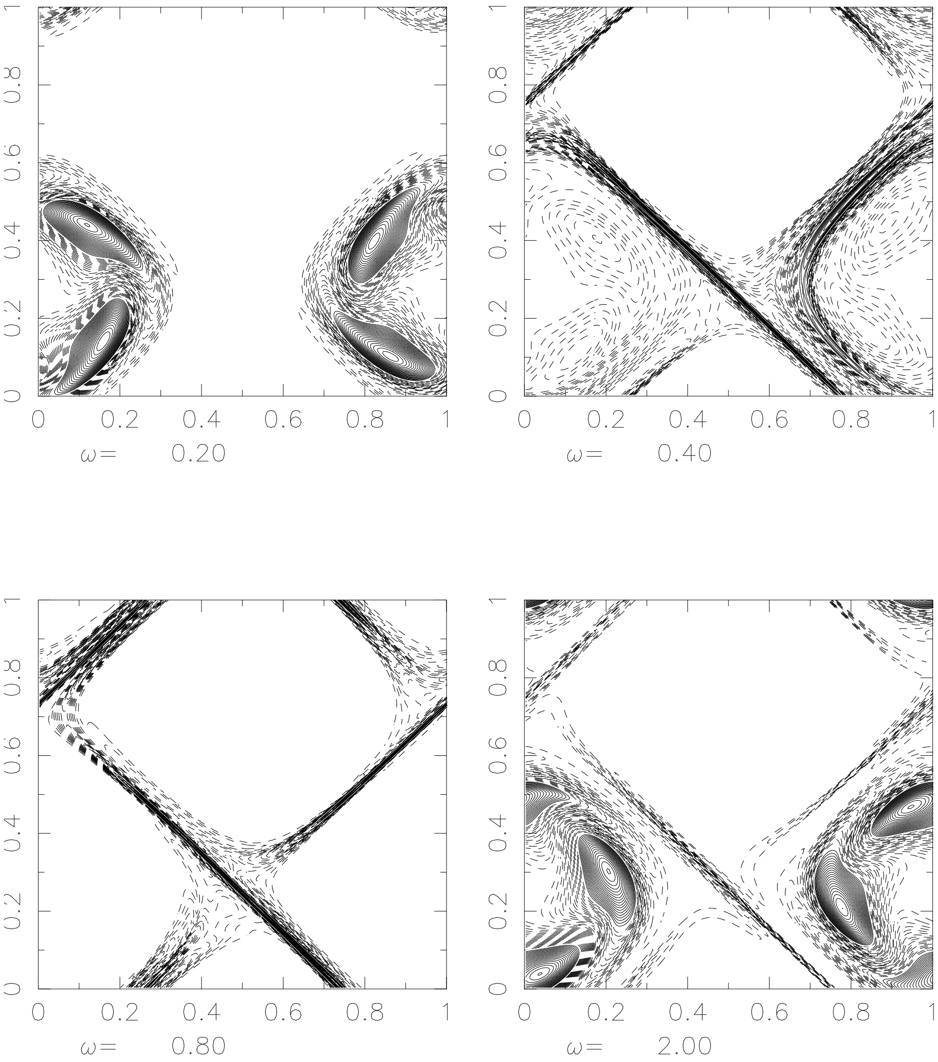

Figure 9: Magnetic contours for a = 1, $\epsilon = 0.1$, $R^M = 2000$ and various ω.

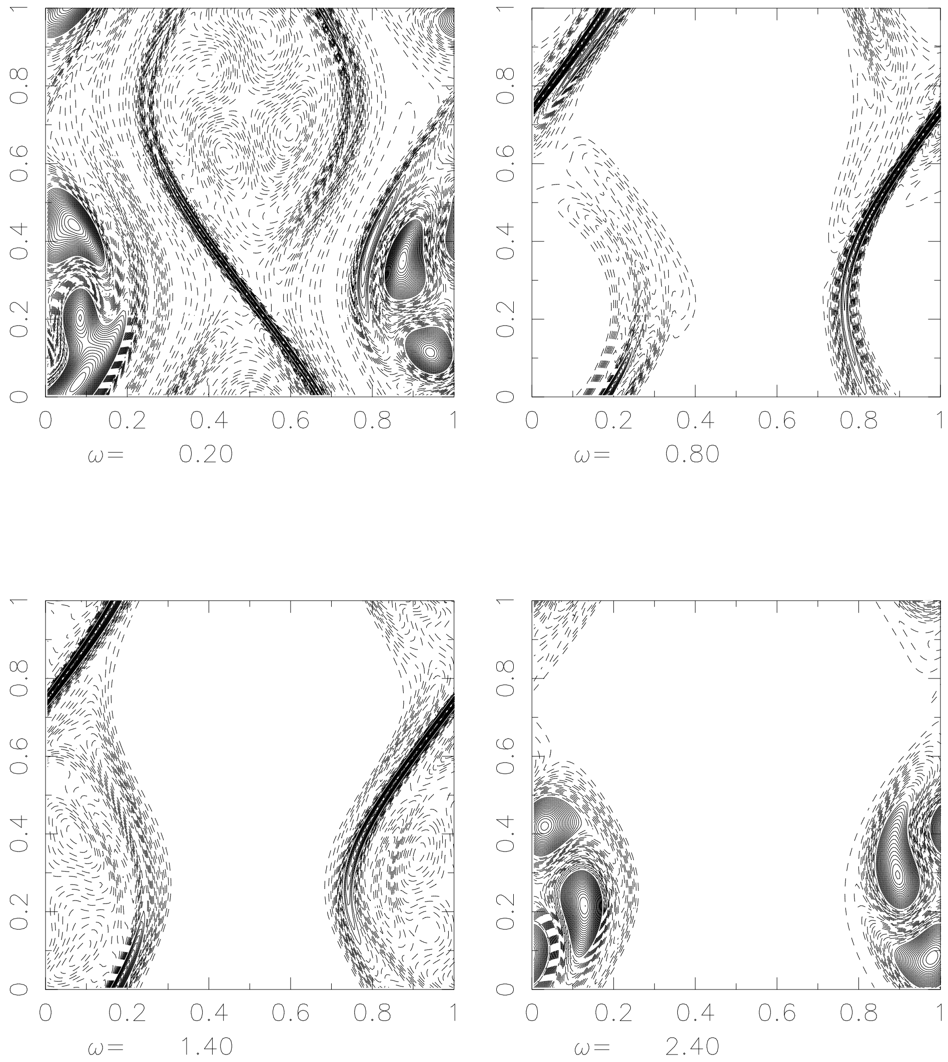

Figure 10: Magnetic contours for a = 0.5 , $\epsilon = 0.1$, $R^M = 2000$ and various ω.

The three-dimensional perspectives displayed in fig.11 for $a = 1$, show that the eddies are associated with magnetic fields transverse to the (y, z)-plane and pointing in opposite directions. The filaments are mostly contained within the (y,z)-plane, and as the Reynolds number is increased, the magnetic field modulus displays more spatial oscillations in the transverse direction (fig.12). The relative importance of the eddies and the filaments may depend on time, since their growth rates are different. A quantitative measurement was made for $a = 1, \epsilon = 0.1$ and $R^M = 500$. For all tested values of the frequency ω, the growth rate of the eddies remains essentially constant and close to 0.02, whereas the filament growth rate (which strongly depends on ω) dominates, except possibly for very small and very large ω. The lack of dependence on ω of the eddy growth rate is at the origin of the plateaux displayed in fig. 7, which were seen to decrease with R^M, a characteristic property of a slow dynamo. In contrast, the filaments seem associated to fast dynamo action.

(a)

$\omega = 0.2$

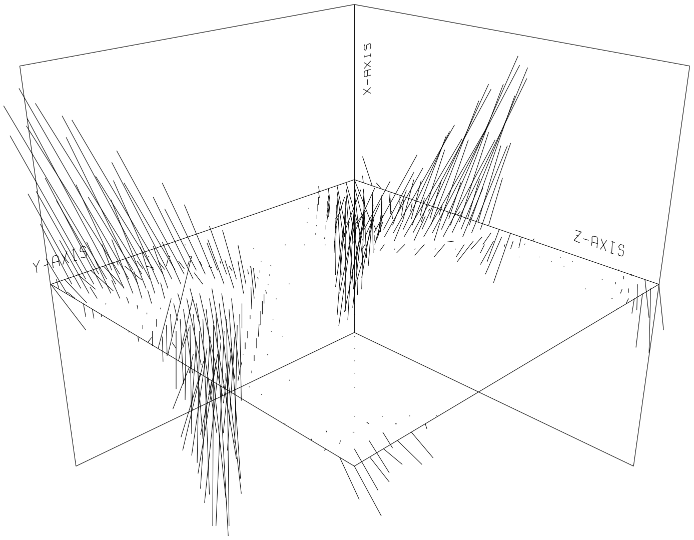

(b)

$\omega = 0.8$

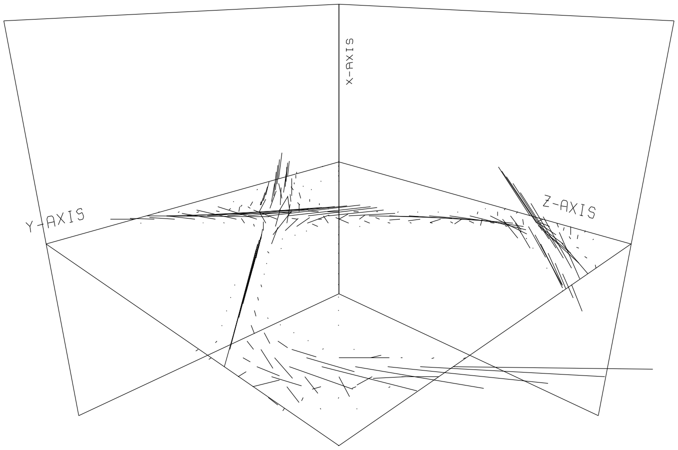

Figure 11: Three-dimensional perspective view of the magnetic field when a = 1 and $R^m = 500$. (a) for $\omega = 0.2$, (b) for $\omega = 0.8$.

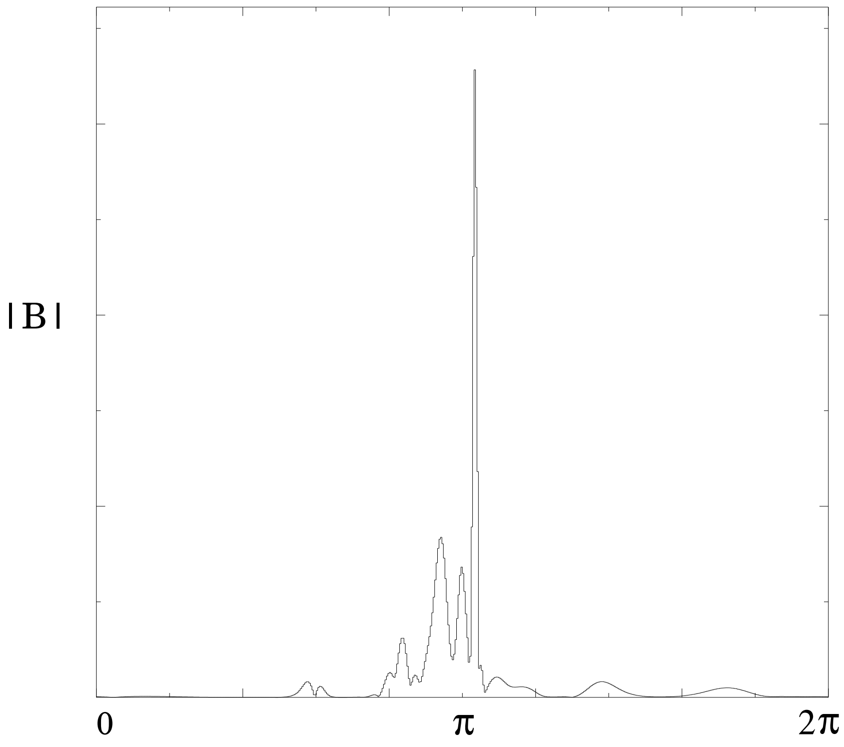

Figure 12: Variation of the magnetic field modulus along $z = \frac{\pi}{2}$, for $\omega = 0.8$, a = 1 and $R^M = 5000$ (linear scale).

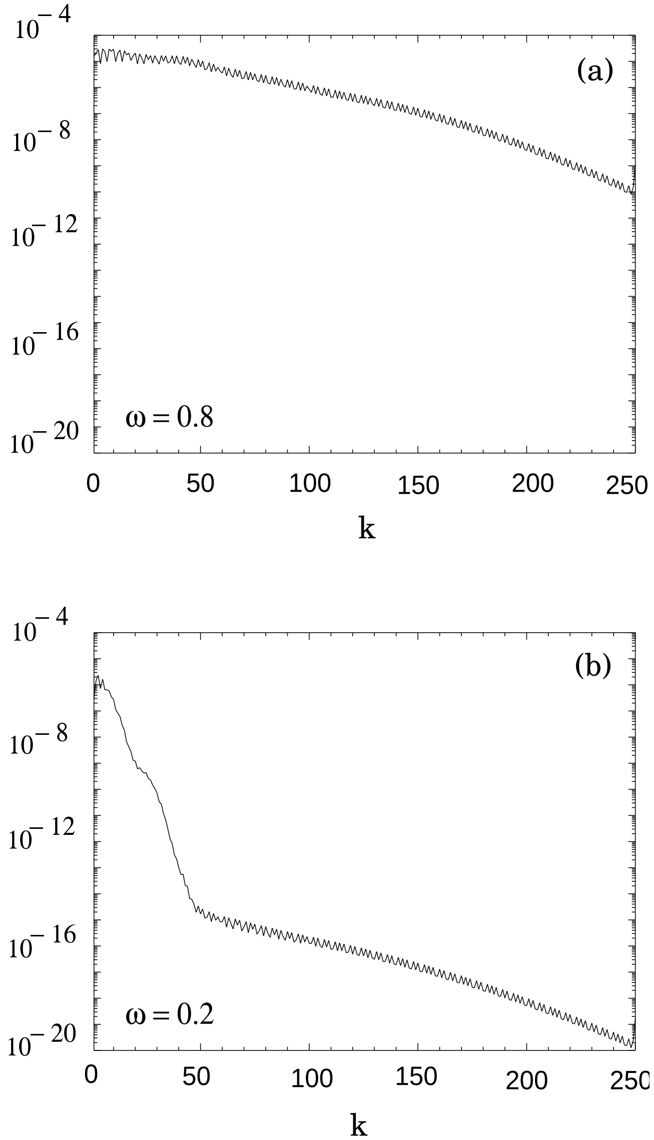

Figure 13: Magnetic energy spectra in lin-log coordinates for a = 1, $R^M = 5000$ with (a) $\omega = 0.8$ and (b) $\omega = 0.2$.

The spectral signatures of the two types of spatial structures is visible in fig.13 where, as can be seen the magnetic energy spectra is plotted in lin-log coordinates for the parameters $a = 1, \epsilon = 0.1, R^M = 5000$ with (a) $\omega = 0.8$ and (b) $\omega = 0.2$. In the former case, the spectrum is quasi-constant up to $k \sim 50$, corresponding to a sharp structures of width $\delta l \sim 2\pi/50$ (see fig. 12). In the latter, the spectrum decreases rapidly, until it meets - at a level of order 10^{-10} - a broad band noisy spectrum corresponding to a low-level filamentary structure with smaller growth rate, as can be checked on contours with logarithmically - assigned valued.

When $a \neq 1$ and ϵ small enough, two distinct chaotic zones exist, as shown in fig.2. By inspection of fig.10, it is striking that the fastest growing magnetic structures are localized in space in the wider chaotic regions, as measured by the Melnikov function (fig 3b). Indeed, for $a = 0.5$, when $\omega = 0.8$, the F_+ function defined in the appendix is dominant (see fig. 3b) and the magnetic field grows near the perturbed homoclinic orbit associated to the $(0, \frac{3\pi}{2})$ stagnation point ("inner orbit"), whereas when $\omega = 1.6$, F_- is dominant and the magnetic field grows near the homoclinic orbit associated to the $(\pi, \frac{\pi}{2})$-stagnation point ("outer orbit"). We checked that this configuration is preserved when the Reynolds number is increased. Similar observations were made for other values of a (still keeping $\epsilon = 0.1$). The generated magnetic field which develops for $a = 0.7$ is shown when $\omega = 0.6$ (which as seen in fig.3c correspond to a strong dominance of F_+), $\omega = 1.0$ (in which case F_+ and F_- are almost equal), $\omega = 1.5$ (for which F^- is dominant) and finally $\omega = 2.5$ (where F_+ and F_- are both relatively small, although F_+ still dominates). We indeed observe that when F_+ (resp. F_-) dominates, the magnetic field develops in the outer (resp. inner) chaotic region. This determinant influence of the largest Melnikov function was also successfully tested with $a = 0.2$ and $\epsilon = 0.1$. However, when at fixed ϵ the value of a is increased (for example $\epsilon = 0.1$ and $a = 0.8$), the chaotic zone tends to merge and the magnetic field develops in the common chaotic zone.

Finally, for $a = 0.5$, we observe that when the chaotic zones are no longer distinct (for example $\omega = 0.8$ at $\epsilon = 0.2$), the dominant magnetic structures (not shown) are still located near the same unstable manifold as in the case $\epsilon = 0.1$ where the chaotic zones are distinct. This is similar to the observation that for $a = 1$ and $\epsilon = 1$ (where the chaotic zones are very extended), the magnetic structures develop in the vicinity of the unstable manifold of the hyperbolic point (Galloway and Proctor 1992).

In conclusion, we have considered the kinematic dynamo action of steady two-dimensional flows subject to weak time-periodic perturbations, thus falling into the realm of almost integrable dynamics for the fluid particles. We observed that different magnetic structures are generated in the integral and chaotic zones. In the latter, magnetic structures in the form of sheets survive in the limit of infinite Reynold number and appear to be strongly sensitive to the width of the chaotic zones controlled by the time frequency of the flow and quantitatively estimated in the context of the Melnikov theory. An interesting question is the stability of these structures in the full magnetohydrodynamic regime, when the reaction of the Lorentz force on the fluid velocity becomes relevant.

Acknowledgments: The computations were performed on the CRAY YMP of the Institut Méditéranéen de Technologie (Marseille), thanks computer time provided by the Région Provence-Alpes-Côte d'Azur. Support from the European Cooperative Network "Numerical Simulation of Nonlinear Phenomena" ERBCHRXCT930410 is Acknowledged. This work was initiated with V. Rom-Kedar, while she was visiting the Observatoire de Nice.

[1] Arnold,V.I. and Korkina, E.I. "The grow of magnetic field in a incompressible flow." *Vestn. Mosk. Univ. Mat. Mekh.* **3**, 43-46 (1983).

[2] Bayly, B. and Childress, S." Construction of the fast dynamo using unsteady flows and map in three dimensions, *Geophys. Astrophys Fluid Dyn.* **44**, 221-240 (1988).

[3] Childress, S. "Fast dynamo theory " in "Topological Aspect of the Dynamics of Fluids and Plasmas",11-147, H.K Moffatt, G.M Zaslavsky, P.Conte and M.Tabor (eds.). *NATO ASI series E*, **218**, Kluwer (1992).

[4] Dombre. T, Frisch .U, Greene. J.M, Henon. M, Mehr. A and Soward A.M , "Chaotic streamlines in the ABC flows", *J. Fluid Mech.* **167**, 353-391 (1986).

[5] Du, Y., and Ott, E. "Growth rates for fast dynamos and high Reynolds number fluid instabilities of chaotic flows", *J. Fluid Mech.* **257** , (1993).

[6] Finn and Ott, E. "Chaotic flows and fast magnetic dynamo", *Phys.Fluid* **31**, 2992-3012 (1988).

[7] Galloway, D.J. and Frisch, U.,"Dynamo action in a family of flows with chaotic stream lines" *Geophys. Astrophys .Fluid Dyn.* **36**, 53-83 (1986).

[8] Galloway, D.J. and Proctor, M.R.E. "Numerical calculations of fast dynamo for smooth velocity field with realistic diffusion", *Nature* **356**, 691-693 (1992).

[9] Gilbert, A. "Magnetic field evolution in steady chaotic flows", *Phil. Trans. R. Soc. London*, **339**, 627-656 (1992).

[10] Guckenheimer, J. and Holmes, P. "Nonlinear Oscillations , Dynamical Systems, and Bifurcations of Vector Fields" *Applied Mathematical Sciences* **42**, Springer-Verlag (1983).

[11] Klapper, I. and Young, L.S. "Rigorous bound on the fast dynamo growth rate involving topological entropy." Preprint (1994).

[12] Leonard, A., Rom-Kedar, V. and Wiggins, S. "Fluid mixing and dynamical systems", *Nucl.Phys.* **B** (*Proc.Suppl.*) **2**, 179-190, (1987).

[13] Oseledets, V. "Fast dynamo problem for a smooth map on a two-torus", *Geophys. Astrophys. Fluid Dyn.* **73**, 133-145, (1993).

[14] Otani, N.F. "A fast kinematic dynamo in two-dimensional time dependent flows". *J. Fluid Mech.* **253**, 327-340 (1993).

[15] Ott, E., Du, Y., Sreenivasan, K.R., Juneja, A. and Suri, A.K. "Sign-singular measures : fast magnetic dynamos, and high-Reynolds-number fluid turbulence" *Phys. Rev. Lett.* **69**, 2654-2657 (1992).

[16] Ottino, J.M. " The Kinematics of Mixing: Stretching, Chaos and Transport", Cambridge Texts in Applied Mathematics, Cambridge University Press (1989).

[17] Ponty, Y. Pouquet, A. Rom-Kedar,A. Sulem, P.L"Dynamo Action in a Nearly Integrable Chaotic Flow" in "Solar and planetary Dynamos" 241-248, M.R.E Proctor, P.C Matthews and A.M Rucklige (eds.) Cambrige University Press (1993).

[18] Robert, G.O. "Dynamo action of fluid motions with two-dimensional periodicity". *Phil. Trans. Roy. Soc. London A* **271** , 411-454 (1972).

[19] Soward, A.M. "Fast dynamo action in steady flow". *Fluid Mech.* , **180** , 267-295 (1987).

[20] Soward, A.M. "An asymptotic solution of a fast dynamo in two-dimensional pulsed flow". *Geophys. Astrophys. Fluid Dyn.* **73**, 179-215 (1993).

[21] Vainshtein, S.I and Zeldovich, Ya.B. "Origin of magnetic fields in astrophysics", *Usp. Fiz. Nank.* **106**, 431-457, (*Sov. Phy. Usp.* **15**, 159-172) (1972).

[22] Vishik, M.M. (1992) unpublished.

We compute here the Melnikov functions for the two chaotic zones associated to perturbed homoclinic orbits of the dynamical system (2), in the case $a \neq 1$. Due to the system symmetries, it is sufficient to concentrate on $a < 1$. Using the notation of section 2 , the solution (u_0, v_0) of the unperturbed system (5) with $\epsilon = 0$, rewrites

$$d\tau = S_1 \frac{du_0}{\sqrt{1-(H-a\cos u_0)^2}}, \qquad d\tau = -S_2 \frac{dv_0}{a\sqrt{1-(\frac{(H-\cos v_0)^2}{a^2})}} \quad , \qquad (A.1)$$

where $H(u_0, v_0) = \cos v_0 + a\cos u_0$ is the associated Hamiltonian. Here $S_1 = \text{sign}(\frac{du_0}{d\tau})$ and $S_2 = \text{sign}(\frac{dv_0}{d\tau})$ depend on the direction along which the system evolves on the orbit. The initial conditions corresponding to $u_o = \pi$ on the branches $j = 1$ and $j = 2$, to $v_0 = 0$ on the branch $j = 3$, $v_0 = 2\pi$ on the branch $j = 4$ (see fig.14). Concerning the sign of S_1 and S_2, on $j = 1$ for example, we have $S1 = -1$, while $S2 = 1$ for $\tau > 0$ and $S2 = -1$ for $\tau < 0$.

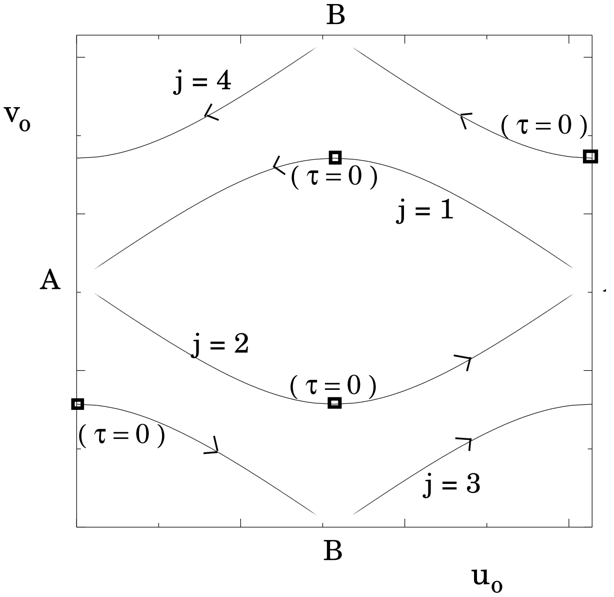

Figure 14: The various homoclinic orbits (indexed by j) for the unperturbed system ($\epsilon = 0$) with $a = \frac{1}{2}$. On each orbit, the small square labeled by ($\tau = 0$), indicates the initial conditions used in the analysis presented in the Appendix.

At the "inner" fixed point A corresponding to (u_0, v_0)=$(0, \pi)$ (or $(\pi, \pi/2)$ in the original coordinates), $H = a - 1 < 0$, while at the "outer" fixed point B of coordinates $(\pi, 0)$ (or $(0, 3\pi/2)$ in the original coordinates), $H = 1 - a > 0$.

To deal with eq. (A.1), it is convenient to define $\phi = (\tan(\frac{u_0}{2}))^S$ and $\psi = \sqrt{a}\,(\tan(\frac{v_0}{2}))^{-S}$, where S=sign(H). For the inner orbit, $S = -1$, while for the outer orbit $S = 1$. We write

$$\cos u_0 = S\frac{1-\phi^2}{1+\phi^2} \quad , \quad \cos v_0 = -S\frac{a-\psi^2}{a+\psi^2} \quad .$$

Prescribing that at the initial time $\tau_0 = 0$, $\phi(0) = 0$ and $\psi(0) = \sqrt{1-a}$, the solution of eq.(A.1) reads

$$\phi = \sqrt{1-a}\sinh(SS_1\sqrt{a}\ \tau)$$

$$\psi = \sqrt{1-a}\cosh(SS_2\sqrt{a}\ \tau) \quad .$$

This enables us to express

$$\sin u_0 = -S_2\frac{2\ \phi}{1+\phi^2} \quad , \quad \sin v_0 = S_1\frac{2\ \sqrt{a}\ \psi}{(a+\psi^2)} \ . \quad (A.2)$$

Substituting in eq.(7) and computing the resulting integrals with the condition that for $a < 1$, $v_0(\tau) = v_0(-\tau)$ and $u_0(\tau) = -u_0(-\tau)$, we obtain for the Melnikov functions $F_+(\omega)$ and $F_-(\omega)$, associated to outer and inner chaotic zones respectively,

$$F_+(\omega) = \sup_{j=2,3}\sup_{\tau_0} \mid M^j(\tau_0) \mid = \mid (a\ \omega\ I_1\ +\ \omega\ I_2) \mid$$

and

$$F_-(\omega) = \sup_{j=1,4}\sup_{\tau_0} \mid M^j(\tau_0) \mid = \mid (a\ \omega\ I_1\ -\ \omega\ I_2) \mid \quad ,$$

with

$$I_1 = 4\frac{\sqrt{1-a}}{\sqrt{a}}\int_0^\infty \frac{\sinh t}{1+(1-a)\ \sinh^2 t}\ \sin(\frac{\omega}{\sqrt{a}}\ t)\ dt \quad ,$$

$$I_2 = 4\sqrt{1-a}\int_0^\infty \frac{\cosh t}{1+(1-a)\ \sinh^2 t}\ \cos(\frac{\omega}{\sqrt{a}}\ t)\ dt \quad .$$

These two functions are plotted in fig. 3b for $a = 0.5$. and in fig. 3c for $a = 0.7$.

Chapitre C

Effet dynamo pour un écoulement proche de l'intégrabilité.

Dynamo Action in a Nearly Integrable Chaotic Flow

Y. Ponty, A. Pouquet, V. Rom-Kedar & P.L. Sulem
OCA, CNRS URA 1362
BP 229
06304 Nice Cedex 04, France

M.R.E Proctor, P.C Matthews & A.M Rucklidge (eds.)
Theory of Solar and Planetary Dynamos, 241-248
Cambridge University Press (1993).

Abstract

Dynamo action of a time periodic flow with frequency Ω, depending on two space variables, introduced by Galloway & Proctor (1992) is considered when the underlying dynamical system is nearly integrable. Competition between fast and slow dynamos is obtained according to the value of Ω. Fast dynamos produce magnetic sheets located in the chaotic regions near the separatrices of the integrable flow. Slow dynamos lead to magnetic eddies which elongate with increasing magnetic Reynolds number R_m and tend to circumscribe elliptic stagnation points. Sheets and eddies may coexist at moderate R_m. A heuristic argument based on the Melnikov method is used to characterize the frequencies which maximize the efficiency of fast dynamos.

1 Introduction

A simple smooth chaotic flow often used as a candidate for fast dynamos is the "ABC flow" $\mathbf{u} = (A\sin z + C\cos y, B\sin x + A\cos z, C\sin y + B\cos x)$, where A, B, C are non-zero coefficients. This flow only involves one wavenumber, which considerably reduces the number of operations when the induction equation for the magnetic field

$$\partial_t \mathbf{b} = \nabla \times (\mathbf{u} \times \mathbf{b}) + \eta \Delta \mathbf{b} \tag{1}$$

is solved numerically in Fourier space (Arnold & Korkina 1983, Galloway & Frisch 1986). The dynamo problem is however three-dimensional, which limits the Reynolds number to moderate values.

Examples of flows that seem well-suited to probe the large magnetic Reynolds number limit on present-day computers were recently introduced by Galloway & Proctor (1992) who used the fact that flows depending on only two space variables can be chaotic if they are time-dependent. We concentrate here on their "circularly polarized" model (CP)

$$\mathbf{u} = (A\sin(z + \sin\Omega t) + C\cos(y + \cos\Omega t), A\cos(z + \sin\Omega t), C\sin(y + \cos\Omega t)) \tag{2}$$

These flows which display large chaotic regions, can be viewed as a modification of the integrable ABC flow corresponding to $B = 0$, by the introduction of a time periodic phase. For this velocity, magnetic field modes with wavevectors having the same component k_1 in the x-direction, evolve independently. Consequently, k_1 can be fixed and the magnetic field computed with a two-dimensional code. For convenience, the (y, z)-periodicity of the magnetic field is taken as that of the flow. There is no periodicity in the x-direction and k_1 can be chosen arbitrarily (but non-zero). For $k_1 = 0.57$, together with $A = C = \sqrt{3/2}$ and $\Omega = 1$, convincing evidence of fast dynamo was obtained, the magnetic growth rate remaining essentially constant for magnetic Reynolds number $10^2 \leq R_m \leq 10^4$. We consider here a similar flow, but in a regime where it is nearly integrable. This is obtained by introducing a small parameter ϵ in front of the oscillatory phase of the velocity.

2 The dynamical system

The fluid trajectories, to be understood mod 2π, obey

$$\dot{y} = A\cos(z + \epsilon\sin\Omega t)\ ,\ \ \dot{z} = C\sin(y + \epsilon\cos\Omega t) \tag{3}$$

together with $\dot{x} = A\sin(z + \epsilon \sin \Omega t) + C\cos(y + \epsilon \cos \Omega t)$. By dividing (3) by C and rescaling time, it is easily seen that, in addition to the perturbation amplitude ϵ, this dynamical system depends on only two parameters, the reduced frequency $\omega = \Omega/C$ and the ratio $a = A/C$. We concentrate here on the case $a = 1$ for which the unperturbed system has heteroclinic orbits. For convenience, results will be presented in terms of ω.

For $\epsilon = 0$, system (3) admits two elliptic stagnation points $(0, \pi/2)$, $(\pi\ , 3\pi/2)$, and two hyperbolic ones $(0\ , 3\pi/2)$, $(\pi\ , \pi/2)$. For $\epsilon \neq 0$, the points of zero velocity rotate with angular velocity Ω on circle of radius ϵ, centered at the stagnation points of the unperturbed problem. Useful insight on the system is provided by Poincaré sections in time (stroboscopic views) at t $= n2\pi/\Omega$ with $n \in N$. The size of the chaotic zones is as expected monotonically decreasing with ϵ, yet exhibits a non trivial dependency with ω. Figure 1 shows the section in the (x, y)-plane, for $\epsilon = 0.1$, and various ω. The observable chaotic regions are localized along the heteroclinic connections of the unperturbed system, whereas for $\epsilon = 1$ they cover a large fraction of the domain.

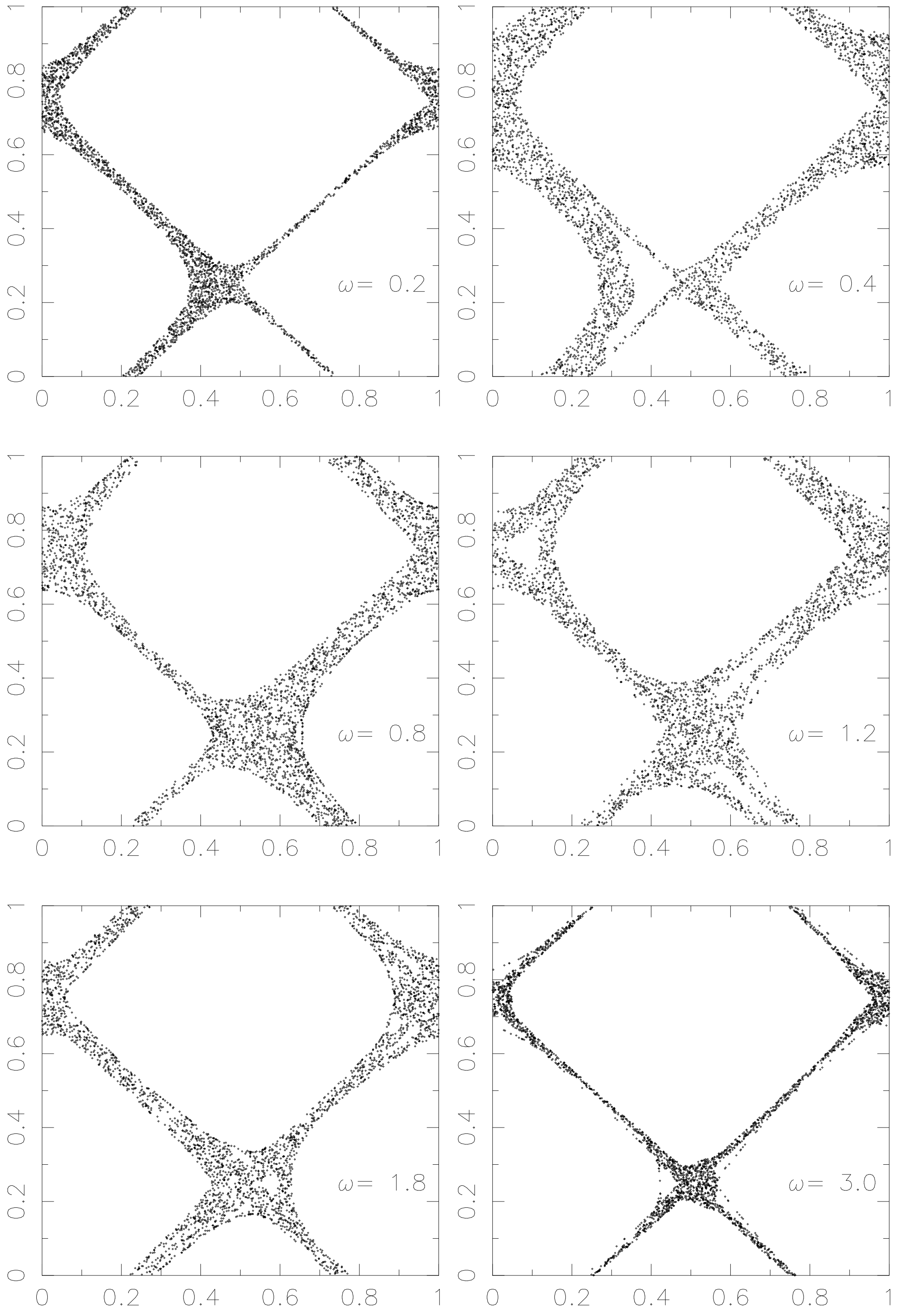

Figure 1: Time Poincaré sections for flow (3), with $a = 1$, $\epsilon = 0.1$.

3 Dynamo action

The induction equation (1) has been integrated with the above velocity field in the case $A = C = 1$ and $\epsilon = 0.1$. The wavenumber k_1 in the x-direction was taken equal to 0.57, as in Galloway & Proctor (1992). The magnetic Reynolds number $R_m = 1/\eta$ was pushed up to 10^4 and the reduced frequency ω varied from 0 to 3. We observe that as soon as the magnetic Reynolds number exceeds a few units, after a transient, the magnetic energy $\int \mathbf{b}^2 d\mathbf{x}$ grows exponentially in time with a growth rate 2λ. In Figure 2, λ is plotted versus R_m for various ω. For some values, e.g. ω =0.8, λ tends to saturate at a finite value as R_m increases, indicating a fast dynamo. In contrast for $\omega = 0.2$, the growth rate decreases monotonically for $R_m > 10$, at least up to $R_m = 5000$. The question arises whether this decay continues for arbitrarily large Reynolds number corresponding to a slow dynamo. It is however not precluded that for any finite non-zero ω, a (weak) fast dynamo emerges at large enough Reynolds number. Note that at sufficiently low Reynolds number λ is not sensitive to ω since growth rates corresponding to different ω fall on the same curve λ versus R_m. The separation from this common curve occurs at different Reynolds numbers for different frequencies, with a minimum for $\omega \approx 0.8$. We interpret this behaviour as resulting from a competition between slow and fast dynamos. Note that for $\omega = 0.8$, λ seems to saturate at a value close to 0.15, only a factor of two below the value obtained for this frequency with $\epsilon = 1$.

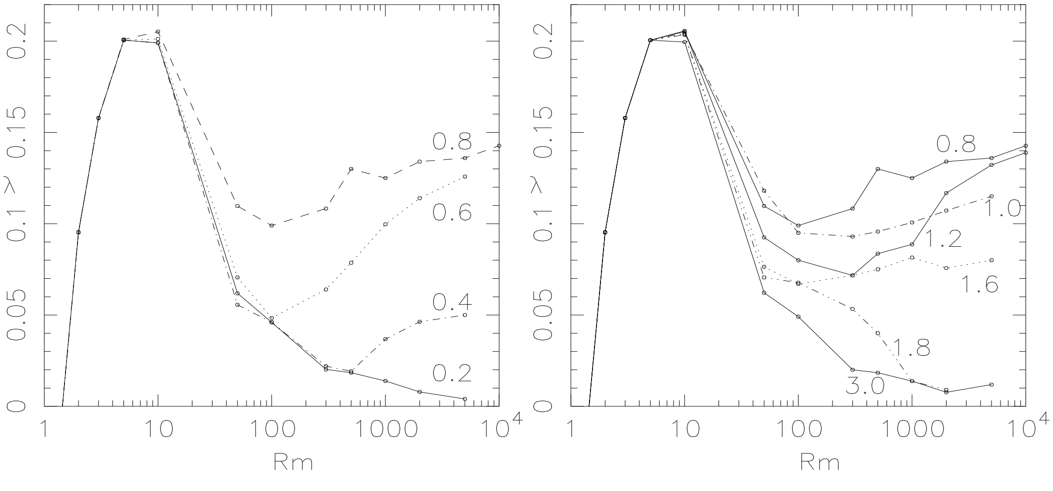

Figure 2: Dynamo growth rate λ versus the magnetic Reynolds number R_m.Curves are labelled by the corresponding value of ω.

The geometry of the magnetic structures are significantly different for fast and slow dynamos. Figure 3 shows the contours of the magnetic field amplitude in the (y, z)-plane for various ω at $R_m = 2000$. At ω =0.8, for which the dynamo appears to be fast, the magnetic structures consist essentially of magnetic layers located in the chaotic regions, near the separatrices of the unperturbed system. As R_m is increased, the thickness of the layers decreases, possibly like $R_m^{-1/2}$ as suggested by a dominant balance argument between stretching and dissipation. Furthermore, the transverse structure of the layer becomes richer with the formation of secondary maxima, and is reminiscent of the structure of the tangled unstable manifold of (3).

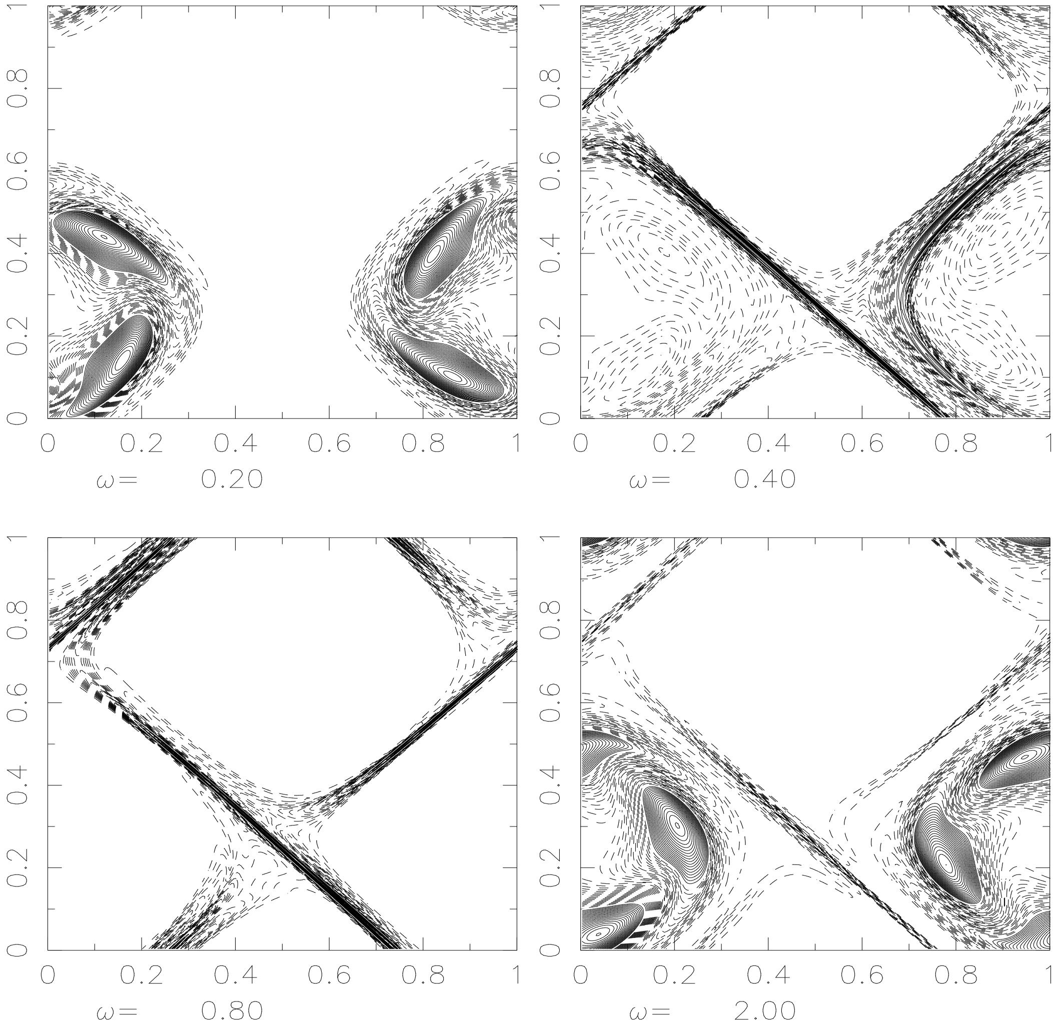

Figure 3: Contours of magnetic field intensity at $R_m = 2000$. Dashed lines refer to levels smaller than half the maximum.

For $\omega = 0.2$, for which the dynamo appears to be slow, the magnetic field concentrates in "magnetic eddies", located in non-chaotic regions, close to the resonance bands of system (3). As R_m is increased, the magnetic eddies, which are rather isotropic at moderate Reynolds numbers, become more elongated and tend to circumscribe the elliptic points. It is noticeable that magnetic eddies, like the resonance bands of (3), appear only in the neighbourhood of zero velocity points rotating in the same direction as the flow particles.

4 Dynamo and chaos: how are they Connected?

We already observed that the dynamo growth rate is sensitive to the velocity frequency. Figure 4 shows this dependency for $R_m = 1000$ and $R_m = 2000$. The central peak, associated with a fast dynamo is maximum at $\omega \simeq 0.8$ and tends to a fixed form as R_m is increased. In contrast, the level of the wings decreases in this limit, as expected for a slow dynamo. The question arises how this behaviour is related to the underlying dynamical system.

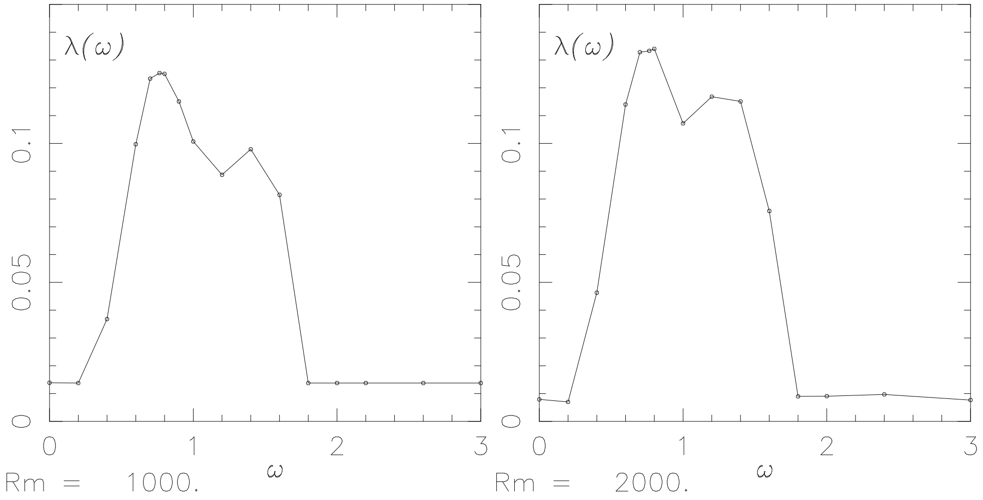

Figure 4: Dynamo growth rate λ versus the reduced frequency ω for $\epsilon = 0.1$, at $R_m = 1000$ and $R_m = 2000$.

A standard characterization of a dynamical system is provided by Lyapunov exponents, because of the analogy between separation of infinitesimally close fluid particles and stretching of the magnetic field at zero magnetic diffusivity. Figure 5(a) shows the largest Lyapunov exponent L versus ω for the trajectories shown in Figure 1. The correlation between this graph and the dynamo growth rate at large magnetic Reynolds number appears to be weak. This confirms that, in the presence of magnetic diffusion, the rate of stretching alone cannot prescribe the efficiency of the dynamo action. Massive cancellation can indeed take place between magnetic field elements stretched in directions which vary strongly from place to place.

One may suspect that the geometry of chaotic zones of the flow and in particular their extent may affect the efficiency of the fast dynamo action. It was suggested by Leonard *et al.* (1987) and Ottino (1989) that the "extent of chaos" may be estimate using the Melnikov method. This method is a perturbative calculation of the distance between stable and unstable manifolds resulting from perturbation of homoclinic or heteroclinic trajectories. It is classically used to test the existence of transverse homoclinic orbits which imply the presence of Smale horseshoes and their attendent chaotic dynamics (Guckenheimer & Holmes 1983; Ottino 1989).

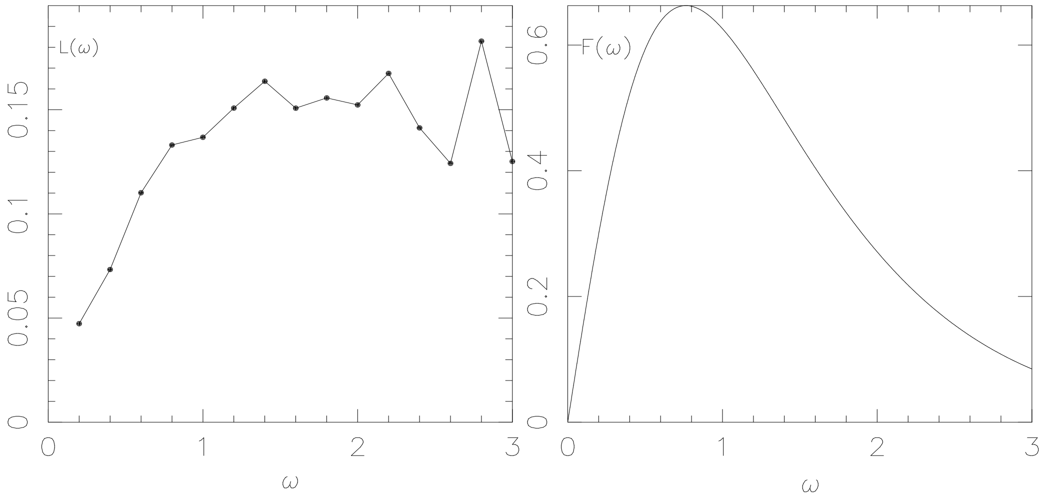

Figure 5: (a) Variation with the reduced frequency ω of the maximum Lyapunov exponent L and (b) of the function F given in (7) for $\epsilon = 0.1$.

By the change of variables $u = z - \pi/2 + \epsilon \sin \omega\tau$, $v = y + \epsilon \cos \omega\tau$ and $\tau = Ct$, and for $a = 1$, (3) becomes

$$\dot{u} = \sin v + \epsilon\omega \cos \omega\tau \ ; \ \dot{v} = -\sin u - \epsilon\omega \sin \omega\tau \ . \tag{4}$$

This is the standard form for the implementation of Melnikov method. To leading order in ϵ, the distance $d(\tau_0)$ between the manifolds is proportional to ϵ and to the "Melnikov function". For each of the unperturbed heteroclinic solution (u_0^j, v_0^j), where $j = 1, 2, 3, 4$, this function reads

$$M^j(\tau_0) = -\omega \int_{-\infty}^{\infty} \sin v_0^j \ \sin(\omega(\tau + \tau_0)) \ d\tau + \omega \int_{-\infty}^{\infty} \sin u_0^j \cos(\omega(\tau + \tau_0)) \ d\tau \ . \qquad (5)$$

After some algebra, we get

$$M^j(\tau_0) = F(\omega) \ (S_1^j \sin \omega\tau_0 + S_2^j \cos \omega\tau_0) \ , \qquad (6)$$

where $(S_1, S_2) = (-1, 1), (-1, -1), (1, -1), (1, 1)$ for $j = 1, 2, 3, 4$ respectively. Furthermore

$$F(\omega) = \omega\pi \ \mathrm{sech}(\frac{\pi\omega}{2}) \ . \qquad (7)$$

Quoting Ottino (1989), "we expect that an extreme in $F(\omega)$ should maximize the extent of chaos". This function is plotted in Figure 5(b). We observe that the range of frequencies ω leading to the largest dynamo growth rates (Figure 4) is located around the maximum of $F(\omega)$. We checked that for sufficiently small ϵ (typically $\epsilon < 0.5$), this behaviour is essentially independent of ϵ.

The Melnikov method has here been used as an heuristic tool to measure the width of the chaotic zones. Further investigations are required to decide whether the location of the maximum dynamo growth rate is indeed correlated with the location of the maximum of the Melnikov function (as found here) or if it is mostly a coincidence. As the next step, we plan to examine the case $a \neq 1$, where heteroclinic connections of the unperturbed problem are replaced by homoclinic orbits.

Computations were performed on the CRAY-YMP of the Institut Mediteranéen de Technologie (Marseille).

[1] Arnold V.I. & Korkina E.I. 1983 The growth of magnetic field in an incompressible flow, *Vestn.Mosk.Univ.Mat.Meckh.* **3**, 43-46 .

[2] Galloway, D.J. & Frisch, U. 1986 Dynamo action in a family of flows with chaotic stream lines, *Geophys.Astrophys.FluidDyn.* **36**, 53-83.

[3] Galloway, D.J. & Proctor, M.R.E. 1992 Numerical calculations of fast dynamos for smooth velocity field with realistic diffusion, *Nature*, **356** , 691-693.

[4] Guckenheimer. J. & Holmes. P. 1983 Nonlinear Oscillations Dynamical System and Bifurcations of Vector Fields, *AppliedMathematicalSciencesSeries* **42**, Springer.

[5] Leonard, A., Rom-Kedar, V. & Wiggins 1987 S. Fluid mixing and dynamical systems, *Nucl.Phys.* **B**(*Proc.Suppl.*) **2**, 179-190.

[6] Ottino, J.M. 1989 The Kinematics of Mixing: Stretching, Chaos and Transport, *CambridgeTexts inAppliedMathematics*, Cambridge University Press.

Résultats et Perspectives

La première partie de ce travail concerne les écoulements convectifs avec rotation dans des domaines étendus, à nombre de Prandtl fini, pour des conditions aux limites supérieures et inférieures libres ou rigides.

A partir des équations de Boussinesq, l'analyse de stabilité des rouleaux de convection dans un fluide à nombre de Prandtl fini, avec des conditions aux limites libres, a montré l'existence d'une nouvelle instabilité en présence de rotation. Cette instabilité amplifie des perturbations dont le nombre d'onde fait un angle petit avec celui des rouleaux de base. Dans l'espace physique, les rouleaux sont déstabilisés par des zones d'étirement engendrées par l'écoulement moyen, et cela produit une rotation globale dans le sens de la rotation.

Pour étudier le développement non linéaire de cette instabilité, un modèle de type Swift-Hohenberg a été construit, permettant de traiter la dynamique des textures dans des domaines à grand rapport d'aspect, aussi bien dans le cas de conditions aux limites libres que rigides. Ces modèles reproduisent précisément les instabilités de Küppers-Lortz et celles "à petit angle" et ainsi que les frontières de stabilité des instabilités de phase près du seuil de convection.

Une analyse de dynamique de phase a permis de retrouver l'instabilité varicose présente en l'absence de rotation et de mettre en évidence son prolongement en une instabilité varicose asymétrique en présence de rotation. Ceci permet d'établir une relation entre l'instabilité de phase varicose asymétrique et l'instabilité à petit angle. En effet, ces deux instabilités peuvent être vues comme la manifestation d'une même instabilité pour des types de perturbations différentes.

En régime non linéaire, la simulation du modèle avec des conditions aux limites libres, à nombre de Prandtl modéré et faible rotation a montré la formation de textures cohérentes sous forme de cibles émergeant d'une turbulence à petite échelle, l'écoulement moyen se concentrant sous forme de tourbillons cohérents. La dynamique dans le cas des conditions aux limites rigides conduit, à faible rotation, à une relaminarisation des textures suite au déplacement et à l'annihilation des dislocations.

Une étude de la dynamique des défauts dans une géométrie cylindrique, tend à montrer ce même phénomène, mais une étude plus fine est envisagée afin de raffiner la description.

La deuxième partie du mémoire porte sur l'effet dynamo dans un écoulement proche de l'intégrabilité. Une dynamo rapide a été mise en évidence par Galloway et Proctor (1992) dans des écoulements ne dépendant que de deux variables d'espace et perturbés par une oscillation temporelle d'amplitude importante. Le présent travail concerne le cas d'une faible perturbation permettant de considérer l'écoulement comme proche de l'intégrabilité et d'utiliser des outils propres à ce régime, afin de relier quantitativement le taux de croissance du champ magnétique avec les propriétés géométriques des trajectoires fluides.

Il apparaît que la divergence des trajectoires évaluées par le calcul des exposants de Lyapunov n'est pas suffisante pour expliquer la variation du taux de croissance de la dynamo en fonction de la fréquence temporelle de la perturbation. Ce dernier est en fait sensible à la largeur des zones chaotiques reliant les points hyperboliques, laquelle est évaluée par la méthode de Melnikov. Cette méthode donne une bonne prédiction de la variation du taux de croissance de la dynamo avec la fréquence de la perturbation. Pour les fréquences auxquelles le taux de croissance de la dynamo est maximum, un exemple de dynamo rapide a été obtenu. Dans ce cas, le champ magnétique se localise autour des variétés instables. Une dynamo lente est aussi présente pour des faibles et fortes fréquences, conduisant à la formation de larges structures magnétiques localisées autour des points elliptiques de l'écoulement.

L'utilisation des modèles de convection en présence de rotation, pour l'étude d'une dynamo cinématique engendrée par des textures convectives, est un prolongement naturel de l'ensemble du travail présenté. Ces modèles de convection avec rotation conduisent à un chaos spatio-temporel qui pourrait fournir un bon paradigme pour l'effet dynamo, dans les écoulements convectifs astrophysiques et géophysiques.

Dans ce contexte, des effets non Boussinesq ainsi que la géométrie sphérique peuvent facilement être pris en compte. La réaction du champ magnétique sur l'écoulement convectif, au travers de la force de Laplace nécessite de nouveaux développements analytiques.

Résumé

Cette thèse comporte deux parties. La première porte sur les écoulements convectifs à nombre de Prandtl fini, en rotation autour d'un axe vertical, dans des domaines étendus. Un calcul perturbatif sur les équations d'Oberbeck-Boussinesq avec des conditions aux limites libres, a permis de mettre en évidence une nouvelle instabilité qui amplifie les perturbations dont le vecteur d'onde fait un petit angle avec celui des rouleaux de base. Afin d'étudier le développement non linéaire de cette instabilité, un modèle de type Swift-Hohenberg généralisé a été construit et étudié numériquement pour des conditions aux limites libres ou rigides. Dans le premier cas, “l'instabilité à petit angle” produit, en régime faiblement non linéaire, une distortion des rouleaux sous l'effet d'un cisaillement moyen qui conduit, après reconnections, à une rotation continue de la texture. En régime fortement non linéaire, on observe pour des rotations modérées, la formation de structures cohérentes sous forme de cibles de grande taille, associées à la présence de forts tourbillons, une configuration compatible avec les propriétés d'invariance par rotation de l'instabilité à petit angle. Dans le cas de conditions aux limites rigides, la dynamique est gouvernée par le mouvement et l'annihilation de dislocations, pouvant conduire, dans le cas d'un écoulement périodique, à la restabilisation des rouleaux droits.

La deuxième partie de la thèse, porte sur l'étude d'une dynamo cinématique dans un écoulement hamiltonien faiblement perturbé. Le champ magnétique qui se développe dans les zones chaotiques localisées le long des orbites homoclines ou hétéroclines, survit à forts nombres de Reynolds magnétique, contrairement aux tourbillons magnétiques apparaissant dans des zones intégrables. Il est montré que le taux de croissance du champ magnétique est sensible à la largeur des zones chaotiques, qui est évaluée par la méthode de Melnikov.

Abstract

This thesis includes two parts. In the first one, the problem of rotating convection at finite Prandtl number in a large aspect ratio container is considered. A singular perturbation analysis performed on the Oberbeck-Boussinesq equations with free-slip top and bottom boundary conditions, points out a new instability which amplifies perturbations whose wavevectors make a small angle with the wavevector of the basic rolls. In order to study the nonlinear development of this instability, a generalized Swift-Hohenberg model has been derived and studied numerically for both free-slip and rigid boundary conditions. In the former case, the “small-angle instability” produces, in the weakly nonlinear regime, a distortion of the rolls under the effect of a strong mean shear, which, after reconnections, leads to a continuous rotation of the pattern. In the fully nonlinear regime, the formation of coherent targets associated to large vortices, is observed, a pattern consistent with the rotational invariance of the small-angle instability. In the no-slip case, the dynamics is governed by the gliding and the annihilation of dislocations, leading to the stabilization of the straight parallel rolls.

In the second part, the kinematic dynamo action of a weakly perturbed hamiltonian flow is considered. The magnetic structures generated in the chaotic zones along the heteroclinic or homoclinic orbits, survive in the limit of infinite Reynold number, in contrast with the magnetic eddies which appear in integrable zones. It is shown that the magnetic growth rate, is strongly sensitive to the width of the chaotic zones, which is estimated using the Melnikov method.